Alma Mater Studiorum - Università di Bologna

DOTTORATO DI RICERCA IN

INGEGNERIA ELETTRONICA, TELECOMUNICAZIONI E TECNOLOGIE DELL'INFORMAZIONE

Ciclo XXIX

Settore Concorsuale di afferenza: 09/E3
Settore Scientifico disciplinare: ING-INF/01

ALGORITHMS AND NUMERICAL METHODS FOR ELECTRICAL BRAIN IMAGING

Presentata da: Andrea Samorè

Coordinatore Dottorato
Prof. Ing. Alessandro Vanelli Coralli

Relatore
Prof. Ing. Roberto Guerrieri

Esame finale anno 2017

Contents

List of Figures

Acronyms

BCI Brain Computer Interfaces.

CPUs Central Processing Units.

CSF Cerebrospinal fluid.

CT Computed Tomography.

DOT Diffuse Optical Tomography.

EBI Electrical Brain Imaging.

ECoG EleCtrocorticoGraphy.

EEG Electroencephalography.

EIT Electrical Impedance Tomography.

ERP Event Related Potentials.

FD Frequency Difference.

fMRI functional Magnetic Resonance Imaging.

FVM Finite Volume Method.

GPGPU General Purpose Graphics Processing Units.

GPUs Graphics processing units.

LORETA LOw REsolution electromagneTic tomogrAphy.

MEG Magnetoencephalography.

MREPT Magnetic Resonance Electrical Properties Tomography.

MRI Magnetic Resonance Imaging.

OpenMP Open Multi-Processing.

PAR Parametric Approach to Reconstruction.

PET Positron Emission Tomography.

SEEG Stereoelectroencephalography.

sLORETA Standardized LOw REsolution electromagneTic tomogrAphy.

SNR Signal to Noise Ratio.

SPECT Single Photon Emission Computed Tomography.

SVD Singular Value Decomposition.

TD Time Difference.

tPA Tissue Plasminogen Activator.

TR Tikhonov Regularization.

VEP Visual Evoked Potentials.

Abstract

Electrical brain imaging (EBI) refers to a set of techniques that exploit either the spontaneous electrical activity of the central nervous system, as in electroencephalographic (EEG) source reconstruction, or make use of external current injections, as in electrical impedance tomography (EIT) , to image the structure or function of the brain. When compared to other brain imaging methods used in research or in the clinical setting, such as computed tomography (CT), magnetic resonance imaging (MRI), functional MRI (fMRI), positron emission tomography (PET) and single photon emission computed tomography (SPECT), EIT and EEG source localization instrumentation offer the advantages of portability, low cost, high temporal resolution [ms] and quick setup. The downsides are a low spatial resolution [cm], high computational cost of the image reconstruction process and high sensitivity to imperfections of the electrical model of the head.

In this work, a new special purpose reconstruction algorithm for EIT is presented and validated wth experimental measurements performed on a cylindrical phantom and on a simulated human head. The algorithm focuses on the quick detection of compact conductivity contrasts in imperfectly known in 3D domains. The performance of the proposed algorithm is then compared to the one of a benchmark reconstuction method in the EIT field, Tikhonov regularized reconstruction, with stroke detection and classification as a case study. Moreover, the possible application of EIT imaging to the detection of epileptic foci with intracranial deep electrodes (stereoelectroencephalography or SEEG) is explored.

Finally, EEG source reconstruction algorithms are implemented on a heterogeneous multi-CPU and multi-GPU computing system to significantly reduce the reconstruction time.

Chapter 1

Introduction

In this work, reconstruction algorithms for electrical imaging techniques applied to the brain are presented from a theoretical point of view and their implementation is detailed.

Due to the combined advantages of low cost, very high temporal resolution, generally quick setup and ability to image both the structure and function of the volume of interest, electrical imaging is a very active area of research.

ElectroEncephaloGraphic (EEG) source localization measures the voltages generated by the neurons to produce a 3D map of brain activity. The reconstructed current density distribution can then be used as an input for Brain Computer Interface (BCI) systems [10], or as a diagnostic tool [11], [12] but it may also be promising to monitor the effects transcranial current stimulation [13], [14].

Electrical Impedance Tomography (EIT) exploits the electric potentials generated by current injections to reconstruct an impedance map of the domain of interest. Impedance is related to the structure of the tissue and its metabolic activity due to a coupling with blood flow. The technique is currently employed in several different disciplines, such as geoelectrical imaging [15], industrial process monitoring [16], robotics [17] and biomedical imaging [18] with current applications spanning from the monitoring of ventilation[19] and gastric emptying [20], to the detection of solid tumors [21],[22] and localization of cerebral activity [23].

Nowadays, the main problems affecting electrical brain imaging are high computational cost and high sensitivity to measurement noise and imperfections in the electrical model of the head. Both aspects are addressed in the developed computational methods.

Initially, the structure and function of the brain is summarized and electrical imaging techniques are compared to other imaging modalities

commonly employed for brain imaging both in the clinical and the research setting and their unique characteristics are highlighted. Then, an overview of parallel computing with cost effective heterogeneous multi-CPU and multi-GPU computing systems is outlined. Thanks to parallel computing and new algorithmic approaches, it is possible to partly bypass the problem of high computational cost of electrical brain imaging reconstruction methods and thus expand their application to time critical contexts.

In the following chapters, the focus will be on EIT and EEG source localization, with stroke, epileptic foci localization and visual evoked potentials (VEP) as case studies to illustrate the advantages of the presented algorithms and implementations.

1.1 The Brain and its Activity

The brain is the main organ of the nervous system, and together with the spinal cord, composes the central nervous system.
Its main function is the coordination of all the activities of the body, from interpreting the information from the outside world to regulating basic biological functions like heart rate or hormonal release. It is also the organ responsible for memory, creativity and intelligence.

It is mainly composed of neurons (Figure 1.1), highly specialized cells that are involved in the transmission of information within the brain. Each neuron has a cell body or soma, that contains the nucleus and all the cellular components that are required for its survival (mitochondria, Golgi apparatus...). Several appendices protrude from the soma, the dendrites are short, while the axon is very long, up to tens of thousands of times the diameter of the soma, and generally undergoes extensive branching toward its end.
Neurons can be divided in different groups depending on their anatomy: pyramidal neurons have a triangular soma and long axons that projects toward the scalp. Stellate neurons feature a large number of dendrites that radiate from the cell body, while spindle cells are characterized by long axons that allow widely separated areas of the brain to communicate. The average brain contains about 100 billion neurons that are highly interconnected, with each neuron interacting with up to 10000 other cells, to create a large network.
The transmission of information between two neurons is mediated by molecules named neurotransmitters that are released by the axon of a neuron and are sensed by receptors on the dendrites of the successive cell.
The small gap between two neurons is called synapse and, depending

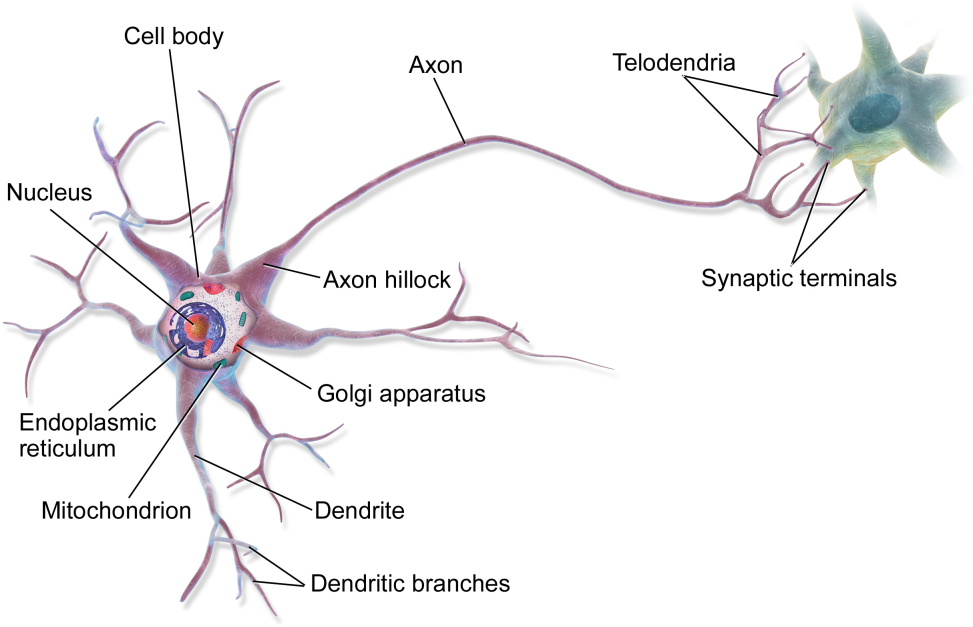

Figure 1.1: Anatomical structure of a neuron [1]

on the type of neuron, can be either excitatory or inhibitory. In the most basic description, the released neurotransmitter induces the opening of Na^+ channels on the cell membrane of the dendrides and thus a depolarization in the membrane, while, in the latter kind of synapse, the chemical signal leads to an increase of the membrane's polarization. If the membrane of a neuron reaches the depolarization threshold (of about -55 mV) an action potential is produced (Figure 1.2). This is a stereotyped signal that travels across the axon and causes the release of neurotransmitters in the synapse. Since the intensity and shape of the signal don't change, the information is carried by the frequency with which action potentials are produced (firing rate). Reaching the threshold of excitation causes the opening of a large number of mainly Na^+ channels which leads to a fast depolarization of the membrane that peaks at about 40 mV. Successively, during the repolarization phase, the K^+ channels open, while the Na^+ ones close, this causes a decrease of the membrane potential that becomes even more negative than the resting potential (-70 mV). This hyperpolarization is associated to a refractory period, a time interval of about 1-2 ms, in which the neuron will be unresponsive. This ensures the return to the resting potential and the complete separation between action potentials.
The electric signal propagates along the axon with a speed of 0.5-2.0 [m/s], a velocity that is not sufficient to grant an adequately quick

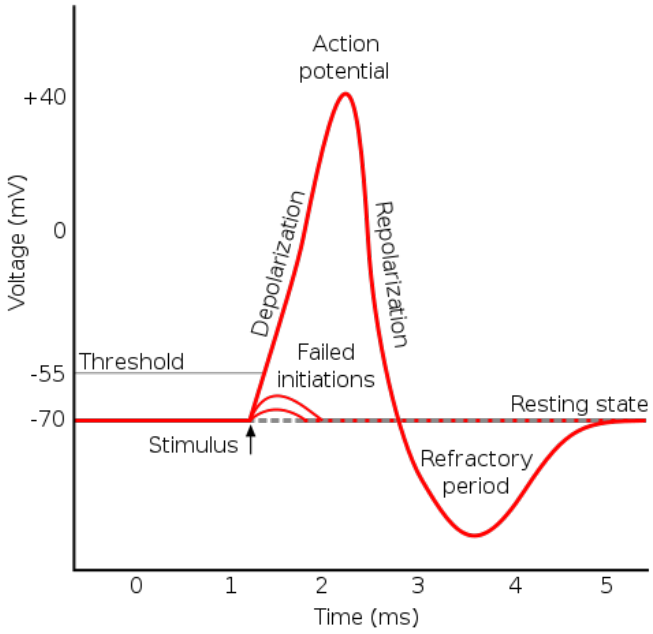

Figure 1.2: Typical shape of an action potential [2]

response in some situations. To address this issue most axons are coated with myelin, an insulating substance composed of proteins and phospholipids that increases the action potential's speed to up to 120 [m/s] depending on the axons diameter. This type of conduction is called saltatory, as the action potential "jumps" from one unmyelinated region to the next (nodes of Ranvier) avoiding any ion exchange in myelinated parts of the axon (Figure 1.3). Beside increasing the signal's speed, the saltatory conduction is also very energy efficient, allowing the transmission of the action potentials for long distances with almost no energy loss.

In the human brain, axons that connect different regions of the brain are mainly located in the white matter, while cell bodies, dendrites and axon terminals, are part of the so called grey matter (Figure 1.4), that also forms the cerebral cortex.

The cross section of the cerebral cortex can be divided in six layers.

- **Layer I**: also called the molecular layer, is the most superficial, it contains mostly dendrites, glial cells (cells that support the neurons and produce the myelin) and horizontally oriented axons and few neurons.
- **Layer II**: features small pyramidal and stellate neurons. It is also

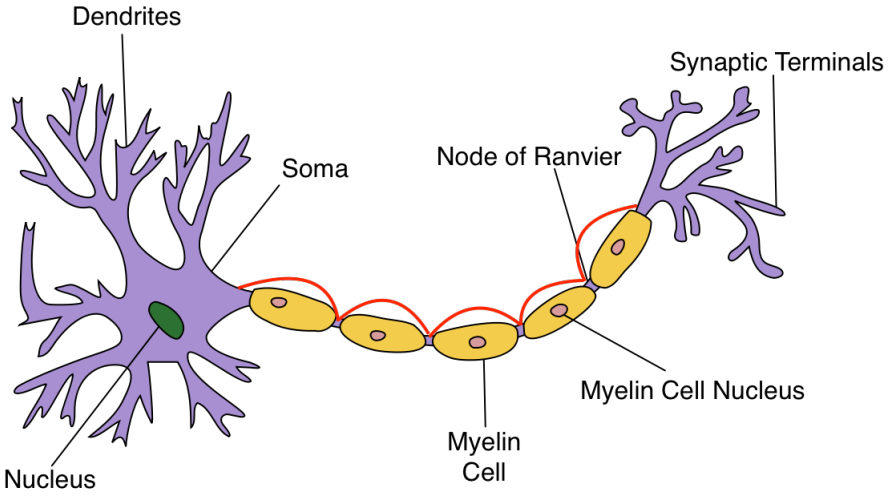

Figure 1.3: Illustration of saltatory conduction [3]

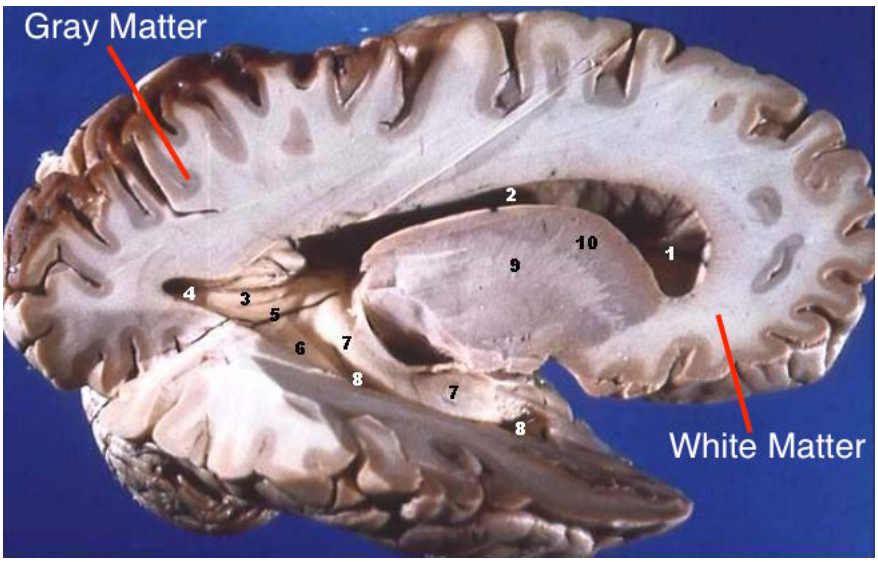

Figure 1.4: Macroscopic division of the brain in grey and white matter [4]

named the external granular level.

- **Layer III**: or external pyramidal level, is mainly composed of pyramidal neurons and other neurons with vertically oriented axons.
- **Layer IV**: also called the internal granular layer, contains stellate and pyramidal neurons.
- **Layer V**: or internal pyramidal level, features mainly large pyramidal neurons.
- **Layer VI**: is composed of large pyramidal and small spindle-like pyramidal neurons and it thus named polymorphic layer.

Over the years several methods have been developed to image the structure or to record and quantify the activity of the brain. These imaging techniques are now used both in the clinic and in research.

1.2 Brain Imaging Techniques

In the following some of the most common brain imaging techniques will be described. Some of them, like computed tomography or magnetic resonance imaging, provide information regarding the structure or the anatomy of the brain, while others (e.g. positron emission tomography, electroencephalography) relate on the activity of this organ. Most of the presented techniques are commonly used in the clinical setting to diagnose a number of pathologies, but they also have a relevant role in research, where they are used to study the brain function and test new potential diagnostic or therapeutic tools.

Several medical imaging techniques can be employed to obtain information about the brain. Structural imaging methods are commonly used to get an accurate representation of the spatial distribution of the different tissues that compose the head, and are commonly employed for the detection of tumors and strokes or to measure the effects of traumas and other medical conditions that can affect the structure of the brain, such as hydrocephalus. Functional imaging, on the other hand, allows for the visualization of brain function, both from an electrical and a metabolic point of view. The electrical activity of the brain can be measured for a variety of reasons, typical examples are to diagnose diseases such as epilepsy, to act as an input for brain computer interfaces (BCI) or for research purposes in neurology and cognitive psychology. While metabolic activity is used both for research (fMRI) and to diagnose a variety of diseases that can affect the brain.

Figure 1.5: GE CT scanner [5]

1.2.1 Computed Tomography (CT)

Computed tomography was introduced in the 1970s as the first three-dimensional brain imaging technique. It relies on the difference in electromagnetic properties of the tissues and specifically on the differential attenuation of the incident radiation to create a structural representation of the brain. It makes use of a X-ray tube and a set of X-ray detectors mounted on a circular structure that is positioned around the subject's head (Figure 1.5).

The rotation of the X-ray tube leads to the acquisition of a number of projections, at different angles, of the structural composition of the brain. The use of computational models allow to combine these data and obtain a three dimensional reconstruction of the subject's head. While being able to distinguish tissues with very small differences in density ($\sim 1\%$), CTs make use of ionizing radiation which have enough energy to cause cellular and DNA damage and have been linked to an increased risk of developing cancer.

1.2.2 Magnetic Resonance Imaging (MRI)

This structural three dimensional brain imaging technique is considered to be complementary to CT and is generally preferred when both techniques convey the same diagnostic information, due to the use of non-ionizing rather than ionizing radiation. MRI is however more expensive than CT scans and it cannot be used in presence of MRI-unsafe implants, like some fracture fixatures, pacemakers or neurostimulators.

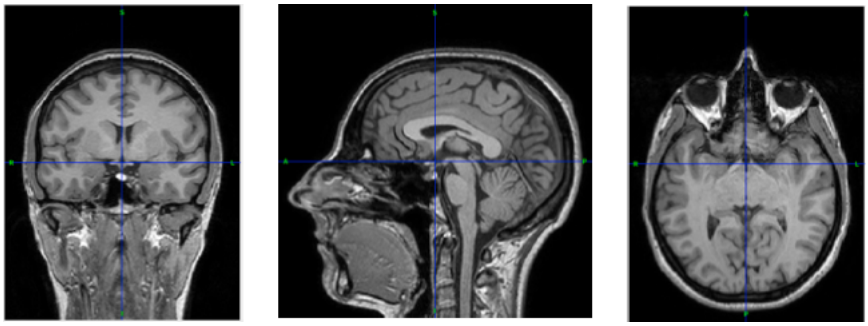

Figure 1.6: MRI slices acquired using alternative directions in space.

MRI exploits the characteristic of the protons of some atoms, like hydrogen, of resonating when hit with a radio frequency pulse within a magnetic field. This phenomenon is called precession and allows to differentiate protons belonging to different tissues. Specifically, upon removal of the of the radio frequency pulses, the atoms return to their original position following a relaxation process that can be characterized through two time constants T_1 and T_2 that differ between tissues (e.g. fat or water) and their location (e.g intracellular water or water in blood and cerebral spinal fluid). The collected data are then organized in three-dimensional images in which the luminosity is generally proportional to T_1 or T_2. During the whole test a constant magnetic field is applied to the subject's head, this causes all the protons to align their axes and precede in the same direction, making the relaxation times identifiable. To pinpoint the source of the signal in the 3D volume, three perpendicular magnetic field gradients along the spatial dimensions are used. One of the three gradients is used to excite the protons within a small region of the subject's head (slice) while the other two subdivide each slice in rows and columns (Figure 1.6).

Modern MRI scans have a very high spatial resolution, with widely available scanners using a 3 T magnetic field able to provide 3D maps composed of $1mm^3$ voxels, however the time resolution remains poor when compared to electrical imaging techniques.

Functional MRI (fMRI)

MRI can also be used as a functional imaging technique to obtain information about energy consumption of brain tissue. fMRI is generally used to measure the blood oxygen level dependent (BOLD) signal which correlate with the hemodynamic response related to the metabolism of neurons and can be used to locate active brain regions.

Since the brain uses glucose as major energy source but it is not

able to store it, an increased neuronal activity is strictly connected to an augmented blood flow, which increments the local concentration of nutrients and oxygenated hemoglobin. Neuronal activity causes a localized decrease in deoxygenated hemoglobin. As oxygenated and deoxygenated hemoglobin interact differently with the magnetic field, neuronal activity can be identified using stimulation sequences sensitive to T_2 which highlight the regions with a more intense signal.

fMRI is also commonly used in brain mapping research, even though its temporal resolution is still in the order of tenths of seconds.

1.2.3 Positron Emission Tomography (PET)

PET is a technique able to quantify the metabolic activity of brain tissue, it can be used to distinguish between Alzheimer's disease and other forms of dementia, study the link between specific psychiatric disorders (e.g. schizophrenia) and brain activity and guide surgery for the treatment of intra-cranial tumours or arteriovenous malformations.

It makes use of a short lived radioactive isotope (tracer), chemically incorporated into a biologically active molecule. The injection of this compound into the subject's circulatory system leads to the accumulation of the active molecule (generally F-18 labeled fluorodeoxyglucose) in the tissue of interest. As the tracer undergoes positron emission decay, it emits a positron. The interaction between the positron and an electron in the nearby tissue annihilates the two particles, creating a pair of gamma photons moving in opposite directions. A scintillator in the scanning device detects these photons, almost simultaneously, thus being able to distinguish annihilation events from spurious radiation.

The reconstruction of the corresponding brain image is a critical aspect of this technique, but mathematical models similar to those employed in CT are generally used. They consist in back-projecting the recorded signal along its line of response, that is adding to every point of the domain the signal's intensity recorded in each projection.

PET scans are non-invasive, even though they involve exposure to ionizing radiation (effective dose of 14 mSv). This is higher than the radiation dose corresponding to a chest x-ray (0.02 mSv) or chest CT scan (6.5-8 mSv).

1.2.4 Single Photon Emission Computed Tomography (SPECT)

SPECT is a technique very similar to PET, but the former measures directly the gamma radiation emitted by the tracer, and not the gamma photons produced by the annihilation of a positron and an electron.

This reduces the SPECT's spatial resolution, as the contemporary detection of two photons by opposite detectors conveys more information than a single gamma ray. SPECT scans are however significantly less expensive, partly because they can use longer-lived radioisotopes that are more easily obtainable and manageable.

For functional brain imaging generally ^{99m}Tc-HMPAO (Technetium-99m- hexamethylpropylene amine oxime) is used as gamma-emitting tracer.

It has an half life of about 6 hours and is found in the brain tissue in concentration proportional to the blood flow. Thus SPECT scans can be used to assess brain's metabolism for example to aid the diagnosis of Alzheimer's disease and vascular dementias.

1.2.5 Diffuse Optical Tomography (DOT)

DOT exploits near infrared light (214-400 THz) to study the optical properties of soft biological tissues. By evaluating the spatio-temporal variations in light absorption and scattering, DOT is able to map the concentration of oxygentated and deoxygenated hemoglobin.

The general functioning principle of this technique involves shining light pulses, generated with a picosecond diode, on the subject's head. The interaction with the different tissues within the brain will attenuate and scatter the light pulses, that are then detected by a number of detectors. The use of physical-computational models allows the estimation of the optical characteristics of the tissues and the reconstruction of an image of the subject's brain.

Additionally, fluorescent contrast agents can be injected into the subject. The excitation of these molecules with light at a specific frequency induces the emission of photons at a longer wavelength that can be recorded and used to map the distribution of the contrast agent within the brain.

1.2.6 Magnetoencephalography (MEG)

MEG is a functional brain imaging technique that exploits magnetometers to record the magnetic field generated by the electrical activity of the neurons. It is extensively used in neurological research to identify the functionality of specific brain regions, investigate cognitive processes, while in the clinical practice can be exploited to localize regions of the brain affected by pathologies or abnormalities.

The signal recorded through MEG is produced by the ionic currents that generate within the dendrites during sinaptic transmission and its

main generators are the pyramidal neurons. This is because the magnetic field produced by each neuron is incredibly small and the coherent orientation of this type of neurons causes their signal to amplify. Even so the signal registered with the MEG has an amplitude of the order of 10 fT, seven order of magnitudes lower than the magnetic noise in an urban environment. As a consequence magnetic shields must be used to isolate the MEG scan from magnetic noise.

Due to its high temporal resolution (10 ms or faster), MEG can be used to complement fMRI with the additional advantage of having an open structure which better adapts to studies involving external stimuli.

1.2.7 Electroencephalography (EEG)

EEG is one of the most commonly used techniques for recording the activity of the brain, it is cheaper and more manageable than other techniques like PET or MRI and it is non-invasive. Furthermore it has a very high temporal resolution ($\backsim$ ms) and is well adapt to behavioural studies. It uses a set of electrodes, generally mounted on a cap in locations specified by an international standard (International 10-20 system, Figure 1.7), to register the electric signal on the scalp produced by the brain's activity. A conductive gel/paste is used to reduce the skin's contact impedance and during the recording a number of procedures to elicit event related potentials may be executed.

The signal recorded with the EEG is mostly produced by the coordinate activity of the pyramidal neurons, due to the fact that their axons are parallel and oriented toward the scalp, thus increasing the strength of their signal on the head's surface and reducing its noise.

Figure 1.8 shows the main components of the EEG signal, waves at different frequencies that are generally identified in the recording and are associated to either a physiological or a pathological activity of the brain. Beta waves are the ones with highest frequency (13-30 Hz) and are associated to conscious thoughts. These waves are generally produced in the frontal or parietal region of the brain, while the alpha ones are more common in the occipital region. These have a lower frequency (8-13 Hz) and correlate with a state of relaxed wakefulness of the subject. Theta waves are even slower (4-8 Hz) and are generally recorded in children or during sleep and meditation. In the hippocampus they correlate to spatial cognition and the memory encoding or retrieval. Indeed an increase in activity in the theta band is recorded during cognitive tasks that require verbal and spatial working memory or item recognition. Delta waves have similar characteristics but are normally associated with the deeper sleep phases and tend to have the highest

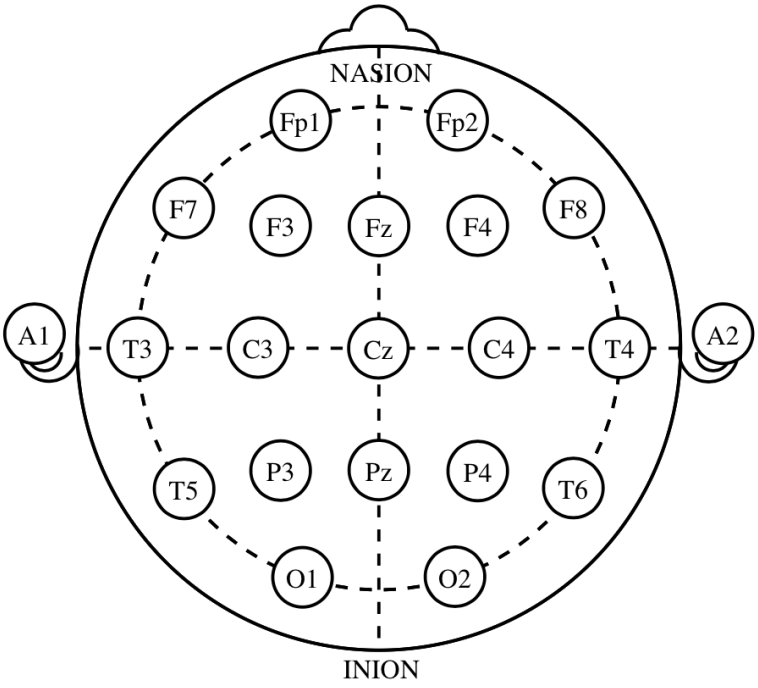

Figure 1.7: Standard positioning of the electrodes on an EEG cap according to the 10-20 system.

amplitude. Another typical analysis of the EEG signal aims to locate the anatomical regions of the brain that produced the potential distribution on the scalp. EEG source imaging is widely used in cognitive neurosciences research, due to the ability of modern systems to image simultaneously the spatial and the temporal activity of the brain, but has also important applications in clinical neurosciences such as Neurology, Psychiatry and Psychopharmacology. In this work it is used to analyse event related potentials (ERP), which highlight the temporal aspects of information processing. The main clinical application, in the field of neurology, is the localization of epileptic foci, even if the study of sensory or motor evoked potentials is of increasing interest. In psychiatry and psychopharmacology, a major focus is the localization of sources in certain frequency bands. While the issue of source localization is similar for these different applications, the pre-processing of the data is somewhat different.

1.2.8 Electrical Impedance Tomography (EIT)

EIT is a reatively new brain imaging technique that aims to reconstruct an impedance map of the subject's head. It uses a set of electrodes

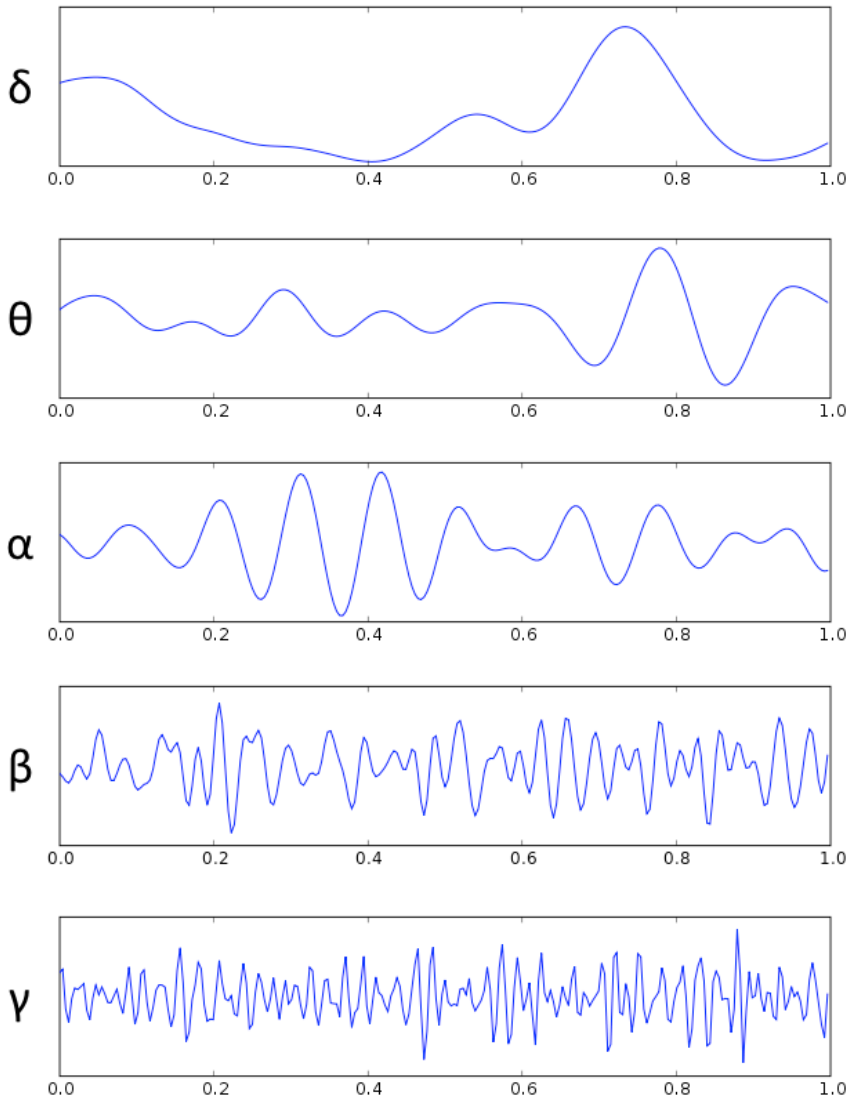

Figure 1.8: Main waveforms recorded with EEG, adapted from [6]

on the scalp to inject small alternating currents according to defined patterns and record the resulting voltage. The repetition of numerous stimulation patterns, alternating the electrodes used to supplement the current and measure the voltage, allows the reconstruction of the conductivity of the biological tissues within the head. This process requires the solution of a non-linear, ill posed, inverse problem that is still the focus of active research. Beside brain imaging, EIT has other applications in which the differences in the electrical properties of the imaged tissues are exploited to detect cancer, monitor ventilation or gastric emptying.

EIT is a non-invasive technique that, unlike most tomographic approaches, does not use ionizing radiations. Furthermore the injected current is not strong enough to cause nerve stimulation, its frequency is too high to induce electrolytic effects and the released Joule heating is easily compensated by the body's thermoregulatory system. Thus it is generally regarded as a safer and cost effective alternative to conventional brain imaging techniques.

1.2.9 Magnetic Resonance Electrical Impedance Tomography (MREIT)

MREIT is a method which combines MRI scans with EIT techniques. Current injections are employed to generate a magnetic flux density which can be measured with a standard MRI scanner to reconstruct the conductivity of the domain of interest [24].

When compared to EIT, MREIT offers a much higher sensitivity in deep regions far from injecting electrodes and a much higher spatial resolution due to the fact that magnetic flux density is measured with an high field MRI scan. On the other hand, the main drawbacks are a lack of portability and a significantly lower temporal resolution [25]. For these reasons, MREIT should be considered as a complementary technique to EIT rather than its evolution.

1.2.10 Magnetic Resonance Electrical Properties Tomography (MREPT)

MREPT is an imaging technique which enables the imaging of electrical permittivity and conductivity distributions in the radio frequency (RF) range comprised between about 10 and 200 MHz [26]. Energy absorption and phase shift at RF in the human body during a MRI scan at high static fields generate patient heating and cause artefacts in the reconstructed images [27], but the same artefacts can be exploited to extract information about the domain of interest. The object to be

imaged with MRI techniques perturbs the RF field of the scanner and recently it has become possible to recontruct the electrical properties (conductivity and relative permittivity) of the domain of interest by measuring the RF magnetic field.

Since tumors tend to have different electrical properties when compared to healthy tissue mainly due to an increased vascularization and altered membrane permeability [28], MREPT reconstructions may have clinical significance.

The main advantages of MREPT over other brain imaging techniques such as EIT and MREIT is the absence of current injections and a well posed image reconstruction problem which leads to a very high spatial resolution in the order of millimeters. On the other hand, being based on MRI scans, the technique is affected by the same disadvantages of MRI equipment: chiefly high cost, significant setup complexity and relatively sparse geographical distribution.

1.2.11 Peculiar Characteristics of EBI

In the following the focus will be on electrical brain imaging techniques and on EEG and EIT in particular. This choice stems from the characteristics of techniques based on electrical measurements that make them particularly attractive for different applications. A comparison table summarizes the characteristics of the described brain imaging methods Table 1.1.

	Spatial Resolution	Temporal Resolution	Structure	Function	Ionizing Radiation	Portability	Cost
CT	mm	10^2 ms	yes	no	yes	no	high
MRI	mm	10^2 ms	yes	no	no	no	very high
fMRI	mm	s	no	yes	no	no	very high
MREIT	mm	s	yes	yes	no	no	very high
MREPT	mm	s	yes	yes	no	no	very high
PET	mm	s	no	yes	yes	no	very high
SPECT	cm	s	no	yes	yes	no	high
MEG	mm	ms	no	yes	no	no	medium
DOT	cm	ms	no	yes	no	yes	low
EEG	cm	ms	no	yes	no	yes	low
EIT	cm	ms	yes	yes	no	yes	low

Table 1.1: Comparison table of brain imaging techniques

Electrical imaging methods are generally non invasive and do not use ionizing radiations, thus reducing the risks and the concerns of performing studies on healthy subjects. Furthermore, the required instrumentation is generally portable and easy to set-up and use with minimal training, with the additional advantage of a cost which is generally orders of mangnitude lower than other noninvasive imaging techniques.

Other techniques commonly employed to image brain tissues, such as MRI, fMRI, PET, SPECT, are indeed considerably more expensive and generally only available in major clinical settings, due to the dimensions of the scanner which often requires a whole custom made room, such as in th case of (f)MRI due to electromagnetic shielding requirements. On the other hand, they grant an higher spatial resolution when compared to electrical brain imaging techniques, with the former in the order of mm and the latter in the order of cm.

Another advantage of electrical imaging techniques is the very high temporal resolution in the order of milliseconds ,which is up to three orders of magnitude higher than MRI, fMRI, PET or SPECT. These characteristics make electrical brain imaging particularly useful in studying the dynamic of brain activity, while allowing for a reasonably accurate representation of the structural information.

With the higher temporal resolution is generally associated a very significant computational cost of the image reconstruction process and thus the development of algorithms for the analysis and the elaboration of these data is currently an active research topic that is benefiting substantially from technological improvements in computer science, like parallel programming in general and GPGPU computing in particular.

1.3 Parallel programming

Traditionally, computers had a single processing unit which run serial software, where only one instruction is executed at a specified time instant and a list of instructions is sequentially processed till the completion of the program. With the advent of limits in frequency scaling suddenly limiting the performance increase of new processors and the ever increasing complexity and computational cost of the developed applications, parallel computing has provided a solution to the need of computational power and has extended the validity of the Moore's Law.

In parallel computing, the throughput is increased not by increasing the clock frequency of the processor but by executing multiple instructions at the same moment in time. Some part of the program can be

often subdivided into smaller, partly independent portions, which can then be executed at the same time and whose results can be combined upon completion.

To process multiple instructions at the same time specialized hardware is required, specifically multiple processing elements (multiple processors or single processors with multiple cores supporting multiple threads) must be available.

Various parallel systems designs have been developed, in the following a single node with multiple central processing units (CPUs), each containing multiple computing cores which support multiple threads of execution, and multiple graphics processing units (GPUs) supporting general purpose computing (GPGPU) is considered (Figure 1.9) due to the advantages of small size, low cost and very high performance.

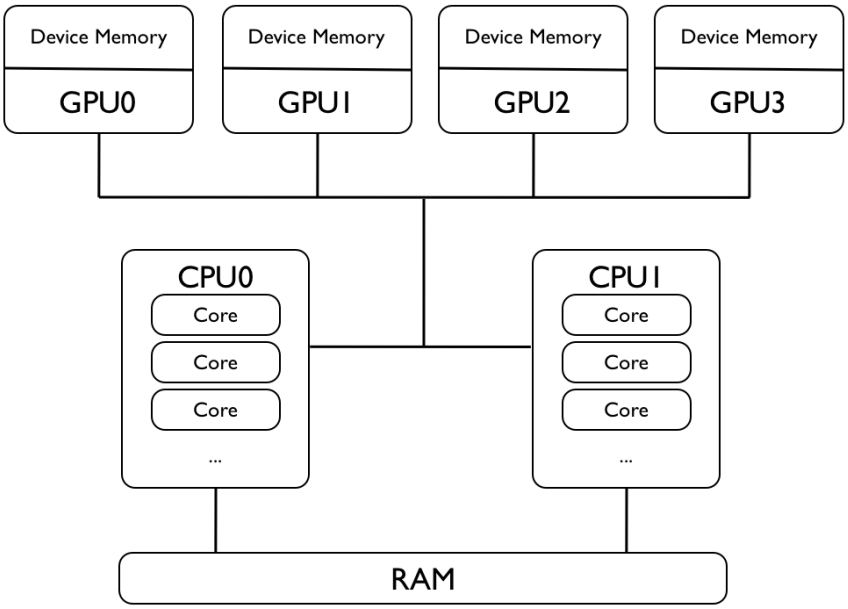

Figure 1.9: Schematic representation of a heterogeneous multi-CPU and multi-GPU computing system.

1.3.1 Computing System

The specifications of the heterogeneous multi-CPU and multi-GPU computing system considered in this work are listed in Table 1.2. This system was chosen to provide high performance computing (HPC) capabilities with off-the-shelf components. In addition, the characteristics of low cost and relatively small size should be drivers for a wide

adoption of similar systems and increase the real world applicability of the presented algorithms.

CPUs	2x Intel Xeon E5-2650 v2 @ 2.60GHz
GPUs	4x Geforce GTX Titan Black
RAM	64 GB

Table 1.2: Specifications of the computing system used in this work

In the considered heterogeneous parallel system, main memory is shared by the CPUs while GPUs are used as accelerators for intensively parallel tasks. For this reason, the Open Multi-Processing (OpenMP) API is used to distribute work on the CPU cores and the Nvidia CUDA parallel programming model to code and run parallel kernels on the GPUs. Each intel Xeon processor is composed of 8 cores, each supporting 2 computing threads, for a total of 32 parallel threads. Nvidia GPUs were preferred to the ATI counterparts due to a more more mature software development framework for GPGPU computing and better performance [29]. The four GPUs are based on the Nvidia Kepler GK110 compute architecture and each of them includes 2880 CUDA cores and 6GB of GDDR5 memory.

1.3.2 Parallel Shared Memory Systems

The most widely employed API for multi-platform shared memory multiprocessing within a single multi-core node is OpenMP. It supports the C, C++ and Fortran programming languages and consists in a set of compiler directives, libraries and environment variables.

OpenMP implements multithreading, where a master threads forks into a set of different working threads that perform the computation Figure 1.10.

All the working threads run concurrently and, while each one executes independently, threads can share variables. OpenMP has been implemented in a wide variety of compilers and is available for Linux, macOS and Windows. The portion of code to be run in parallel is marked by specific directives that generate the thread pool and split the work among the available threads.

1.3.3 GPGPU Computing

GPGPU, which refers to general purpose computing on graphics processing units, is a relatively new way to use graphic cards to solve problems that can also be unrelated to graphics and have traditionally been handled by the CPU. One of the characteristics of GPGPU is the

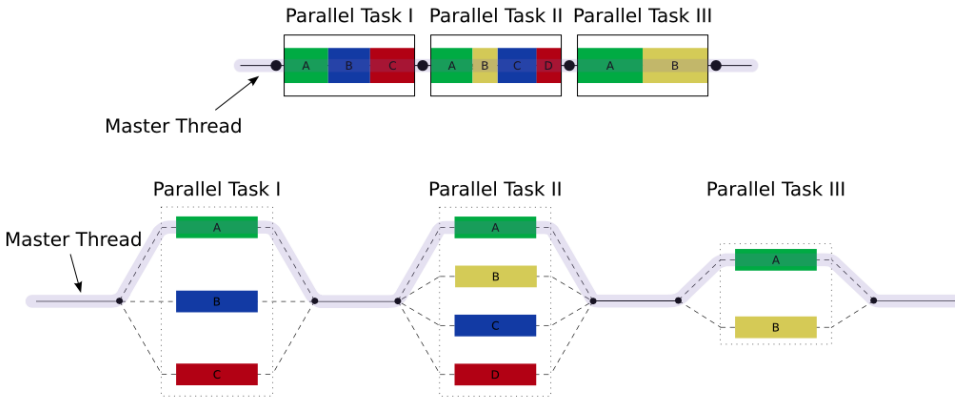

Figure 1.10: Multithreaded computation with OpenMP. To elaborate a parallel task, a master thread generates a number of worker threads. [7]

possibility to transfer data bidirectionally between CPU and GPU with high throughput.

While early attempts to solve general purpose problems with GPUs had to reformat the problem in term of graphics primitives, recently general purpose parallel programming frameworks which greatly simplify GPU programming have been developed.

The leading open source GPGPU computing framework is OpenCL, which is backed by the non-profit consortium Khronos Group, while the most widely adopted proprietary software developer platform is Nvidia CUDA.

OpenCL is not limited to GPUs but can also be used to write code that needs to be executed on heterogeneous platforms that may include CPUs, GPUs, digital signal processors (DSPs), field-programmable gate arrays (FPGAs) and other accelerators.

OpenCL is composed of a C-like programming language and an Application Programming Interface (API) which allow developers to take advantage of the various CPUs and accelerators present in the system.

The CUDA Toolkit is highly optimized but can only be used with Nvidia GPUs. Compilers, libraries and developer tools are included in the toolkit distribution. With CUDA, it is possible to program GPUs in C, C++, Fortran and a few other laguages.

Nvidia Kepler Architecture

A peculiar characteristic of CUDA capable GPUs when compared to CPUs is the very large proportion of die area which is dedicated to

computation rather than control logic and caching (Figure 1.11). The reason is that CPUs are optimized for serial computation and complex control logic is necessary to execute instructions in parallel or out of order while mantaining the appearance of serial execution and caching is needed to reduce the memory access latency[30]. GPUs are instead focused on maximizing the performance of floating point calculations and, to minimize the requirement of control logic, the scheduler picks from a large pool of computing threads to assign work when some wait for memory accesses. Small caches are used to avoid multiple accesses to global memory if multiple threads need to access the same memory location.

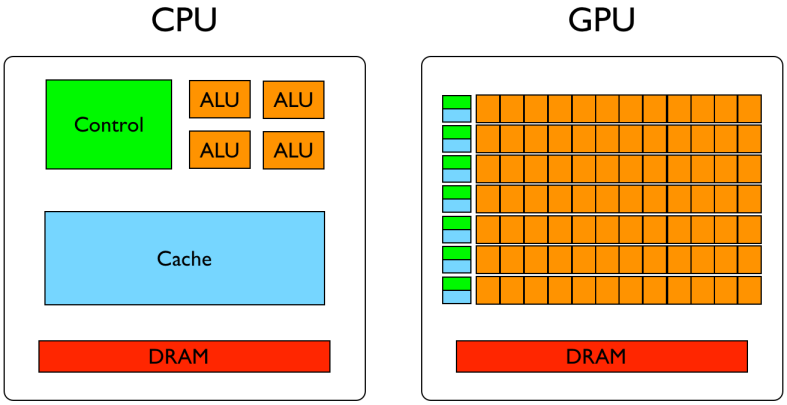

Figure 1.11: Die occupation difference between CPUs and GPUs.

Nvidia GTX Titan Blacks are based on the Kepler GK110 architecture, which includes 15 streaming multiprocessors (SMX) and 6x64 bit memory controllers. When compared to the previous iteration, the Fermi architecture, it proves to be much more power efficient, with 3x the performance per watt. Kepler implements full IEEE 754-2008 compliant single and double precision arithmetic.

Each SMX contains 192 single precision CUDA cores, 64 double precision units, 32 special function units (SFU) for fast approximate trascendental operations, and 32 load/store units (LD/ST). Threads are scheduled in groups of 32 named warps and each SMX includes four warp schedulers that allow for four warps to execute concurrently. Developers can avoid to think about warp execution from an output correctness standpoint but computational performance is significantly improved if threads in the same warp execute the same code path and access contiguous memory.

CUDA Programming Model

The portion of code that runs in parallel on the GPU cores is called a kernel. Kernels invoked by CUDA code execute on a generally large number of parallel threads and each thread executes an instance of the kernel. Threads must be organized by the developer into thread blocks, which compose a grid of threads as illustrated in Figure 1.12.

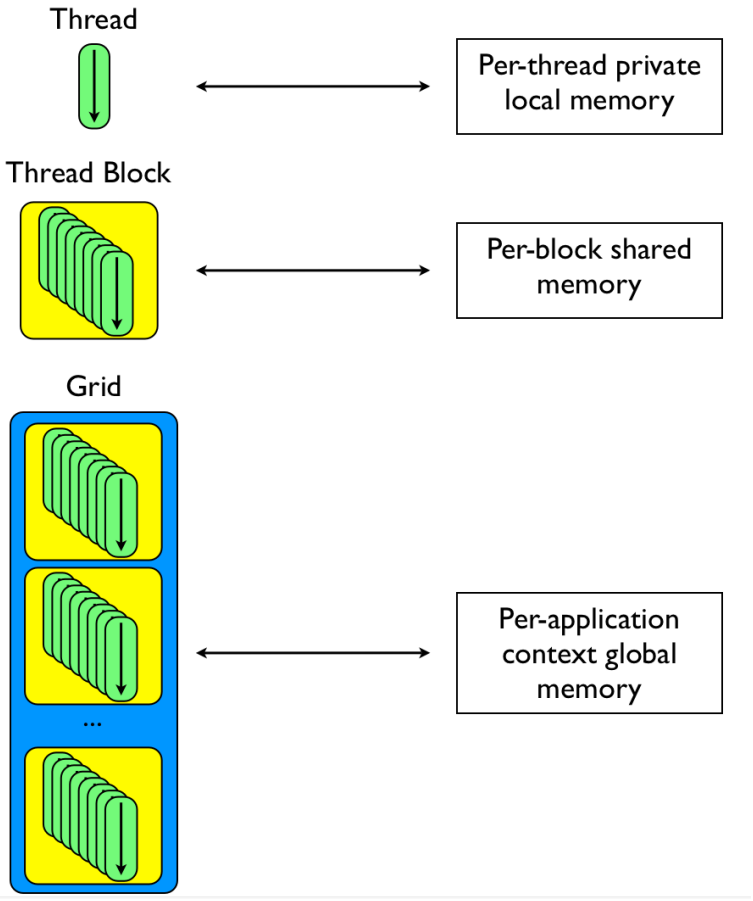

Figure 1.12: Thread hierarchy. Threads are grouped in blocks, which compose a grid.

Threads have their own private memory and registers but have also access to a per-block shared memory region that can be used for inter-thread communication or data sharing, a global device memory region generally used to read inputs and write results and a constant memory region that can only be read by code running on GPUs Figure 1.13.

To perform computations on the GPU, the following steps are required:

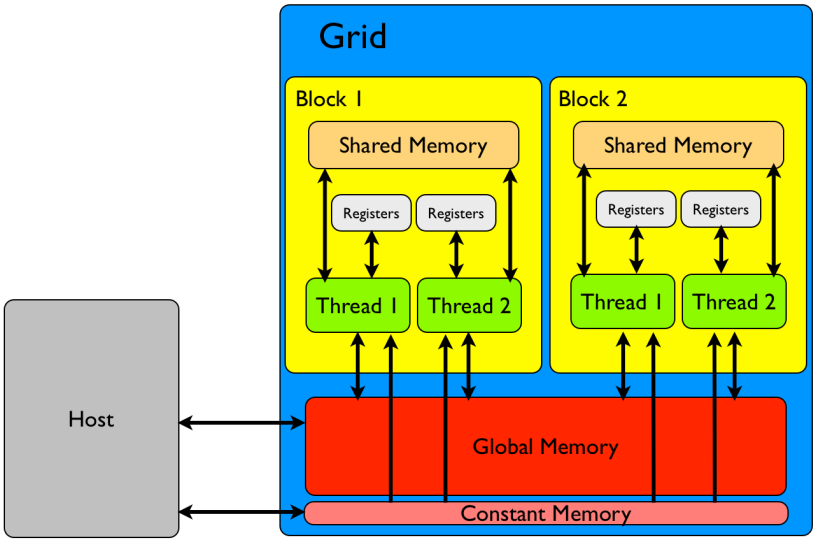

Figure 1.13: CUDA memory structure from a developer point of view. Different threads have access to different memory regions. While all threads have access to global memory and shared memory of the block to which they belong, each thread also has access to a unique small portion of private memory and registers.

- Copy input data from host memory (RAM) to device (global) memory;
- Launch the kernel;
- Copy back the results from device memory to host memory.

Since CUDA 6, a unified memory space that includes boh RAM and device memory is available but manual management of device memory is still more efficient thus it is adopted throughout this work.

Threads are then mapped to physical processors on the GPU. Each GPU can execute more than one kernel grids (if enough resources are available), a streaming multiprocessor (SMX) can execute one or more blocks and individual CUDA cores elaborate thread instructions. The different speed of the various memories present on the GPU can be exploited for optimization of the CUDA code. Specifically, registers and shared memory are much faster than global device memory.

1.4 Considered EBI Applications

In this work, stroke and epileptic foci localization have been selected as case studies to compare the performance of the developed EIT reconstruction algorithms while Visual Evoked Potentials (VEP) experiments have been considered to evaluate the performance of the optimized EEG source localization implementation.

1.4.1 Stroke

Stroke is a life-threatening medical condition which is characterized by loss of brain function due to disruption of blood perfusion. In an ischemic stroke, the blood supply to a brain region is reduced or completely cut off [31]; conversely, in a hemorrhagic stroke blood floods the region adjacent to the leakage of a vessel [32]. Both conditions can lead to severe brain damage, and stroke is the second single most common cause of death in Europe [33] and the fourth leading cause of death in the U.S.A. [34].

Nowadays, stroke is diagnosed mainly by means of X- ray Computed Tomography (CT) and Magnetic Resonance Imaging (MRI), techniques which yield structural information about the tissues of interest. Conventional CT and MRI scans are only able to detect brain injury several hours after stroke onset while specialized acquisition protocols, such as diffusion weighted imaging (DWI), perfusion weighted imaging (PWI) and magnetic resonance angiography (MRA), can detect an anomaly

within minutes of its genesis [35]. All the available techniques share the disadvantages of high costs, no portability and significant geographical inequalities of availability. Early recognition is crucial for therapy since, if an ischemic condition is detected within 4.5 hours of onset, it is possible to initiate treatment with Tissue Plasminogen Activator (tPA), a clot-busting therapeutic agent [36]. At the same time, discrimination is fundamental since treatment of a hemorrhagic condition by tPA is likely to result in additional damage to the patient [37].

Stroke is known to alter the conductivity of brain tissues: during ischemia the decreased extracellular volume due to cellular swelling (cytotoxic edema) reduces the average conductivity of the affected region [38]; on the other hand, when intracranial bleeding occurs, the average conductivity of the flooded region increases significantly due to the higher conductivity of blood with respect to cerebral tissue [39]. Hence EIT might be deployed in emergency situations in which MRI and CT scans are not an option due to the physical dimension of the scanner and its cost. For example, on ambulances or in remote areas, a preliminary EIT scan might be performed when a stroke is suspected in order to support the diagnosis and discriminate between a hemorrhagic and an ischemic condition. A cap with up to 128 active electrodes, similar to the ones used in electroencephalography (EEG), could be applied to the patient within minutes [40] and, considering about 20 minutes of computing time which will be shown to be reasonable using the technology presented in this work, the whole acquisition and reconstruction process might be completed in less than thirty minutes. Since the information that needs to be processed in order to detect and classify the stroke consists in a reduced number of measurements, a few kilobytes of data in a typical situation, the computing platform could be located off-site and accessed remotely.

1.4.2 Focal epilepsy

Epilepsy is a neurological disorder that affects about one person every 2000 each year. From a physiological point of view, it can be characterized by a sudden onset of abnormal electrical activity in the gray matter portion of the brain. This aberrant activity manifests itself as seizures. In most cases anti-epileptic drugs are able to manage this pathology, as they both cause the seizure to end and prevent it from spreading to other areas of the brain, through the inhibition of the accelerated activity of the neurons.

However, in approximately one third of the patients, pharmacological treatment is ineffective [41] and, in this specific subgroup, about half of the subjects is affected by focal epilepsy, a particular type of

epilepsy in which only a limited part of the brain, the epileptogenic zone, initiates the abnormal electrical activity.

In these cases, the surgical removal of the epileptogenic focus can be a viable option to effectively cure the patient [42]. To this end, the precise identification of the regions which need to be removed is essential to both effectively cure the disease and avoid the resection of the eloquent cortex, i.e. areas of the brain involved in important functions such as motor control, language or memory. Noninvasive brain imaging techniques, like PET, SPECT, EEG, MRI and fMRI, are routinely used in this framework to accurately locate the lesion and define the surgical plan. When definitive localization cannot be achieved by noninvasive methods, invasive EEG recordings can be performed using intracranial stereoelectroencephalography (SEEG) to directly measure the potentials generated by deep cortical regions. Then, a trained physician analyzes the raw EEG measurements with information about contact positions to determine the source of epileptic activity.

Recent research highlights a 10% increase in the impedance of seizing cortex when compared to non-seizing gray matter and this constitutes a contrast which may be detectable with EIT techniques. Impedance imgaging may thus provide a completely new source of information for epileptic foci localization and in this work its feasibility is tested in simulation.

1.4.3 Event Related Potentials

Event Related Potentials (ERP) refers to a standard neurological test that evaluates the brain response to specific events or stimuli [43]. They manifest themselves as modifications of the electroencephalographic signal that are time-locked with the event that elicited them and thus provide a noninvasive way of studying psychophysiological correlates of mental processes.

Early waves, that peak within the first 100 ms from the stimulus, show a higher dependence on the event that induced them and thus are referred to as sensory or exogenous, while later peaks are named cognitive or endogenous as they are connected to the processing of the information by the subject [44]. ERP can be either positive, like the P300 wave, recorded between 250 and 400 ms after the stimulus, that is associated to the speed of classification and discrimination of the event or negative as the N100 deflection that is generally observed 100-250 ms after an unexpected stimulus. Modifications in the amplitude and latency of these waves have been associated to a number of psychiatric and neurotic disorders like schizofrenia [45], depression [46], panic disorder [47] or obsessive compulsive disorder [48].

Visual Evoked Potentials (VEP) are a particular kind of ERP in which visual stimuli are employed to elicit a cerebral response which can be detected with scalp electrodes.

Given their extensive characterization in the literature, visual evoked potentials (VEP) experiments will be considered in the following to evaluate the performance of the implemented EEG source localization algorithms.

Chapter 2

Electrical Impedance Tomography

In this chapter the focus is on Electrical Impedance Tomography. This imaging technique is able to retrieve structural information about the subject's brain through the reconstruction of a conductivity map of the domain, due to the differences in the electrical properties of the various tissues which compose it. Beside a formal definition of the problem, two algorithms for its solution are presented. One is the Tikhonov Regularized inversion, which, being widely used in EIT imaging, can be considered a benchmark for the evaluation of other methods' performances. The other is a novel algorithm, named PAR, that is characterized by significantly lower computational cost and can be used to detect conductivity contrasts with high efficiency.

After the technical description of both methods, their results are compared thoroughly on two different reconstruction domains. In the first one a cylindrical phantom containing saline solution is used as a simplified model and non-conductive contrasts of varying dimensions constitute the targets to be detected. Successively, both methods are applied to the problem of stroke detection and classification using simulated head domains representing different physiological and pathological conditions with various levels of uncertainty (noise).

This analysis led to the validation of PAR and the identification of this method as more suited than the Tikhonov Regularized inversion for the quick detection and identification identification of a varying number of compact conductivity contrasts in complex 3D domains.

In the last section of this chapter an innovative application of EIT is considered. It involves the identifiation of the brain region which initiates an epileptic seizure (i.e. the epileptic focus) by exploiting data recorded with needle-like invasive electrodes. Once localized, the

epileptic focus can be surgically resected to alleviate symptoms. EIT may constitute a completely new source of information for epileptic foci detection and potentially improve the localization accuracy which can be achieved. At first, anovel algorithm for segmentation of deep intracranial electrodes from volumetric MRI scans of the head is introduced. Then, EIT reconstructions and an analysis of the influence of current injection patterns on reconstruction quality is performed. The outcome is then used to suggest a standard protocol for current injections with intracranial electrodes which would grant an accurate conductivity map reconstruction.

2.1 Background

Electrical impedance tomography is a cost effective electrical imaging method that enables the reconstruction of an impedance map of the region of interest starting from measured electric potentials generated by a set of current injections.

There are mainly three different ways in which it is possible to generate images starting from measured electric potentials: absolute, time difference (TD) and frequency difference (FD) reconstructions. In the absolute reconstruction method, the initial guess conductivities of the electrical model representing the domain of interest are updated considering a single set of measured electric potentials. This approach is generally applicable but has a very significant disadvantage: it is highly sensitive to inaccuracies of the electrical model and to measurement noise.

To try and reduce the impact of errors, the TD approach is based on two different electric potentials measurements acquired at different time instants. This method allows to image the change in impedance which happens between the first measurement (baseline) and the second one and is applicable whenever the impedance is time-dependent and when it is possible to acquire a baseline measurement. In such cases, noise due to imperfections in the electrical model of the domain and part of electrical noise are present equally in the baseline and the second measurement, thus they cancel out and the reconstruction quality is markedly improved when compared to absolute reconstruction methods.

A similar approach is the frequency difference method, where the electric potentials are measured not at different time instants but at different frequencies almost simultaneously. The main drawback is that the technique is not always applicable since the impedance of some materials only has a negligible dependance with respect to frequency.

This approach provides a smaller reduction in sensitivity to errors when compared to TD because the errors due to uncertanties in the electrical model of the head on the measured potentials propagate differently at different frequencies.

In many biomedical EIT applications, like the identifiction of solid tumors, the diagnosis of localized variation in blood perfusion or the identification of intracerebral strokes, the goal consists in the detection and approximate localization of a compact conductivity variation that is surrounded by an electrically uniform background . Due to the nature of the diagnosis process, baseline measurements (healthy state) are generally not available. For this reason, time difference (TD) imaging is not an option and absolute or frequency difference (FD) algorithms, which are more sensitive to modeling and measurement errors when compared to TD [49], may be employed. The problem with FD approaches is that some electrical properties of tissues, such as blood conductivity, show negligible dependence on frequency thus their application to stroke classification is very difficult.

In the following, a new parametric approach to reconstruction (PAR) is presented and its main advantages with respect to standard absolute reconstruction, speed and robustness to noise, are highlighted.

Starting from an electrical model of the domain, the head in our case, to reconstruct an impedance map of the region of interest, two different computational modules must be in place: a forward and an inverse problem solver [50].

2.2 Electrical Model

The electrical model defines the reconstruction domain and specifies:

1. the positions of the different tissues that compose the domain;
2. the electrical properties of each tissue;
3. the position and number of electrodes.

Structural information about the position of the different head tissues can be obtained starting from a MRI scan of the head. A MRI scan is composed of a series of images, thin slices, that can be combined to obtain a three dimensional volume.

The domain is discretized with a structured hexahedral mesh, this allows for a direct mapping between the acquired MRI scan of the head, which specifies a grayscale value for each hexahedral voxel of the volume, and the electrical model.

Open source tools, such as Brainsuite [51], can be used to segment the MRI scan in order to obtain precise information about the spatial distribution of the different tissues that compose the head. The user can tune the various parameters of the segmentation algorithm to obtain best results for each individual subject. Moreover, the gray and white matter region of the brain are parcellated according to standard neuroanatomical regions.

As the composition of each kind of tissue is different from the others, so are its electrical properties. Precise information about the electrical properties of biological materials at different frequencies can be found both in online databases [52] and in the literature [53] [54].

For our purposes, the head model is considered to be composed of six different tissues, namely skin, bone, connective tissue, cerebrospinal fluid and brain (composed of white matter and gray matter) (see Figure 2.1).

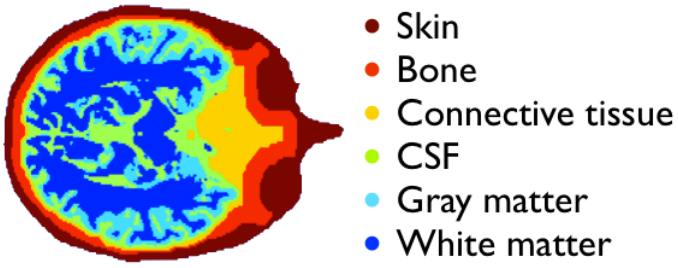

Figure 2.1: Graphical representation of the electrical model of the brain.

2.2.1 Electrode Positioning

Once the electrical model of the head specifying the precise location and conductivity of the different tissues is constructed, the position of voltage recording and reference electrodes on the scalp must be specified. Two different electrode-positioning routines have been developed in order to obtain either a uniform electrode distribution, in which electrodes are placed on the scalp at approximately constant distance from each other (Figure 2.3 (a)), or an electrode distribution that matches the one on an EEG cap (Figure 2.3 (b)).

Uniform Distribution

To mantain an approximately constant inter-electrode separation, electrodes are initially uniformly distributed on top of a semisphere centered on the head and then projected onto the scalp.

The spherical coordinate system is used Figure 2.2 to place each electrode in the corresponding point on the semisphere surrounding the head. The radius of the semisphere is then iterarively reduced until the electrode touches the skin.

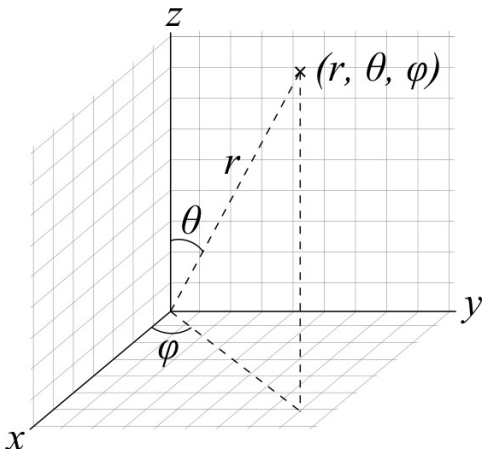

Figure 2.2: Spherical polar coordinate system.

EEG cap

The function to place electrodes on the scalp according to the position of an EEG cap is similar to the previous one, but in this case the angles at which electrodes are placed do not depend on the specified inter-electrode distance but are drawn from the specifications of the EEG cap that are provided by the manufacturer.

2.3 Forward Problem

The forward problem yields the voltage distribution in the volume of interest, given the applied current and the physical properties of the domain. It can be formalized as a Poisson problem in the quasi-static case with Neumann boundary conditions [55] (system of equations 2.1).

$$\begin{cases} -\nabla \cdot \sigma \nabla \phi = 0 & \text{on } \Omega \\ \iint_{S_i} \sigma \nabla \phi \cdot \hat{n} dS = \iint_{S_i} g \cdot \hat{n} dS = I_i & \text{with } i = 1 \cdots N_e \\ \sigma \nabla \phi \cdot \hat{n} dS = 0 & \text{on } \Omega / \cup_{i=1}^{Ne} S_i \end{cases} \tag{2.1}$$

where σ is the local conductivity of the medium and ϕ is the local electric potential. One convenient approach is to assume σ to be

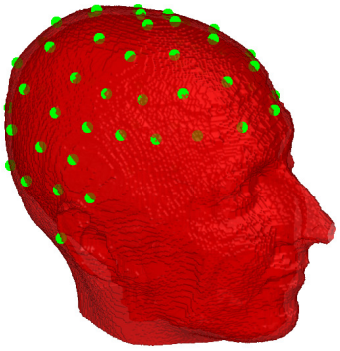

(a) 64 electrodes positioned on the subject's scalp, approximately uniform distribution of inter-electrode distance.

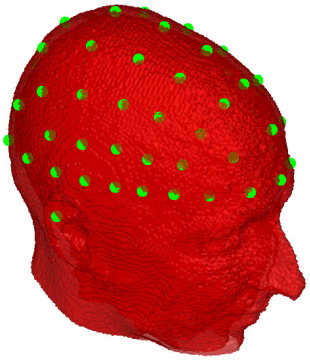

(b) 64 electrodes positioned on the subject's scalp according to the positions of a standard EEG cap.

Figure 2.3: Electrode positioning outcomes.

piecewise constant in each voxel of the discretized volume Ω. In the second and third equation, g is the local current density, $\hat{n}$ is the versor normal to the surface of the electrode, and I_i is the current injected in the i-th electrode of area S_i. The second equation defines the current that flows through each of the N_e electrodes placed on the scalp. The third one specifies that the only current that flows across the boundary is the one injected by the electrodes.

Given the electrical model, it is possible to solve the Poisson problem locally in each corner (node) of the voxels. The finite volume method (FVM) is the method of choice due to the fact that the mesh deriving from a MRI scan is regularly structured and each cubic voxel maps to an element. Considering the formulation described in [56], the problem can be expressed as a linear system:

$$B \cdot \phi = I \tag{2.2}$$

Where B is a symmetric non-hermitian structured matrix with 7 bands in the isotropic case, ϕ is a vector of electric potentials at each node of the discretized volume and I specifies the injected currents.

2.4 Inverse Problem

The inversion method makes use of the forward problem solver to provide an estimate of the physical properties of the volume given the stimulation pattern and the set of measurements.

The reconstruction of an image of the brain starting from EIT data is an exceedingly complex problem that is characterized by both a significant under-determination and a severe ill-posedness. Most of the methods currently employed apply a least square minimization procedure to a regularized functional, in which a penalty term is used to favour smooth conductivity variations (L2-norm) or the reconstruction of piecewise constant conductivity regions (L1-Norm). Among the approaches that use the former, the most notable example is the Tikhonov Reconstruction (TR) in which the penalty term includes a regularization matrix, which can be defined as approximations of differential operators [57] or the identity matrix [58] or even structural priors [59]. Other regularization strategies, like the Total Variation [60] or the sparsity regularization [61],[62], apply the L1-Norm, while approaches developed for more specific applications (Subdomain Methods [63],[64],[65]), improve the accuracy of the result by including prior information about the domain or by limiting the region to be reconstructed. In the past, the back projection algorithm [66], that is derived from the Radon transform and is commonly used for the analysis

of computed tomography data, was applied to EIT reconstruction, together with the Landweber method that was obtained modifying the generalized inverse matrix method [67]. Recently developed methods, on the other hand, are able to take into account modeling errors through the application of advanced statistical methods [68],[69]. At present, Tikhonov Reconstruction can be considered the most widely employed approach and it is generally used as a benchmark for evaluating the performances of newly developed algorithms in this field [61], [70].

	Voxel by voxel	Regularized	Computational cost	Applications
Backprojection	Yes	No	Low	Obsolete
Landweber	Yes	No	Medium	Obsolete
Tikhonov	Yes	Yes	High	General
Total Variation	Yes	Yes	High	Preserve edges
Sparsity	Yes	Yes	High	Preserve edges
Subdomain	Yes	Yes	High	Use prior info.
Bayesian	Yes	No	High	Increase contrast

Table 2.1: Comparison table of EIT inversion methods

2.4.1 Tikhonov Regularized Inversion

The aim of EIT imaging is to determine the conductivity of each voxel within the domain; it corresponds to the solution of an ill-posed problem, that has an infinite number of solutions. The identification of a single conductivity map thus requires the introduction of additional knowledge. In the TR inversion [57], the most widely used EIT reconstruction strategy, an additional term is added to the error function, that aims to favour the most regular solution.

$$E(\sigma) = \|V_m - V_g(\sigma)\|^2 + \|\Gamma \cdot \sigma\|^2 \tag{2.3}$$

where V_m are the measured surface potentials, V_g are the computed surface potentials with an initial guess conductivity distribution σ_0 while the regularization matrix $\Gamma = \lambda \cdot M$ is composed of a regularization parameter, λ, and a matrix M. The latter is constructed as a discrete Laplacian filter to enhance the smoothness of the reconstruction [59] while the former is selected by locating the point of maximum curvature on the L-curve generated by a one-step linear Gauss-Newton solver [71]. The L-curve is constructed by plotting the norm of the solution versus the seminorm of the residual vector parametrized by

the regularization parameter. The value of the regularization parameter that corresponds to the corner of the curve constitutes the best tradeoff between minimizing the solution norm and the residual and for this reason it generally yields the best reconstruction quality.

The iterative reconstruction stops when a local minimum of the error function is reached or the maximum number of iterations set by the user is met. The effect of the regularization is to favour the reconstruction of compact contrasts through the penalization of gradient variations. In the following M and the reconstruction process will be restricted to the brain and the CSF. This is because the TR inversion will be applied to the detection of a stroke, that does not affect scalp, skull and connective tissue and can be identified as a compact conductivity variation with respect to the surrounding region.

The error function in Equation 2.3 is generally minimized under the linear approximation [72]. This results in the following equation

$$\Delta\sigma = (J^T \cdot J + \Gamma^T \cdot \Gamma)^{-1} \cdot (J^T \cdot (V_m - V_g)) + \Gamma^T \cdot \Gamma \cdot (\sigma_r - \sigma_n) \quad (2.4)$$

Where $\Delta\sigma = \sigma_{n+1} - \sigma_n$ is the conductivity update, σ_r is a reference conductivity distribution and σ_n is the reconstructed conductivity distribution at step n.

The Jacobian matrix J can be computed by exploiting the reciprocity principle [73].

J is a rectangular $[N_i \cdot (N_e - 3)$ x $N_v]$ matrix, where N_i is the number of injections, N_e is the number of electrodes and N_v is the number of voxels which compose the domain. It is important to observe that, for each injection, two electrodes inject current and one is used as a reference, thus the number of measuring electrodes is $N_e - 3$.

Computation of J can be performed through a finite difference approach, in which the conductivity of each voxel is varied by a small amount and the resulting variation in the electrode potentials is evaluated. This procedure would require the solution of one forward problem for each voxel of the discretized volume and would become infeasible if the voxel number exceeds the hundreds. A segmented MRI scan acquired with a 3 Tesla machine is composed of voxels of about $1mm^3$ in volume and a whole head consists of more than 2 million voxels. A better approach is to compute the Jacobian at each iteration by exploiting the reciprocity principle:

$$J_{i,j} = \frac{dV_i}{d\sigma_j} = -\frac{1}{I} \int_{\Omega_j} \nabla\Upsilon(\sigma_j) \nabla\Psi_i(\sigma_j) d\Omega \quad (2.5)$$

Where Υ is the potential distribution generated by the actual injection pattern and Ψ_i is the potential distribution generated by an artificial current injection which takes place between the i-th measuring electrode and a reference electrode [73]. The result is the variation in the potential on the i-th electrode dV_i when a $d\sigma_j$ is applied to the volume Ω_j.

This technique reduces the number of forward problem solutions needed to calculate the jacobian matrix from $N_i \cdot (N_v + 1)$ to $N_e \cdot N_i$.

Due to the significant difference between the electrical properties of the healthy brain tissue and that of the region affected by a stroke, it is possible to use an iterative reconstruction process that updates the initial guess conductivity distribution σ_0 until either the difference between two consecutive iterations drops below a threshold or the maximum number of iterations is reached. Each step of the simulation consists in computing the Jacobian and solving the linearized problem that leads to the determination of the contribution $\Delta\sigma$ that is then used to update the conductivity distribution.

Once the image has been reconstructed, the conductivity anomaly is automatically identified by means of an automated segmentation procedure that uses a threshold equal to 75% of the maximum variation from the initial guess condition. This approach is able to identify all the conditions of interest since a stroke is characterized by a significant variation of conductivity, that increases in case of an hemorrhagic stroke and decreases for an ischemic one; while the electrical properties of a healthy brain are homogeneous enough to remain undetected. The segmentation is followed by a feature extraction procedure which computes the volume of each recognized contrast. The final image is then filtered to remove spurious lobes, identified as contrasts with a volume which is less than 20% of the largest detected object. By considering only thresholds above a minimum expected contrast, it is possible to correctly classify also the absence of a target.

Finally, if the conductivity variation in all the segmented regions has the same direction, that is if they are all characterized by an increase or decrease of conductivity with respect to the background, a stroke is detected and opportunely classified. A healthy condition, on the other hand, is characterized by the inability of the procedure to detect a target.

2.4.2 Parametric Approach to Reconstruction (PAR)

Reconstruction methods that aim to determine the conductivity of each point (voxel) of the domain are generally associated to a high computational cost and the necessity to identify a regularization parameter,

whose value may significantly influence the result. To address these limitations, a parametric approach to reconstruction (PAR) was developed. This method is less general, since it avoids the complete reconstruction of the conductivity map, but is able to efficiently recognize compact conductivity variations. This makes it applicable to many different situations where the goal is fast detection and classification of conductivity contrasts, independently of their exact shape.

The reconstruction process consists in updating the position and properties of a first-guess anomaly until either a target is identified or no irregularity is detected. The initial compact conductivity variation is positioned within the domain and its size and electrical properties are set to plausible values for a stroke condition.

To better understand the functioning of the proposed algorithm, the description will be initially restricted to the simplified 2D domain of Figure 2.4, consisting of a uniform disk with sixteen equally spaced electrodes placed on its boundary and a punctiform target anomaly that has a conductivity slightly different from the background. The stimulation pattern considered in the following is the so-called opposite injection pattern, which has been demonstrated to maintain good sensitivity even far from the electrodes in the central region of the phantom and in presence of measurement noise [74]. This injection pattern consists in using two opposite electrodes as entry and exit points for the current, while all the non-injecting electrodes measure the surface potentials. In this simplified case, eight independent opposite current injections are possible: in the first one the current flows between electrode 1 and electrode 9, in the second one between electrodes 2 and 10 and so on, until all pairs of opposite electrodes have been considered. The total number of measurements for this example is 104 because, for each injection, 2 electrodes are creating the current flow, one is used as a reference and 13 are recording [75].

In this domain, for each injection, the forward problem takes the form $-\sigma\nabla^2\phi = 0$, with Neumann boundary conditions. The solution can be computed analytically to be:

$$\begin{cases} \phi(r,\theta) = \sum_{n=0}^{\infty} r^n \cdot [A_n \cdot cos(n\theta) + B_n \cdot sin(n\theta)] \\ A_0 = \text{free} \quad , \quad A_n = \frac{1}{\pi n R_0^{n-1}} \cdot \int_0^{2\pi} k(\theta) cos(n\theta) d\theta \\ B_n = \frac{1}{\pi n R_0^{n-1}} \cdot \int_0^{2\pi} k(\theta) sin(n\theta) d\theta \end{cases} \tag{2.6}$$

Where R_0 is the radius of the disk and $k(\theta)$ are the boundary conditions:

$$\begin{cases} k(\nu) = -1 \quad , \quad \nu = \frac{\pi}{8}, \frac{\pi}{4}, \cdots, (1 - \frac{1}{8})\pi \\ k(\nu + \pi) = 1 \end{cases} \tag{2.7}$$

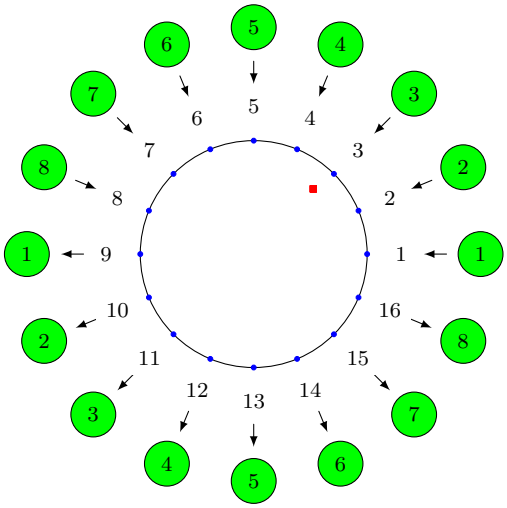

Figure 2.4: 2D depiction of the simplified domain. The anomaly (red rectangle) is represented as a single voxel in which the conductivity is different from the background. The blue circles at the edge of the domain identify the position of electrodes, each associated to a progressive number, while the outernmost numbers circled in green together with the arrows identify the eight independent opposite injections.

To detect a target starting from an initial guess punctiform conductivity variation, the solver updates its coordinates until its position corresponds to that of the target. To do so it minimizes the 2-norm of the difference between potentials measured at the electrodes when only the target anomaly is present, V_t, and the ones obtained when only the moving anomaly is placed in the first guess position, V_g:

$$E = \|V_t - V_g\|^2 \tag{2.8}$$

Given the non-linearity of the minimization problem, as a first step the surface potentials are linearized: $V_t = V_g + J_p \cdot \Delta p$, where $\Delta p = [\Delta x \quad \Delta y]$ represent the variation of spatial coordinates while $J_p = [J_{px} \quad J_{py}]$ is the Jacobian. This variable characterizes the relation between the variation of the surface potentials, recorded with the electrodes and Δp, thus leading to the following equation for an update step of the iterative solver:

$$\Delta p = (J_p^T \cdot J_p)^{-1} \cdot J_p^T \cdot (V_t - V_g) \tag{2.9}$$

Assuming that the conductivity variation $\Delta\sigma$ from the background conductivity value is small, it is possible to write:

$$\begin{cases} V_t = V_0 + J \cdot \Delta\sigma(x - x_t, y - y_t) \\ V_g = V_0 + J \cdot \Delta\sigma(x - x_g, y - y_g) \\ J_{px}(x, y) = J(x + \Delta x, y) - J(x, y) \\ J_{py}(x, y) = J(x, y + \Delta y) - J(x, y) \end{cases} \tag{2.10}$$

where (x_t, y_t) is the position of the target, (x_g, y_g) is the position of the guess, $\Delta\sigma(u, v) = d\sigma$ for $u = v = 0$ and $\Delta\sigma(u, v) = 0$ otherwise. V_0 are the potentials sampled at electrode positions when both target and guess anomalies are absent ($\sigma(x, y) = \sigma_0$). The efficiency of the jacobian computation $J_i(x, y) = \frac{dV_i}{d\sigma(x,y)}$, which defines the relation between the potential variation at the i-th electrode and the conductivity variation in (x,y), can be greatly increased by applying the reciprocity principle which significantly reduces the computational cost of the operation. The computation of Δp in each point of the domain produces a map that defines the direction and amplitude of the movement of the guess anomaly at the following iteration (Figure 2.5). If the sign of the guess conductivity variation matches that of the target (panels (a) and (b) in Figure 2.5), a basin of attraction is generated and the guess anomaly is pushed towards the target. In contrast, opposite conductivity variations of target and guess will generate a repulsor (panels (c) and (d) in Figure 2.5) which tends to move the guess away from the target. Similar results may be achieved independently of the target's position.

The same approach is applied when a 3D domain is considered. The only difference is in the number of variables that need to be reconstructed. Indeed the radius and position of the guess anomaly (probe) and the conductivity of the five background tissues (scalp, skull, connective tissue, CSF and brain) must be included in the complete algorithm for the considered case study of stroke detection and discrimination. The electrical properties of head tissues are initially set according to literature data, while a spherical wandering probe, approximating the generic structure of a compact conductivity contrast, is placed at a first-guess position within the domain with a guessed radius and conductivity variation. Even though a spherical probe is used to approximate the target, it is important to note that there is no requirement relative to the shape of the target conductivity variation.

The reconstruction is obtained using an iterative linearized solver that applies Equation (2.9) to determine Δp, a vector containing the variation of the various reconstructed properties with respect to the previous iteration. In the considered case study, it is a nine values vector which contains the conductivity variation of each head tissue,

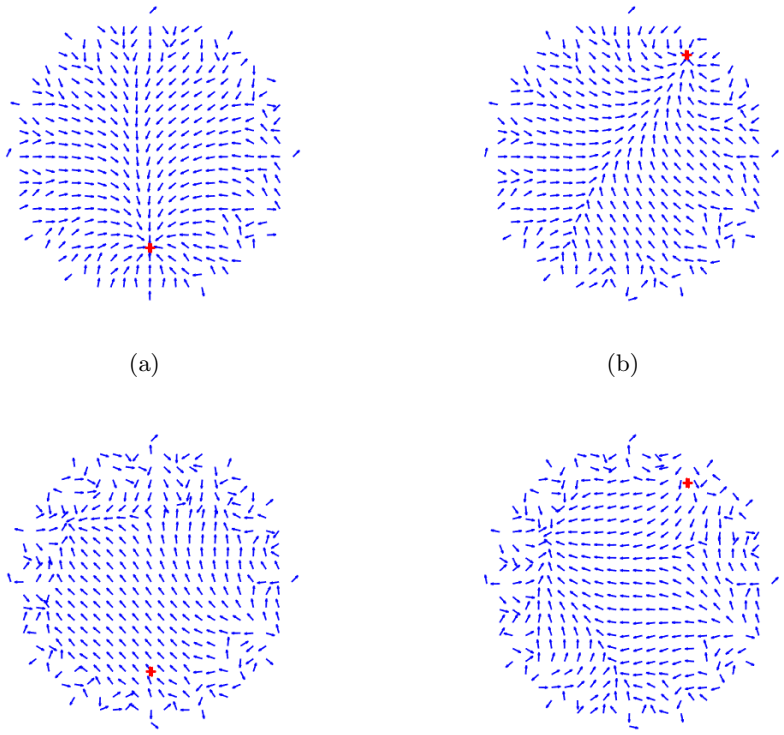

Figure 2.5: Representation of the basins of attraction or repulsion which drive the moving anomaly respectively towards the target (marked as a red plus) or away from it. In (a) and (b) the initial conductivity variation has the same sign as the target and an attractor is generated. In (c) and (d), on the contrary, the conductivity variation of the target is opposite to that of the anomaly and so the latter will be pushed away from the former, resulting in a repulsor. In this representation two possible target positions are considered (first and second row). The arrows, on the other hand, have been represented with the same length, for clarity of representation.

considered homogeneous, and the variation in position and radius of the probe.

Given the limited number of properties that can vary, in this case the Jacobian is computed with a finite-difference approach (see Figure 2.6 and Equation 2.11) where the minimum spatial variation was set to 1 voxel and the minimum conductivity change of background tissues to 1% of the current iteration value.

$$J_{i,k} = \frac{\phi_i(p_k + \Delta p_k) - \phi_i(p_k - \Delta p_k)}{2\Delta p_k} \tag{2.11}$$

Where ϕ_i denotes the electric potential computed at the i-th measuring electrode location, p_k is the k-th property and Δp_k is a small variation of the k-th property.

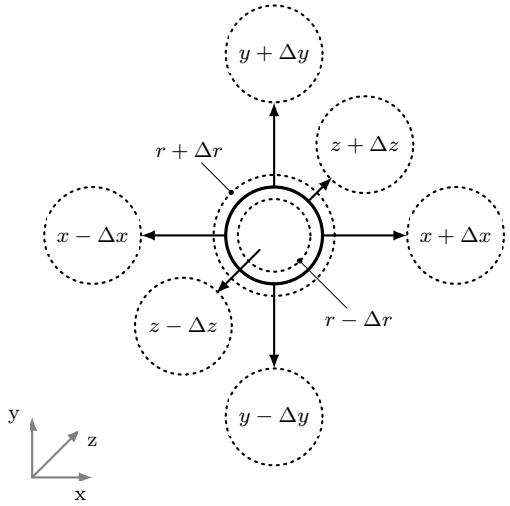

Figure 2.6: Graphical representation of the construction of the Jacobian. The black circle represents the probe, identified by its current position and size, while the dotted lines identify the possible positions and sizes of the conductivity variation used to compute the Jacobian matrix.

The wandering probe is subjected to specific constrains during the reconstruction process: its size must remain within a defined range and it must be positioned within the region of interest, that is it must overlap regions labelled as brain or CSF for at least 90% of its volume. If this condition is violated, the probe is moved toward the center of the head until the constrain is satisfied. Moreover, the radius of the probe has both upper and lower bounds. In particular, the radius of the guess anomaly reaching the lower limit is used as a stopping criterion identifying absence of the kind of stroke being examined.

In this algorithm two stopping criteria are defined: the first one is convergence, defined as a variation in size and position of the probe smaller than the spatial discretization step of the domain while the second one is divergence, which happens when the volume of the probe is reduced below a defined threshold. Finally, to guarantee the termination of the computation in a finite time, a maximum number of iterations is set as an additional stopping criterion. This third condition has been included to account for rare cases in which the wandering probe might be unable to exit a close circle around the target anomaly and thus fail to satisfy the first stopping criterion. The main steps of the proposed algorithm are depicted in Figure 2.7.

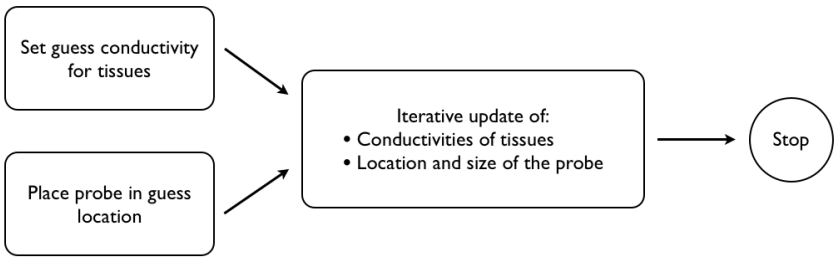

Figure 2.7: Main steps of the parametric reconstruction algorithm

At each iteration, a number of forward problem solutions need to be computed in order to construct the jacobian matrix and obtain the electric potentials at the measuring electrodes. For each forward problem computation, one of the most expensive operations turns out to be the construction of the B matrix of Equation 2.2.

Since, at each step, the conductivity distribution differs from the background conductivity only in a limited region defined by the current location and size of the wandering probe, it is possible to split the B matrix in the two different components of equation 2.12.

$$B = B_0 + B_c \tag{2.12}$$

where B_0 is a static matrix which describes a domain that doesn't contain any anomaly and B_c is calculated on a domain that includes only the difference between the probe's conductivity and the background. Thanks to this approach, B_0 is calculated only once and just the much lighter computation of B_c needs to be performed for each forward problem solution.

It was empirically determined that, for a realistic 3D head domain, four different locations of the guess wandering probe are required for

best detection and discrimination performance. This is due to the fact that, given a complex domain, the multidimensional landscape of error function is characterized by a number of local minima which could trap the wandering probe in a local dip and result in incorrect identification.

The discrimination between ischemic and hemorrhagic stroke is obtained by running, for each of the four initial probe positions, two different reconstructions. In the first one the wandering probe is assigned the electric properties of an ischemic stroke, while in the second they match those of an hemorrhagic one. These simulations, run in parallel, return eight residual errors that are ranked in increasing order. The lowest error, corresponding to the deepest minimum, is associated to the correct reconstruction.

2.4.3 Implementation

In Figure 2.8 are summarized the main steps of an EIT algorithm. Both TR and PAR follow this workflow and the definition of the electrical model is shared between the two reconstruction algorithms, developed in Matlab. Both approaches also exploit an optimized parallel forward problem solver for EIT developed by our research group. This method, presented in [52], uses the finite volume method (FVM) on a cubic mesh to solve the PDE and is coded in C and CUDA. The identification of the Jacobian and the inversion loop implemented for PAR, on the other hand, are not the same as the ones used by TR.

Since a stroke is generally characterized by local, compact anomalies with medium contrast, an accurate definition of the electrical model can significantly increase the quality of reconstructions. This information is then used to compute the surface potentials (V_g) that, together with the measured surface potentials (V_m), are used to compute $\Delta V = V_m - V_g$. The iteration is completed by the identification of the Jacobian and the solution of the inverse problem which leads to Δp. The outcome of the inversion step assumes two different forms, depending on the reconstruction algorithm considered. In TR it is a vector in which the conductivity variation of every voxel of the domain is specified, while in PAR it contains the conductivity variation of each tissue, assumed to be homogeneous, and the variation in spatial coordinates and radius of the anomaly. It is important to note that even in the parametric approach, all the variables that compose Δp are simultaneously reconstructed at each iteration. Finally, the satisfaction of the stopping criteria is evaluated. An affermative answer causes the algorithm to exit, otherwise the surface potentials and the Jacobian are updated and a new iteration is performed.

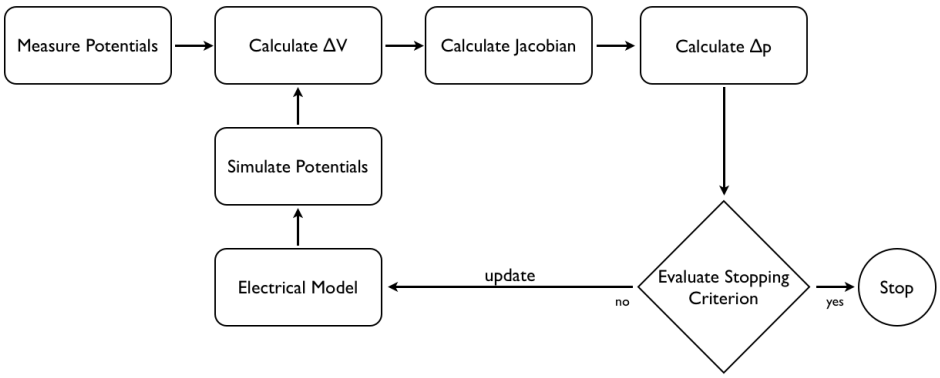

Figure 2.8: General structure of an iterative EIT inversion algorithm.

2.5 Phantom Experiments

To test the newly developed algorithm and compare it to TR, a phantom was built consisting of a cylindrical tank (see Figure 2.9) equipped with sixteen equally spaced metal electrodes on its border.

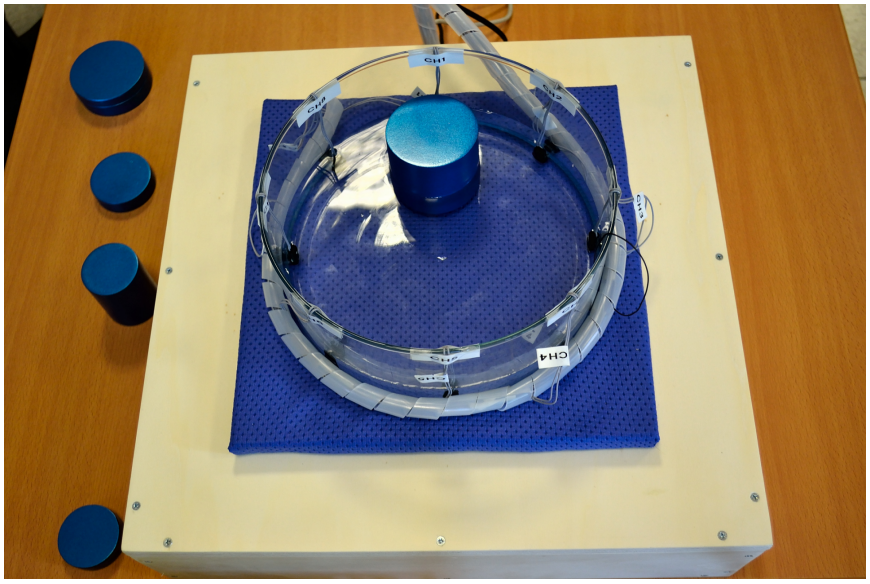

Figure 2.9: Cylindrical phantom containing saline solution ($\sigma = 0.25 \ [S/m]$) and a nonconductive anomaly (blue cylinder) placed inside the reconstruction domain. Nonconductive targets of different dimensions are visible on the left.

The electrodes are made of rectangular strips of aluminium tape

(590 Series, 3M, U.S.A.), while the tank is filled with saline solution. An Agilent 4294A impedance analyzer (Agilent Technologies, U.S.A.) connected to a 16048H port extension cable, is used to perform four-terminal impedance measurements and four different opposite sinusoidal current injections at a frequency of 32 kHz are considered (see first row in Figure 2.10). The acquisition settings, listed in Table 2.2, allow for an acquisition time of less than 100 ms for each data point and lead to a SNR of the impedance measurement at the terminals of 16048H of approximately 54 dB [76]. This value is comparable to those obtained with existing EIT systems [77], [18], while the the noise at the electrode-solution interface has been determined to be several orders of magnitude lower than the instrument noise, at the chosen frequency. For this reason, in the following, it will be neglected.

Property	Value
Bandwith Level	4
Frequency	32 KHz
Oscillator Level	500 mV
DC Bias Range	1 mA

Table 2.2: Acquisition settings of the impedance analyzer

Three different conditions are considered to compare the reconstruction performances of the two competing algorithms:

1. constant conductivity set to $\sigma = 0.25[S/m]$;
2. presence of a single uniform conductivity contrast ($\Delta\sigma = -0.25[S/m]$) with radius r = 24 [mm];
3. presence of two compact conductivity contrasts ($\Delta\sigma = -0.25[S/m]$) with radius r = 24 [mm];

When a single anomaly is considered, two alternative positions are tested, as shown in the first row of Figure 2.10. For this experiment the contrast consists of non-conductive cylindrical objects spanning the whole thickness of saline solution. Equivalent results have been obtained considering different background conductivities (in the range 0.15, 0.35 [S/m]) and targets simulating a partial decrease in conductivity with respect to the background, through the use of targets that did not reach the surface of the saline solution.

Four different conditions are considered: constant background conductivity ($\sigma = 0.25$ [S/m]); two different locations of a single compact, uniform conductivity variation ($\Delta\sigma = -0.25$ [S/m]) with radius r = 24

mm; and the simultaneous presence of two compact, uniform conductivity variations ($\Delta\sigma = -0.25$ [S/m] each) with radius r = 24mm (see Figure 2.10, first row).

2.5.1 Results

The results of the comparison are illustrated in Figure 2.10 where the first row reports the experimental condition, highlighting the position of the probe/probes and that of the electrodes.

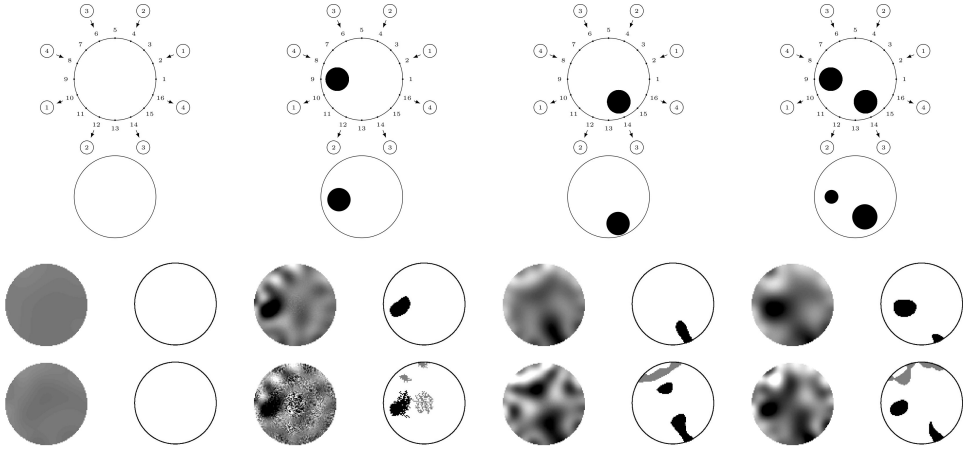

Figure 2.10: Experimental results obtained with the phantom shown in Figure 2.9. In the first row the experimental setup and the position of the non-conductive target/targets (black circles) is shown. The cylindrical tank is filled with saline solution and it features sixteen equally spaced electrodes on its border. These are used to sequentially apply four different current injections, that are here identified by the arrows. In the second row the results of the PAR reconstruction are reported while rows 3 and 4 show the ones obtained with TR. In this case both the conductivity map (on the left) and result of the post-processing procedure that identifies the anomalies (on the right) is shown. The difference between the last 2 rows is in the accuracy of the regularization parameter. In the first case (row three) it was optimized independently for every target position while in the second analysis a value equal to 20% of the optimum was used.

The reconstructions obtained with PAR when the conductivity variation set for the probe matches that of the actual target are shown in the second row of this image. Simulated experiments in which the anomaly was set to have an higher conductivity with respect to the background led to divergent reconstructions, thus enabling the identification of the correct solution.

PAR has been designed to be able to automatically identify the presence of more than one anomaly by means of successive reconstructions which take into account the position of the previously identified anomalies, thus preventing the multiple identification of the same target. When the addition of another probe leads only to divergent reconstructions, the process is interrupted. This can be better understood by considering the last column of Figure 2.10. In this case, the first and the second probe lead to convergent reconstructions, in which the wandering anomaly stops in a location within the domain and is characterized by a radius above the defined threshold. Performing the reconstruction with a third probe, on the other hand, leads to divergent outcomes for both initial guess conductivities of the wandering probe, thus concluding the reconstruction process.

The third row of Figure 2.10 depicts the results obtained with TR. In this analysis the regularization parameter was optimized for each target position. The reconstructed conductivity maps are shown on the left, where the dark shades of gray are associated to a conductivity reduction with respect to the background and light shades to a conductivity increase. On the right, the detected anomalies, extracted from the corresponding conductivity distribution with the developed post-processing procedure, are shown. In this regard, black identifies regions in which a significant reduction of the conductivity is detected, gray, on the other hand, labels conductivity increases with respect to the background. In this case both TR and PAR are able to correctly identify all the targets.

To highlight the importance of accurately tuning the regularization parameter (λ), the analysis shown in the third row of Figure 2.10 was repeated by assigning to λ a value that was reduced to 20% of the optimal. Errors of this entity, or even higher, are to be expected when the L-curve optimization is applied to complex domains characterized by important geometrical uncertainties [78]. These results, shown in the last row of Figure 2.10, are strikingly different from the ones above. A number of artifacts emerge in the conductivity map, some of which are then classified as anomalies, preventing a reliable determination of the number and position of the targets.

2.6 Simulated Head

Beside comparing PAR and TR using data acquired using the phantom previously described, stroke detection and classification on simulated head domains was considered. The electrical model is constructed as previously described and 128 electrodes are placed uniformly on the

surface of the scalp.

For this analysis the two main types of stroke (ischemic and hemorrhagic) were simulated using a single ellipsoidal anomaly placed at three alternative positions within the brain. Additionally the healthy condition, characterized by conductivities approximately uniform within each tissue and absence of a target, was considered.

In this comparison, three different stroke locations are considered in series. One target (P1) is positioned in the left hemisphere, between the parietal and occipital lobe. Then a stroke in the frontal lobe, slightly on the right side (P2) is modeled. Finally, another one is placed in the temporal lobe of the left hemisphere (P3). These conditions, represented in Figure 2.11, are characterized by a compact conductivity variation with elliptical shape and a volume of about $40cm^3$ [79]. Conductivities resembling both ischemic and hemorrhagic conditions are considered.

Four different sources of uncertainty are taken into consideration:

1. errors in tissue conductivity with resepect to literature values;
2. small conductivity inhomogeneities;
3. imprecision in the segmentation of the various head tissues;
4. electrical noise affecting the measured potentials.

The first one is modeled by adding a random variation to the nominal conductivity of each segmented tissue (σ_t in Equation 2.13). This term, identified with the symbol η in Equation 2.13 is distributed according to a gaussian probability distribution with mean zero and standard deviation 0.1 [54].

$$\sigma_t = \sigma_t + \eta \cdot \sigma_t \tag{2.13}$$

An additional term is then added to the conductivity of each voxel (identified as σ_j in Equation 2.14) to take into account small scale fluctuations of electrical properties within the same tissue. These inhomogeneities (ν in Equation 2.14) are characterized by a normal distribution with mean 0 and standard deviation 0.01.

$$\sigma_j = \sigma_j + \nu \cdot \sigma_j \tag{2.14}$$

Imprecisions in the segmentation, and thus in the shape of the head and tissue positioning, are accounted for by modifying about 2.5% of the boundaries between the segmented tissues. As a consequence, the electrical model used in the inversion step is structurally different from the one that is used in the forward problem solution. This procedure

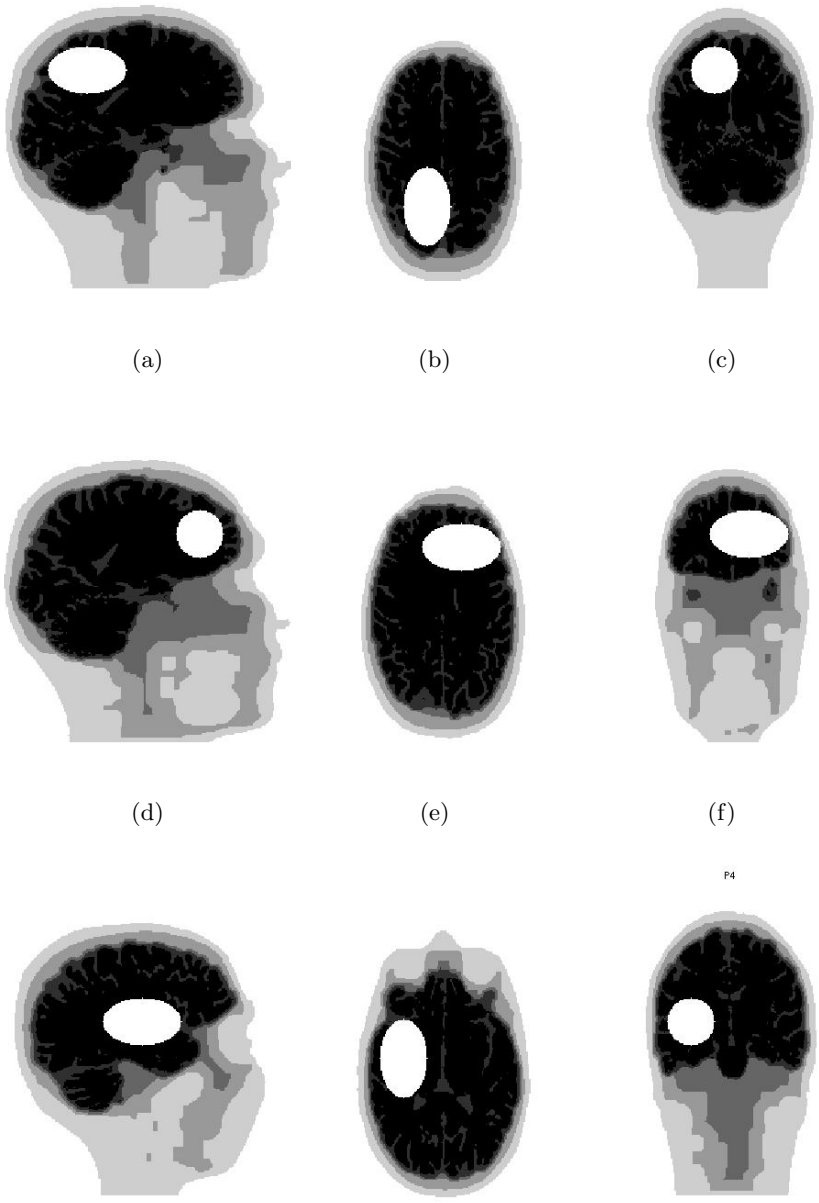

(a) (b) (c)

(d) (e) (f)

(g) (h) (i)

Figure 2.11: Sagittal (a), (d) and (g); transverse (b), (e) and (h); and coronal (c), (f) and (i) sections passing through the center of the three target locations considered.

can be exemplified as follows: the voxels in the first tissue which border the second tissue must be selected, together with the ones in the second tissue which are in contact with the first tissue. At this point, 2.5% of the border voxels are randomly switched to the neighboring tissue.

Finally, measurement noise is modeled as a random contribution, normally distributed with mean 0 and two alternative standard deviations of about 0.5% and 5% of the average amplitude of the simulated measurements. This is coherent with the method commonly used to test the robustness of EIT reconstruction algorithms to measurement noise, where a normally distributed noise between 0.1-10% of the amplitude of measured potentials is added [80],[65],[81]. If we consider our signal to be the potentials at the electrodes in presence of a stroke, the two noise levels, in the following defined as low and high, correspond to a SNR of about 48 and 28 dB respectively. This parameter, computed as the quadratic mean of the measurements referenced to the average, assumes a value dependent on the position of the anomaly and its conductivity, in case the signal is considered to be the potential variation at the electrodes caused by the stroke. These values are reported in Table 2.3 where P1, P2 and P3 refer to different positions for the anomaly.

	Low Noise	High Noise
P1 Ischemic	17	-3
P1 Hemorrhagic	15	-5
P2 Ischemic	25	5
P2 Hemorrhagic	22	2
P3 Ischemic	14	-6
P3 Hemorrhagic	19	-2

Table 2.3: SNR Stroke - No Stroke [dB]

2.6.1 Results

The two algorithms are compared considering both their detection and discrimination capabilities. Specifically, the percentage of conditions correctly classified as ischemic, hemorrhagic or "not detected" are used to characterize the performaces of PAR and TR. The results of this analysis are reported in Figure 2.12 where panel (a) reports the results relative to PAR and panel (b) the ones of TR. Within panels, each group of bars of bars is associated to a different condition (either healthy or pathological) and, withih groups, each bar is associated to a different noise level. Bars on the left were obtained with a low noise

level while the ones on the right refer to the higher level of measurement noise. Finally, different colors are used to differentiate strokes correctly identified and classified by the ones misclassified or not found.

PAR Reconstructions

The results obtained with this reconstruction approach, reported in-Figure 2.12(a), were obtained considering ten different reconstructions, each performed with a different electrical and tissue conductivity noise realization. Furthermore, the lower limit for the wandering probe's radius was set to 5 voxels, that corresponds to a spherical anomaly of about 14 cm^3 (33% of the actual target volume). It is important to note that the target differs, both in shape and volume, from the initial guess set for the probe ($V \approx 57cm^3$).

The main characteristic of PAR is the ability to correctly classify all the detected contrasts (i.e. a hemorragic stroke is never mistaken for an ischemic one and vice versa), even though some of the strokes present in the simulated domain are not detected. The false positives rate, that is the number of healthy conditions incorrectly classified as pathological, is the result most deeply affected by the increase of measurement noise, but also the detection performance is degraded with a general decrease of the number of strokes detected with increasing noise.

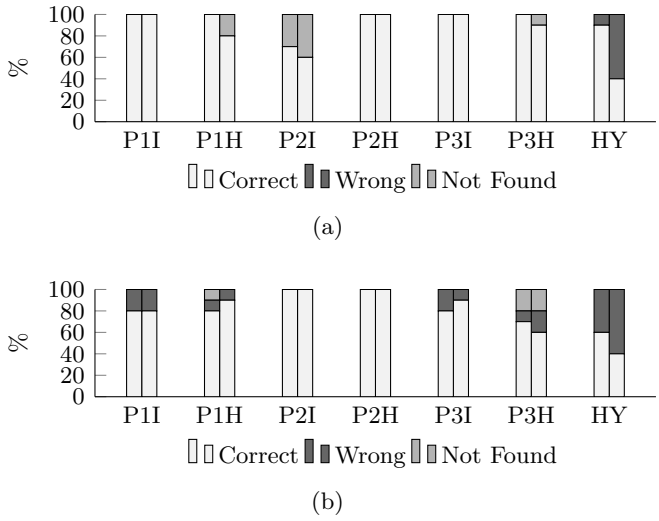

Figure 2.12: Stroke detection and discrimination at low (left column) and high (right column) noise levels for each target and the healthy state. PAR inversion (a) and TR inversion (b).

During the reconstruction, the conductivity variation of the probe

does not change with respect to the initial value because both variations in conductivity and radius of the probe have a similar effect on potentials at the electrodes. If both properties are allowed to vary at the same time, the algorihm tends to become unstable. An error in the initial guess conductivity value of the probe can be compensated by a variation in the volume of the reconstructed region (see Figure 2.13). For example, an ischemic stroke with a conductivity variation that is 30% lower with respect to the background when compared to the literature value, will result in a reconstructed region that has a volume roughly 20% larger than it would have been if it target and probe had the same conductivity. This behavior is conserved in case of an haemorrhagic stroke, the only difference is in the sign of the variation, so that a decrease in target conductivity variation with respect to the background results in a decrease in volume of the reconstructed region. As a consequence, it is possible to obtain correct detection and classification even if the conductivity variation is not precisely known and modeled accurately in the initial guess probe. In extreme cases, such as when very small anomalies with high conductivity variation or large inclusions with electrical properties similar to the background are present, a reasonable guess for the conductivity of the wandering probe is required for reliable detection and discrimination.

TR Reconstructions

For what concerns the TR algorithm, only the conductivities of brain and CSF are reconstructed at each inversion step and the electrical properties of skin, skull and connective tissue are fixed to the correct values. As a consequence, the noise due to inaccurate segmentation is limited to the skin-air and brain-CSF boundaries. This leads to a significanlty lower amount of imprecision in the electrical model of the head when compared to the one used for PAR reconstrucions. The results obtained with this method, presented in Figure 2.12(b), are computed using the same noise realizations used for the previously described PAR results.

In this case, the error rate is higher with, ecluding position P2, at least one noise realization leading to a wrong classification, despite a percentage of correctly classified reconstructions always above 60% and as high as 100% for P2. Imperfect knowledge of the actual electrical model appears to be the driving cause of wrong classifications, as they appear both at the high and low noise levels tested.

The fact that an increase in conductivity is likely to be classified as a decrease and vice versa make the application of classical inversion methods like TR risky when the sign of conductivity variation is

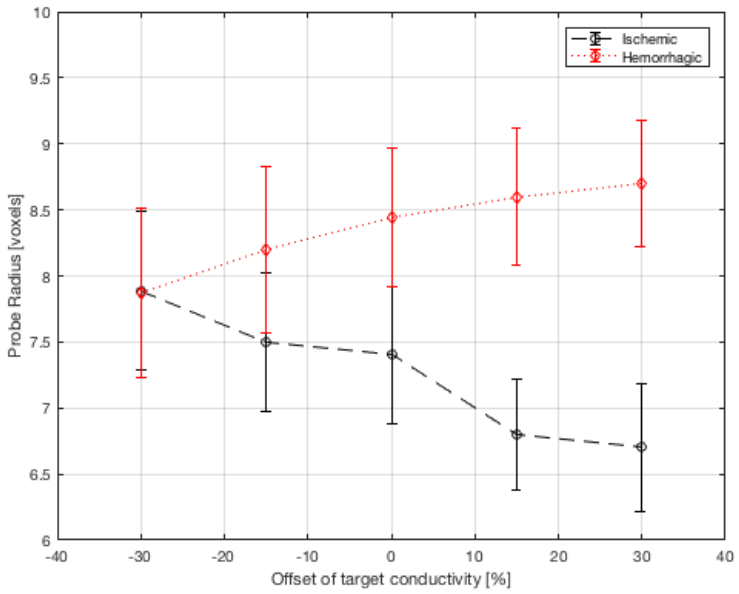

Figure 2.13: If the conductivity of the wandering probe doesn't exactly match the one of the target, the volume of the reconstructed contrast compensates the mismatch. For each condition, dots illustrate the average reconstructed radius and bars are two standard deviations long in total. 10 different noise realization were considered to produce this plot.

critical, such as in stroke detection and discrimination.

2.6.2 Computational Performance

EIT reconstruction methods are characterized by a high computational cost. Each iteration of the TR algorithm requires the computation of $N_e \cdot N_i$ forward problems and solution of Equation 2.4, where $J^T \cdot J + \Gamma^T \cdot \Gamma$ is a matrix with a number of elements of the order of 10^9. PAR, on the other hand, solves $N_i \cdot (2 \cdot N_k + 1)$ forward problems and inverts the matrix $J_p^T \cdot J_p$ (Equation 2.9), at each step. This matrix is significantly smaller than the one considered in TR, indeed it only has about 10 elements. Furthermore, it is worth noting that the number of forward problems solved in PAR at each iteration is independent on the number of electrodes and only depends on the number of different injections N_i and reconstructed properties N_k (5 tissues and 4 spatial parameters that define the position and dimension of the moving anomaly, in the considered application).

A commonly used configuration for stroke detection in 3D, consists of 128 electrodes and 16 different current injections. This corresponds to the solution of 2048 forward problems for TR and 304 for PAR, for every initial guess position and conductivity of the moving anomaly. In the tested configuration, however, the number of forward problems solved by each method at every iteration is comparable but PAR has a speed advantage anyway, due to the smaller Jacobian matrix and the absence of a critical regularization parameter, which would require a specific tuning for each domain and noise level. Another advantage of PAR is that the construction of the Jacobian is very fast and thus it does not impact significanlty on the simulation time, while the implementation of the reciprocity principle, required for the TR reconstruction, is computationally expensive.

The optimization of the regularization parameter, a critical element for the correct reconstruction with the TR method, is obtained through the construction of the L-curve on a point by point basis, a method which results feasible even for large scale problems such as the considered case study of stroke detection and classification. In contrast, generalized singular value decomposition analysis (SVD) is generally prohibitive for large problems. In the L-curve approach, the regularization parameter is computed at a few points and then the one corresponding to maximum curvature is selected [71]. For the current application we have determined that at least 10 points are required to obtain a good L-curve approximation thus preventing the quick and accurate estimation of lambda which is often required in real life applications. Furthermore, the multiple and scarcely characterized sources of noise,

complicate additionally the regularization parameter optimization.

For the system used in this work, whose characteristics are reported in Table 1.2 and considering a segmented head with 27 mm^3 voxels, the solution of each forward problem requires 0.2 s. In TR the implementation of the reciprocity principle for jacobian construction takes about 15 minutes and the inversion step (Equation 2.4) requires about 3 minutes for every iteration. The postprocessing procedure, developed to automatically detect and classify significant conductivity contrasts from the conductivity map obtained with TR, requires about 15 seconds for each inversion process. As for the new approach to reconstruction here introduced, PAR, the inversion step (Equation 2.9) is almost instantaneous, furthermore this method is able to detect and classify an intracerebral stroke in about 3 iterations that correspond to about 24 minutes of computing time. This is just slightly more than the time required by TR for a single iteration (20 minutes), after the optimization of the regularization parameter. For TR, the average number of iterations is 3 and the time required for the optimization of the regularization parameter amounts to about 30 minutes.

It is important to note that, in cases in which the sign of the conductivity variation with respect to the background is known a priori from the specification of the problem, the number of required forward problems solutions in PAR is approximately halved, making it even more convenient. Finally the parametric approach, that avoids a voxel by voxel reconstruction of the domain, is better suited for the inversion of meshes with a large number of elements, especially because the computational cost of the inversion step is independent on the number of discretizing elements.

2.7 Epilepsy Imaging

In this section, epileptic foci localization is evaluated as a potential new application of EIT imaging. In epileptic patients which do not respond to medication and are candidate for surgical treatment, both invasive and noninvasive imaging methods are attempted for epileptic foci localization. When noninvasive approaches fail to provide definitive answers, invasive techniques can be attempted, in which electrodes are surgically placed in contact with the gray matter portion of the brain to greatly increase the SNR and aid localization. The same electrodes are also used to inject small currents in order to generate a map of the eloquent cortex, which should not be resected. EIT reconstructions may be performed with just a slight modification of the current protocol for invasive measurements and its feasibility is analyzed in this

section.

2.7.1 Noninvasive Approach

To identify the epileptogenic focus a combination of structural, functional and clinical information is used. Specifically, a precise representation of the brain structure is obtained through an high-resolution MRI scan, while an EEG recording informs about the electrical activity during a seizure. Since a normal EEG test is generally not able to capture this event, due to its short duration, EEG video telemetry is generally performed. This is a combined video and EEG recording that might last up to a week, and aims to record a seizure in the patient. In this regard sleep deprivation or a reduction in the dose anti-epileptic drug might be used to enhace the probability to record a seizure.

If a focus is identified and it is located far from the so called eloquent cortex, the patient will undergo an fMRI to further evaluate the regions of the brain involved in language processing. This function is significantly lateralized [82] so one of the two emispheres contribute more than the other to its execution, and there are significant differences between different people, thus making it necessary to precisely localize the eloquent regions of the cortex in each different patient.

Unfortunatly in about 15-30% of the patients this approach is unable to identify the epileptic focus due to either discordant data or absence of a structural abnormality. In these cases other functional brain imaging techniques can be used to infer the location of the epileptogenic focus. Specifically, a PET scan may be performed to identify hypometabolism areas, especially in patients that seem to have more than one seizure initiating region. A drawback of this technique is that the potential foci include the entire region involved in the epileptic activity thus leading to uncertainty about the area to resect, even though a less conservative surgery has been associated to a higher probability of leaving the patient seizure free [83].

Another technique commonly applied in this framework is the SPECT, and in particular the ictal SPECT, that analyses how the blood flow within the brain changes before, during and after a seizure. The epileptic focus is generally identified as an hyperperfusion region, surrounded by areas with reduced blood flow. The use of this technique is however limited as it only informs about brain perfusion and an accurate synchronization between the seizure and the recording is required to obtain meaningful images.

Alternatively, EEG source localization techniques can be used to reconstruct a conductivity map of the brain's electrical activity and determine the irritative zones generating seizures. In order to obtain

an accurate result it is necessary to build an electrical model starting from a patient's MRI, as imprecisions in the electromagnetic field propagation model can introduce significant distortions. The use of this technique and the resection of the region with maximal electrical activity has however been associated with a good surgical outcome [84], especially if the region identified through EEG source localization matches the lesion in the patient's MRI [85].

While the brain imaging techniques described above can be used to prevent damage to important regions of the cerebral cortex, it is also necessary to preserve their routes of communication through the white matter. To this end, tractography data extracted from MRI scans can delineate white matter fibers non-invasively.

In approximately 20-30% of epileptic surgery candidates the non-invasive identification of the epileptogenic focus is not possible, thus intracranial EEG is required [86].

2.7.2 Invasive Approach

Two different methods that allow for intracranial measurements are commonly used in clinical practice: electrocorticography (ECoG) and stereoelectroencephalography (SEEG).

ECoG

In ECoG, part of the cerebral cortex is exposed by means of a craniotomy procedure and grids or strips of electrodes are placed in direct contact with the brain tissue to measure the local electrical activity of neurons (Figure 2.14).

This technique allows for a marked increase in the resolution of the reconstructed electrical activity map of the cerebral cortex, which improves from the order of [cm], in the case of a standard EEG source localization performed with scalp electrodes, to [mm] for intracranial measurements. The main disadvantage is the fact that the reconstructed activity is only related to the portion of cerebral tissue which is directly underneath the electrode strips and the localization accuracy for deep epileptic foci is poor. Another important disadvantage is the significant risk of complications due to the craniotomy procedure required to place electrodes.

SEEG

SEEG is a different approach which consists in surgically placing up to 20 very thin, needle-like, electrodes (Figure 2.15) in various strate-

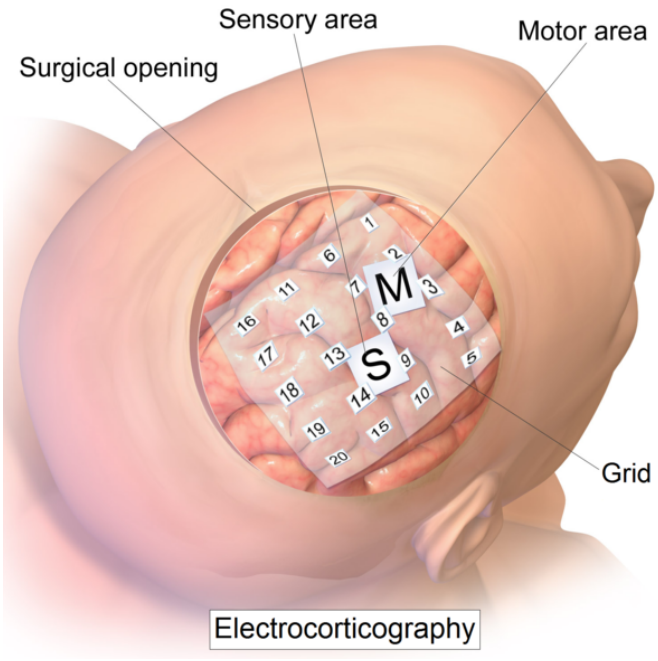

Figure 2.14: ECoG setup [8]

gic locations inside the cerebral tissue determined with the previously described noninvasive brain imaging techniques.

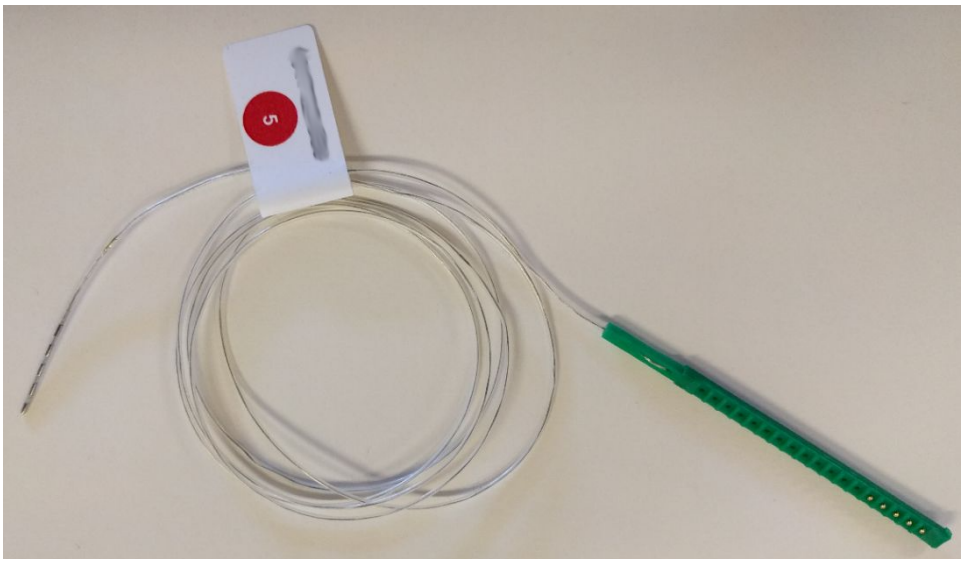

Figure 2.15: SEEG electrode

SEEG electrodes are thin structures which are placed trough burr

holes drilled in the skull, avoiding a more risky craniotomy procedure. Electrodes of different length and with different configurations of contacts (up to 18) separated by insulating material are commercially available (Figure 2.16).

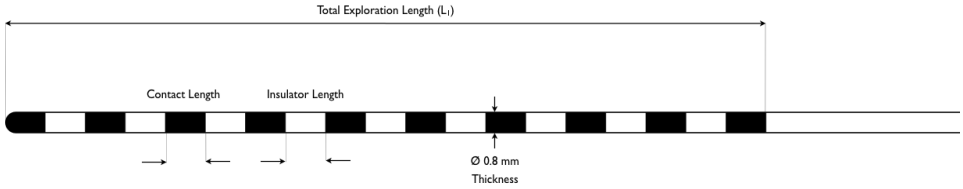

Figure 2.16: SEEG electrode schematic

Electrode positioning is a procedure that requires extensive planning as it can affect the recording quality and can cause damage to the patient (haemorrage, neurological deficit, infection). The identification of the trajectory of each electrode, using multimodal imaging, minimizes the risks by identifying the targets (usually located in the hippocampus, the amygdala the midline or the inferior neocortex), the skull's entry points and by avoiding to puncture blood vessels and other critical structures. Furthermore, careful surgical planning can maximize the contact area between the electrode and the grey matter, thus improving the measurement quality.

Once the electrodes have been positioned, the patient is continuously monitored for up to two weeks, both recording EEG and video images until at least a seizure has been documented. The standard analysis of SEEG data consists in the inspection of the measured potentials by a trained physician which attempts to locate the source of epileptic activity before it spreads to different brain regions (Figure 2.17). The spreading of epileptic activity can also be tracked starting from the measured data.

This work focuses on SEEG due to the higher flexibility granted by the possibility of measuring electrical activity from deep brain regions as well as that of more superficial ones and due to the reduced risk of complications when compared to ECoG procedures.

Recent research shows that cerebral tissue which is experiencing epileptic activity has a significantly different impedance than healthy gray matter and, specifically, impedance is 10% higher in the former case [87]. This is a large enough conductivity contrast which may be detectable by EIT imaging performed with intracranial electrodes. Current injections are commonly performed during SEEG procedures for cortical mapping purposes, in which portions of gray matter tissue are stimulated and temporarily disabled to generate a map of the

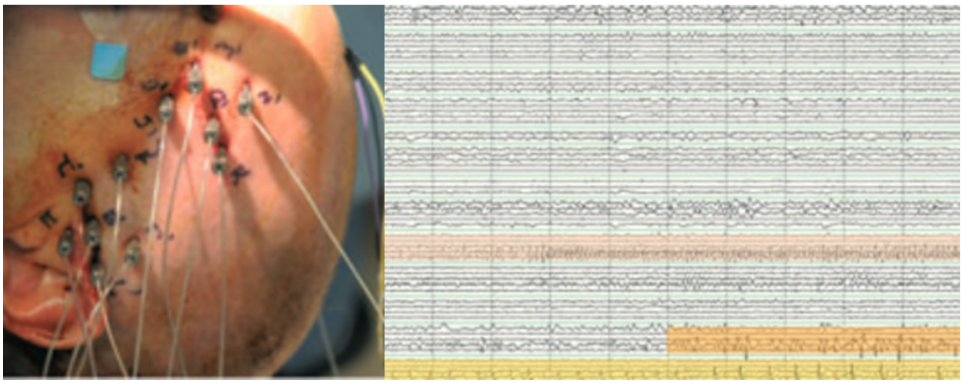

Figure 2.17: SEEG measurements [9]

eloquent cortex, which should not be resected. These current injections could also be exploited to perform EIT measurements and bring a completely new source of information to the arsenal of imaging techniques which have been previously described and are currently used for epileptic foci detection. The aim is thus to bring electrical imaging to the process of electrode foci detection in an attempt to improve the localization accuracy.

In the following, a complete workflow for EIT imaging of epilepsy with SEEG electrodes is presented, starting from the construction of the electrical model. Subsequently, a simulation study is performed to characterize the EIT reconstruction quality in function of the current injection pattern used to acquire data.

2.7.3 Electrical Model

As described the previous sections, the electrical model is constructed starting from MRI scans of the subject. The head volume is segmented in the different head tissues using Brainsuite and electrical properties are assigned to them according to literature data. In the case of SEEG, electrodes are intracranial and their precise location can be inferred starting from the MRI scan by means of a segmentation procedure.

SEEG Electrodes Segmentation

SEEG electrodes are visible on MRI scans but the size of their artefact on MRI images is larger than their actual dimensions Figure 2.18.

In Brainsuite, SEEG electrodes are assigned the label CSF/Other together with part of CSF tissue so an automatic segmentation procedure has been developed to appropriately extract them from the seg-

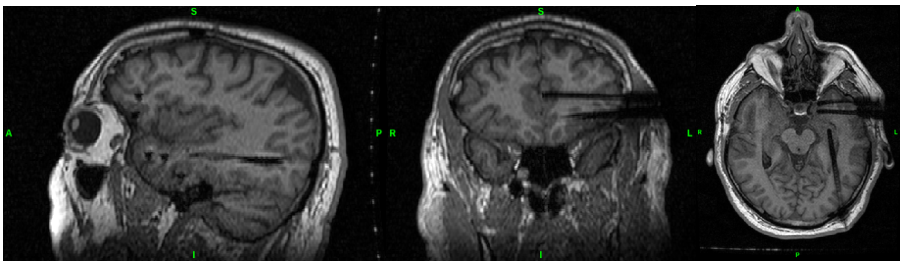

(a) (b) (c)

Figure 2.18: MRI scan of a subject with SEEG electrodes implanted. Sagittal (a), coronal (b) and transverse (c) sections.

mented MRI scan of the subject. Figure 2.19 illustrates the portion of brain tissue to which Brainsuite associates the label CSF/Other.

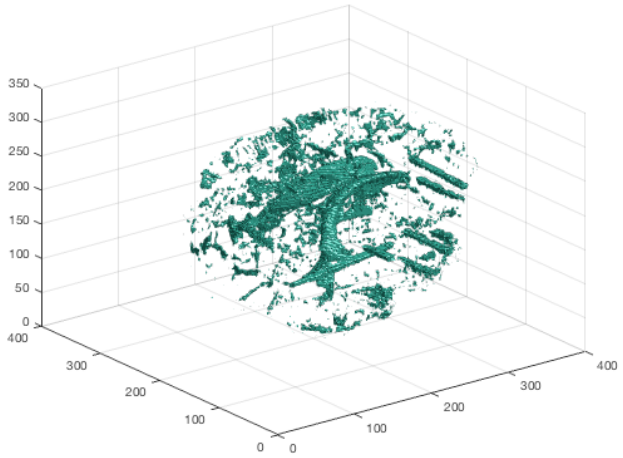

Figure 2.19: The label CSF/Other is assinged by Brainsuite to both areas containing CSF and SEEG electrodes.

Morphological operators (closing) and thresholding based on the volume of contiguous group of voxels can then be applied to the domain to get rid of most of the unwanted CSF and obtain a cleaner volume containing mostly SEEG electrodes. Figure 2.20.

At this point, the only elongated structures present in the domain are SEEG electrodes. Each contiguous group of voxels is considered as a 3D point distribution in space for which a covariance matrix S is computed. The eigenvectors of S indicate the direction of the principal

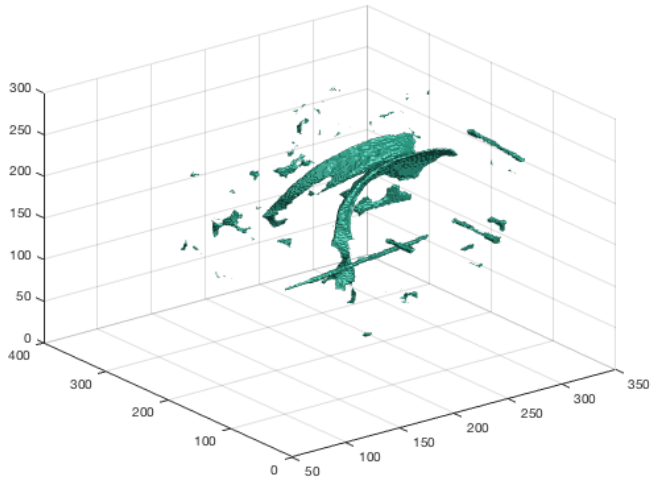

Figure 2.20: Most of the unwanted CSF is removed after morphological operators and thresholding based on volume.

axes while its eigenvalues are related to their length. To filter CSF regions and keep electrodes, only objects with an eigenvalue much larger than the others are selected Figure 2.21.

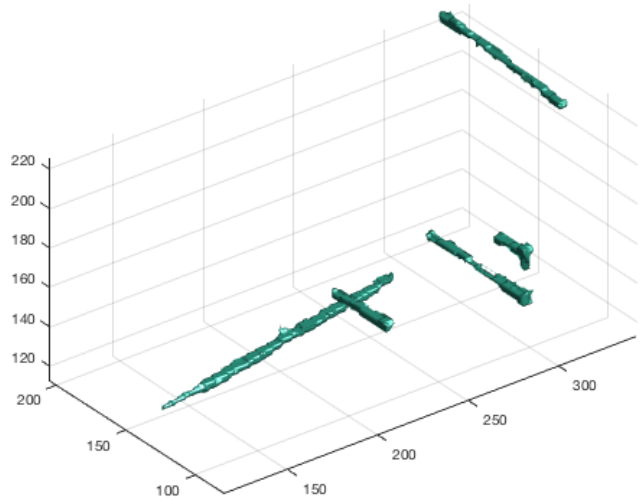

Figure 2.21: Electrodes are selected but their shape is distorted.

The resulting volume is composed of electrodes only but their shape is distorted by the MRI acquisition and morphological operators ap-

plied for segmentation purposes. For this reason, each electrode is scaled back to the correct dimensions according to the datasheet, the surface is smoothed and metallic contacts are placed along the lead at the nominal location (Figure 2.22).

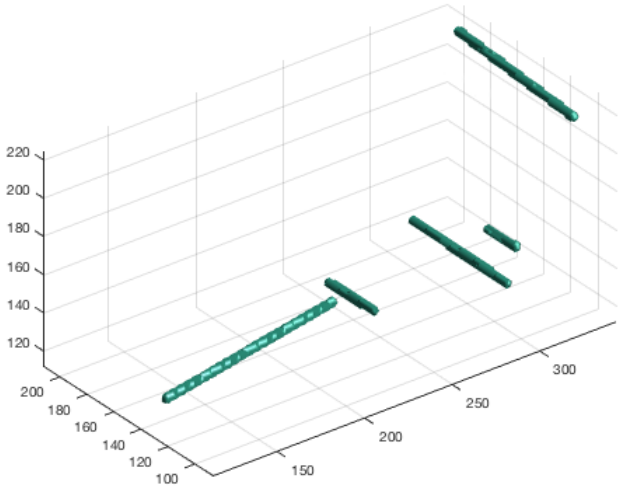

Figure 2.22: Manufacturer specifications are used to scale back the electrodes to the correct dimensions.

The segmented head tissues are then finally combined with the segmented electrodes to generate a complete electrical model for EIT.

2.7.4 Injection Pattern Optimization

The problem of identifying the characteristics of the injection pattern which lead to good sensitivity in the volume of interest has been previously considered in the literature for measurements acquired with surface electrodes and in several different applications. For example, in brain imaging, it is generally known that an opposite injection pattern, in which current is injected and drawn from electrodes that are on opposite sides of the head, allows for a better sensitivity in deep brain regions.

To the best of the author's knowledge EIT imaging with SEEG electrodes has never been described in literature, thus a characterization of the reconstuction quality in function of current injection pattern is needed.

In a standard SEEG protocol, currents are injected between adjacent contacts on the same electrode one electrode at a time to precisely focus stimulation in a limited part of cerebral cortex (Figure 2.23).

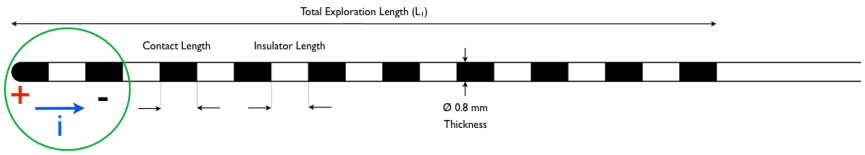

(a)

Figure 2.23: Example of current injection performed for cortical mapping purposes

Two different categories of injection patterns are characterized:

- adjacent, a straigthforward extension of the current cortical mapping stimulation protocol;
- non-adjacent , in which the contact which injects current and the contact which draws current reside on different electrodes.

Simulation setup

For the considered application, time difference reconstructions are possible because a baseline measurements can be performed. A regularized Tikhonov reconstruction algorithm was selected due to the absence of strict time constraints for reconstruction and also due to the highly inhomogeneous background caused by the presence of intracranial electrodes in the domain to be reconstructed. A point by point conductivity map highlighting the conductivity variation associated with the epileptic focus is thus generated.

The domain considered for the analysis is composed of a segmented human head containing 5 different SEEG electrodes for a total of 41 metallic contacts. A simulated epileptic focus of 256 mm^3 volume is then placed in a deep hippocampal cortical region Figure 2.25 (a).

Each of the two different kinds of injection patterns previously described is tested with a varying number of injections (1,2,4,6). As the goal is the localization of the conductivity variation associated with the epileptic focus, the euclidean distance between the maximum reconstructed conductivity decrease and the actual centroid of the simulated epileptic focus is computed for each injection pattern.

After a first analysis in idealized noiseless conditions, the characterization is performed in presence of additive measurement noise. The uncertainty is modeled as a gaussian distribution with mean zero and standard deviation at different levels which correspond to SNR (calculated as the quadratic mean of the simulated measurements referenced

to the average) of about 96, 104 and 106 decibels for the high, medium and low noise levels tested, respectively.

Results

Figure 2.24 illustrates the dependence of reconstruction quality on the number of injections which compose the injection pattern, for both adjacent (a) and non-adjacent (b) injections.

The accuracy of localization for a single injection is very poor and, with distances between the reconstructed and actual position of about 12 [cm] and 6 [cm] for the non-adjacent and adjacent patterns, respectively, the localization can be considered completely wrong. While increasing the number of adjacent injections doesn't improve reconstruction accuracy, when a non-adjacent pattern is considered, while a single injection completely mislocates the target, increasing the number of inter-electrode injections greatly improves the localization performance. In this latter case, the error is reduced to about 2 [cm] with a pattern comprising only 6 different injections and, considering that tens of contacts are generally present, it seems reasonable to expect a further reduction in localization error if more injections are employed.

The information extracted from EIT measurements could then be combined with the outcome of other imaging techniques to increase the confidence in the localization.

Figure 2.25 illustrates an example of the images used to generate the previously described plots. In particular, the case of 6 injections is considered and a 2D slice of the reconstruction crossing the simulated epileptic focus is shown to illustrate the reconstruction quality of both adjacent and non-adjacent patterns.

Even from the raw EIT reconstruction it is evident that switching to a non-adjacent injection pattern markedly improves the quality of the reconstructed image and allows for a better approximation of the epileptic focus despite the intrinsic blurring of TR reconstructions.

To evaluate the requirements of an EIT system for epileptic foci localization, ten different noise realizations are considered to produce the results of Figure 2.26. Inaccuracies in the electrical model of the head are not considered in this comparison because a patient-specific MRI or CT scan is always performed as part of the SEEG procedure, hence very accurate information about electrode and tissue positions is generally available. The graphs, similiarly to the previous ones, illustrate the localization accuracy as a function of the number of current injections which compose the pattern but in this case three different measurement noise levels of increasing magnitude (with SNR from left to right: 106 dB, 104 dB and 96 dB) are considered to better grasp the

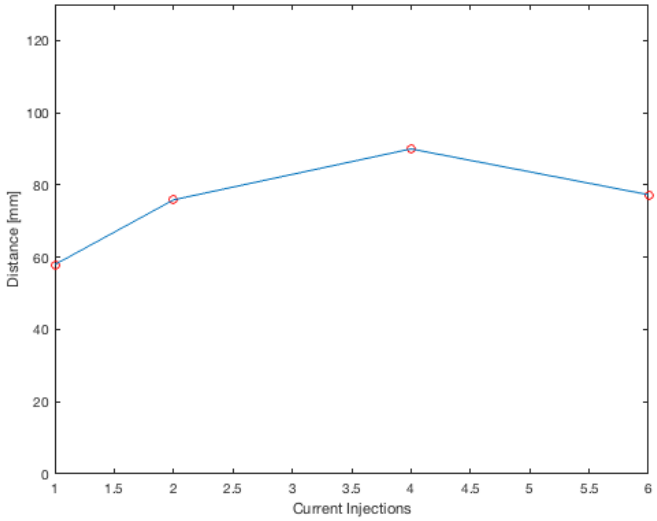

(a)

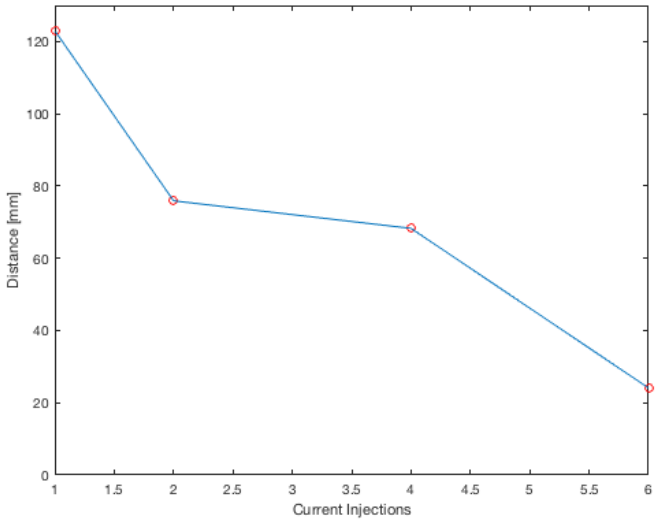

(b)

Figure 2.24: Distance [mm] from peak decrease of reconstructed conductivity variation and actual position of the simulated epileptic focus in function of the number of current injections for a set of adjacent (a) and non-adjacent (b) injections.

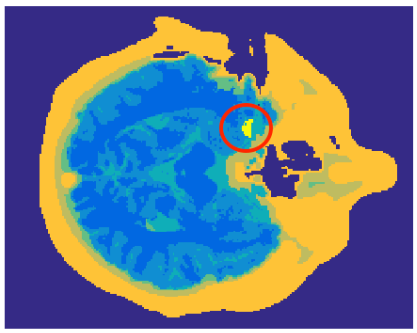

(a)

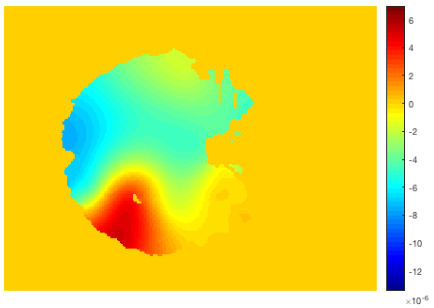

(b)

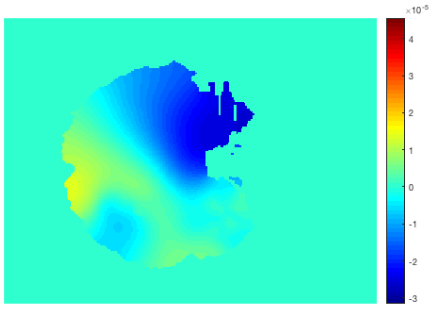

(c)

Figure 2.25: Transverse slice of the head domain crossing the centroid of the simulated epileptic focus (a), reconstruction of conductivity variation with an adjacent injection pattern comprising 6 different injections (b) and reconstruction of conductivity variation with a non-adjacent injection pattern comprising 6 different injections (c). Scale is in [S/m].

effect of noise on reconstruction quality. The same noise realization were used for both injection patterns. The three plots on the top are relative to the adjacent injection pattern while the bottom ones show the performance of the non-adjacent one. Circles illustrate the average of 10 reconstructions while error bars are two standard deviations long in total.

As expected, increasing levels of measurement noise generally decrease the localization accuracy but the trend is similar to the one obtained in the noiseless cases. Localization accuracy strongly degrades for SNRs below 100 dB and this may be considered as a threshold for EIT acquisition systems in the considered application.

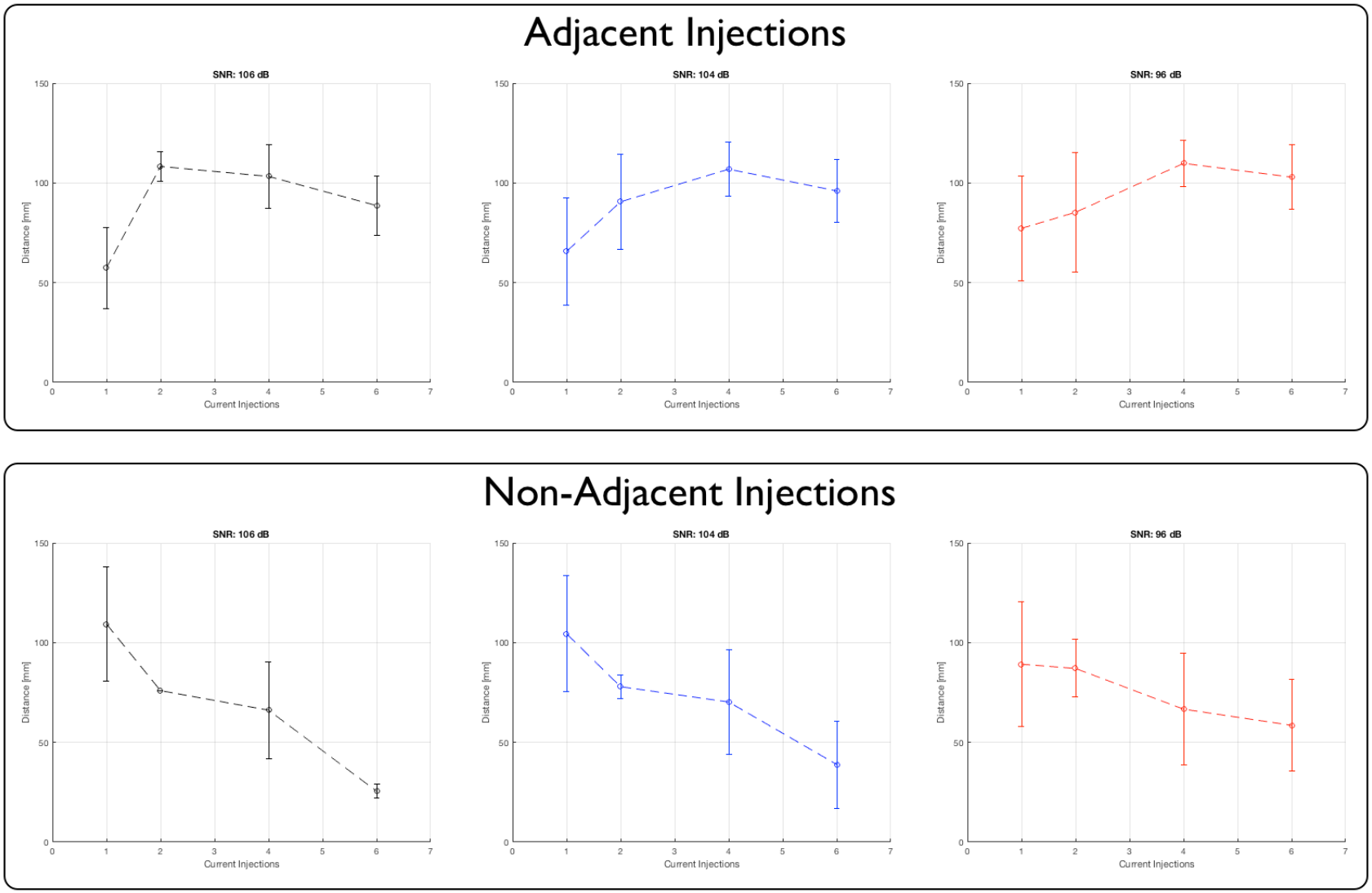

(a)

Figure 2.26: Localization accuracy as a function of number of injections for adjacent (top) and non-adjacent (bottom) injection patterns. Performance significantly degrades below 100 dB.

2.8 Summary

In this chapter the reconstruction of conductivity maps with EIT has been detailed. Specifically, an innovative reconstruction algorithm able to identify compact conductivity contrasts was presented and compared to a widely used method, here used as a benchmark. Two alternative scenarios of different complexity were considered. Initially non-conductive targets in a homogeneous phantom were used to characterize the reconstruction techniques. This comparison allowed to determine the accuracy of the proposed method in a controlled environment, that allowed for an immediate verification of the results. Successively simulated head domains, reproducing both physiological and pathological conditions (hemorrhagic or ischemic stroke) were considered. PAR was determined to be quicker than Tikhonov Regularized inversion at identifying and classifying compact conductivity contrasts in complex 3D domains. Furthermore, the proposed method was shown to be less influenced by measurement noise and uncertainties in the electrical model of the head.

Then, another application of EIT which, to the best of the author's knowledge has never been described in literature, was introduced. It exploits needle like electrodes, surgically implanted within the brain of epileptic patients, to reconstruct the brain's conductivity map in order to help locate the epileptic focus. Within this topic a segmentation algorithm able to automatically identify intracranial electrodes from a MRI scan of the head was presented, together with an analysis of reconstruction quality as a function of current injection pattern, to determine an optimized protocol that would improve the quality of the reconstruction.

Chapter 3

EEG Source Localization

The brain imaging technique detailed in this chapter is EEG source localization, which is based on EEG recordings and aims to reconstruct a map of brain activity. sLORETA, one of the most commonly used algorithms for EEG source localization, is described together with its parallel implementation using the CUDA framework, which is used to optimize the most computationally expensive steps of this method. The newly developed sLORETA implementation is then compared to its serial counterpart and experimentally validated using data recorded during Event Related Potentials (ERP) experiments, which evaluate the brain's response to specific events. In the analysis, visual stimuli are used and the objective is the identification of the source of specific peaks in the recorded signal that are characterized by a defined latency time and a direction of deflection.

3.1 Background

The correct functionality of the human brain relies on the activity of distributed neural networks [88]. These networks are created by the coordinate activity of a large number of neurons which heavily interact, through inhibitory and excitatory feedforward and feedback processes to give rise to complex functions [89]. The localization and the determination of the distribution of the various modules of the functional network implicated in a given mental task is the principal aim of functional neuroimaging studies.

The electric potentials that is possible to measure on the scalp by means of an electroencephalographic (EEG) acquisition system are due to the impressed current density distribution that is generated by neuronal post synaptic activity in the cerebral cortex. By exploiting measured electric potentials on the scalp, it is possible to generate a map

of the electrical activity in the brain by solving the inverse problem.

Unlike images generated by functional magnetic resonance (fMRI), which measure cardiovascular coupling to brain activity and thus represent an indirect index of brain activation, the estimation of the current density distribution provides a direct approximation of electrical activity.

The simple approach of locating the electrode that exhibits the maximum signal and considering the underlying brain region as the source is misleading because a large number of different configurations of the generators can produce the potential distribution measured on the scalp [90].

To reconstruct a meaningful volumetric map of electrical activity, it is necessary to solve an inverse problem that consists in the determination, from a set of measurements, of the causal factors that produced them. In EEG source localization, the inverse problem aims to identify the current density distribution in the gray matter region of the brain that leads to the electric potentials measured on the scalp. This is subordinate to the definition of an electrical model of the head, which can be initially constructed as previously described in the EIT section. In this case, electrodes are placed on the scalp according to the positions defined by standard EEG caps.

3.2 Tuning the Electrical Model

Starting from an electrical model of the head constructed as detailed in the EIT chapter, it is possible to use part of the PAR algorithm to optimize the electrical properties of the different tissues which compose the human head on the specific subject which is to undergo EEG source localization. To this end, a framework for the integration of EIT measurements into source reconstruction algorithms has been developed (Figure 3.1).

As previously described, an MRI scan of the subject or a head volume coming from an online database is segmented using one of the available open source tools such as BrainSuite to obtain the location of the different head tissues. Then, to each tissue is assigned an impedance value according to the literature. In the proposed approach, the electrical properties are then fitted to the specific subject by means of EIT measurements which are performed prior to EEG source localization. In PAR, if no initial guess wandering probe is inserted in the domain, only the conductivity values of background tissues as whole regions are reconstructed and this information can be exploited to update the electrical model of the head to be used for EEG source

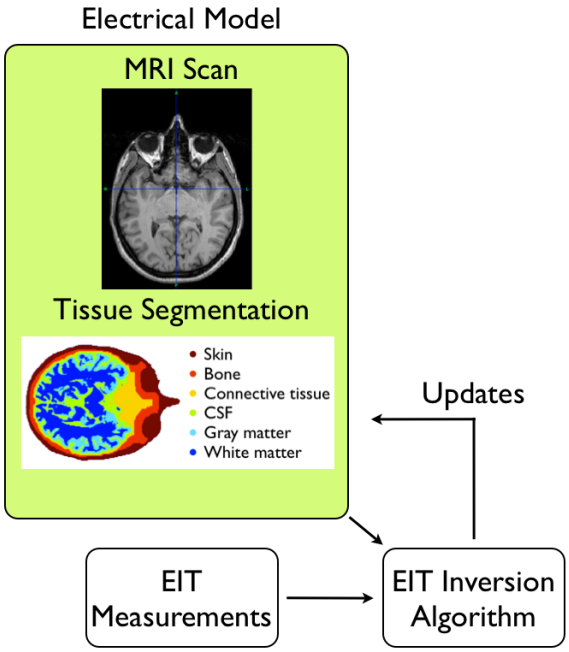

Figure 3.1: EIT measurements can be used to fit the electrical properties of the various head tissues to the specific subject and obtain a more realistic electrical model of the head.

localization purposes.

3.3 Forward Problem

The forward problem consists in the determination of the potentials measured on the scalp generated by the combination of the current densities present in each voxel of the discretized gray matter region of the brain (Equation 3.1).

$$\Phi = KJ + c_1 \tag{3.1}$$

Where Φ is a vector containing the electric potentials measured on the scalp, J is a matrix containing the current density in each voxel of the domain and c_1 is an arbitrary constant. K is the so called lead field matrix, that describes how the current generated by each dipole contributes to the measured potential and depends on the number and positioning of the sensors on the scalp, on the voxels disposition and the electrical model.

3.4 Inverse Problem

The inverse problem in EEG source reconstruction is underdetermined, with the number of unknowns that need to be resolved usually at least about three orders of magnitude higher than the amount of measured data. For this reason, to obtain a single solution, a-priori assumptions on the generation of the signals are introduced. The quality of the reconstructed image is tightly connected to these assumptions and thus care must be taken in ensuring their accuracy and appropriateness.

In the present case Φ and K are known and the aim is to determine J. This can be formalized, in case of exact noise free measurements, as in Equation 3.2 where T is a generalized inverse of K and satisfies Equation 3.3.

$$\hat{J} = T\Phi \tag{3.2}$$

$$KT = H_N \tag{3.3}$$

Where H_N stands for the $N \times N$ average reference operator (Equation 3.4):

$$H_N = I_N - \frac{1}{N} 1_N 1_N^T \tag{3.4}$$

where I_N is the $N \times N$ identity matrix and 1_N is a vector (of length N) composed of ones.

The condition in Equation 3.3 imposes the correspondence between the potentials measured on the scalp and those obtained applying Equation 3.1 to the estimated current density obtained through Equation 3.2. Since the inverse problem is underdetermined, there are infinite $\hat{J}$ that satisfy Equation 3.2, it is thus necessary to identify a criteria to select one solution. The resolution matrix describes the relation between the estimate current density $\hat{J}$ and the real one (Equation 3.5).

$$R = TK \tag{3.5}$$

The properties of an inverse solution can be characterized fully through the corresponding resolution matrix, and specifically through either its columns, or its rows. Each column represents the estimated current density due to one current source, this is also known as the point spread function as it describes the effect of each generator on the measured potentials. Any inverse solution can be completely characterized through the study of all possible point spread functions and particularly the evaluation of its ability of correctly localize ideal point sources.

Each row of R corresponds to an averaging kernel of Backus and Gilbert, that is a description of how all the sources contribute to the

generation of the current density in a specific point. However it can be shown, for the EEG problem in a piecewise homogeneous medium, that the averaging kernel always reach their maximum on the border of the domain. This is because the averaging kernels are, in this case, combinations of harmonic functions, and thus harmonic functions themselves and it has been demonstrated [91] that harmonic functions attain their extreme values on the boundaries of their domain. The non-existence of ideal averaging kernels for non boundary points limits the number of algorithm able to correctly localize the sources of EEG signal.

3.4.1 LORETA

One of the classical approaches for the identification of the generators of the surface potential is the LORETA (LOw REsolution electromagneTic tomograAphy) algorithm, that consists in the constrained solution of the forward equation (Equation 3.1). The functional that needs to be minimized is:

$$F = \|\Phi - KJ\|^2 + \alpha\|J\|^2 \tag{3.6}$$

where α is a regularization parameter.

The explicit solution to the minimization problem is:

$$\hat{J} = T\Phi \quad with \quad T = K^T H[HKK^T H + \alpha H]^+ \tag{3.7}$$

where $[HKK^T H + \alpha H]^+$ denotes the Moore-Penrose pseudoinverse of $HKK^T H + \alpha H$ and H is the average reference operator of Eq. 3.4. This method proved to have fairly good localization error, generally smaller than one grid unit, even for deep test sources [92], [93], [94].

3.4.2 sLORETA

A variant of the LORETA algorithm, sLORETA, introducing a standardization step improves the localization performance with respect to LORETA. It is proven to provide zero localization error in noiseless conditions and for this reason it has become one of the most widely used EEG source localization algorithms in practice.

Even in this case solving the inverse problem consists in minimizing the functional of Equation 3.6 and the explicit solution is the one of Equation 3.7 but, in this case, this first estimate is standardized. In order to perform the standardization step, it is necessary to obtain an estimate of the variance of $\hat{J}$. The actual source variance (S_J) can be described with the identity matrix, while the variance due to noisy measurements, that is assumed to be uncorrelated to the activity of

the actual sources, can be formalized as:

$$S_{\Phi}^{noise} = \alpha H \tag{3.8}$$

Thus the electric potential variance becomes:

$$S_{\Phi} = K S_J K^T + S_{\Phi}^{noise} = K K^T + \alpha H \tag{3.9}$$

Combining Equation 3.9 and Equation 3.7 it is possible to define the variance of the estimate current density as:

$$S_{\hat{J}} = T S_{\Phi} T^T = T(K K^T + \alpha H) T^T = K^T [K K^T + \alpha H]^+ K \tag{3.10}$$

This estimate is used to standardize $\hat{J}$ with respect to each voxel, as shown in Equation 3.11.

$$\hat{J}_l = \hat{J}_l^T ([S_{\hat{J}}]_{ll})^{-1} \hat{J}_l \quad for \quad l = 1...n_{voxel} \tag{3.11}$$

3.5 Parallel Implementation

One of the most computationally expensive steps of the presented reconstruction methods is the lead field computation, which needs to be performed whenever there is a change in the electrical model that specifies the positions and electrical properties of the different tissues that compose the head. Other very demanding steps which are also perfomed at each inversion step are the matrix product of Equation 3.7 and the standardization step of Equation 3.11.

In this thesis, the developed parallel code is written C and exploits the OpenMP library to split work among CPU computing threads and the CUDA framework to take advantage of the GPUs as accelerators. Code is compiled into a shared library which can be loaded by a Matlab mex file for easy Matlab integration of the parallel implementation.

In the following, details about the parallel implementation of the lead field computation, the LORETA matrix product and the sLORETA additional standardization step are provided.

3.5.1 Lead Field

The most straightforward way to compute the lead field matrix is by using the perturbative approach. This method consists in varying the impressed current in each voxel of the region of interest by a fixed amount and subsequently recording the effect on the measured surface potentials. To this end, it is necessary to solve a number of forward

problems which compute the voltage distribution in the volume of interest given a certain disposition of electrical current sources (i.e. voltage potentials on the electrodes generated by dipole current sources in the grey matter region of the brain).

The forward problem solver used in this work is based on the finite volume method and is tuned for heterogeneous multi-CPU and multi-GPU computing systems [95].

The perturbative approach has the disadvantage of being computationally very expensive. In fact, it requires at least N_v+1 forward problem solutions, where N_v is the number of gray matter voxels. On the considered computing system described in Table 1.2, with a domain discretized with $1mm^3$ voxels, each forward problem solution takes about 4 seconds and the computation of the full-resolution lead field matrix by the perturbative approach would take about 32 days.

To speed up the computation, the lead field matrix is computed by exploiting the reciprocity principle [73]. The reciprocity principle states that, considering a region Ω with conductivity σ, given a current source and a voltage detector in a medium with electrical properties which are generally verified in nature (and in our case as well), the voltage measured by the detector is the same that it would measure if current source and voltage detector were switched. The idea is then to sequentially place a fixed test current source at each electrode position and compute the lead field matrix as the gradient of the voltage computed by the forward problem solver in each voxel of the domain along the three cartesian directions. The reciprocity principle allows to drastically reduce the number of forward problem solutions that are needed to compute the lead field matrix to N_m, where N_m is the number of measuring electrodes, and thus to shorten the computing time from about 32 days to about 10 minutes.

3.5.2 sLORETA

A parallel implementation of the inversion step in the time domain has been developed. In particular, the product between the T and the ϕ matrices of equation 3.2 was implemented to run on GPGPU capable Nvidia GPUs using the parallel CUDA programming language. The implementation is integrated with the Matlab environment by means of a mex file that loads a shared library. The optimized CUDA implementation of LORETA takes advantage of the device shared memory to reduce as much as possible the latency of memory accesses in the matrix product. As illustrated in Figure 1.13, threads can access data from both per-application-context global memory and per-block shared memory. Since the bandwidth of shared memory is much higher, and

its latency is much lower, than global memory, data that needs to be processed by blocks of threads is moved to shared memory before processing. sLORETA can be considered an extension of the LORETA algorithm in which an additional step, the standardization, is performed.

The standardization step is implemented using the OpenMP API for paralled programming to make efficient use of the available threads of a multicore computing system.

3.5.3 Performance Comparison

The characterization focuses on the sLORETA algorithm which is more commonly employed due to the better localization accuracy. The performance of the parallel implementation is compared with a standard Matlab implementation of the algorithm. In the first comparison, the gray matter region of the brain is discretized with about $7 \cdot 10^5$ cubic voxels. In Figure 3.2, voltages are measured with 32 electrodes and the time to reconstruction for several different sampling rates is illustrated. Considering 128 samples per second, the parallel implementation provides a reconstruction in about 3 seconds of computing time while a standard Matlab implementation requires more than 20 seconds. It is important to note that the Matlab integration (shared library loaded by a mex file) limits the level of optimization of the CUDA code that runs on GPUs and a standalone implementation would reduce the time to reconstruction for a sampling rate of 128 Hz to less than a second, thus rendering the source localization process real time.

In Figure 3.3, 128 electrodes are used to measure voltages on the scalp. In this case, while the time to solution doesn't significantly vary for the Matlab implementation, the parallel implementation requires significantly more time than before to elaborate 128 and 256 time samples. The cause is the overhead due to the Matlab integration and the larger data transfers that need to be performed between the GPUs and the Matlab environment. As the number of samples increases, the effect of the number of electrodes becomes less noticeable.

In the following, gray matter is downsampled to about $9 \cdot 10^4$ voxels. Given the fact that the inverse problem is underdetermined, it is possible to reduce the number of sources considered without seriously affecting the quality of the source localization.

It is important to note that this is not the same thing as reducing the resolution of the electrical model used by the forward problem solver to generate the lead field matrix, which needs to be as precise as possible to accurately represent the physics of the problem.

In Figure 3.4, 32 measuring electrodes are considered and the reconstruction is performed on the subsampled gray matter region of

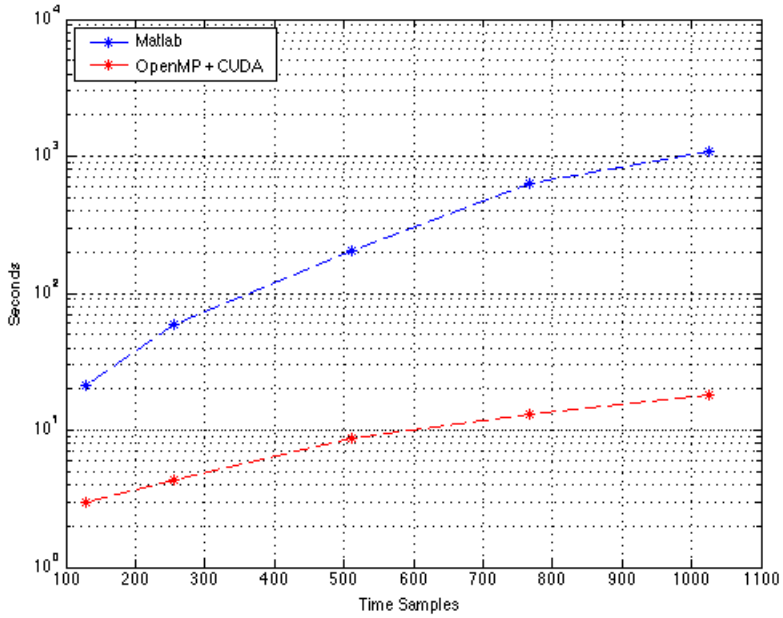

Figure 3.2: Time to solution [s] in function of time samples for about $7 \cdot 10^5$ sources and 32 measuring electrodes. Y axis is in logarithmic scale.

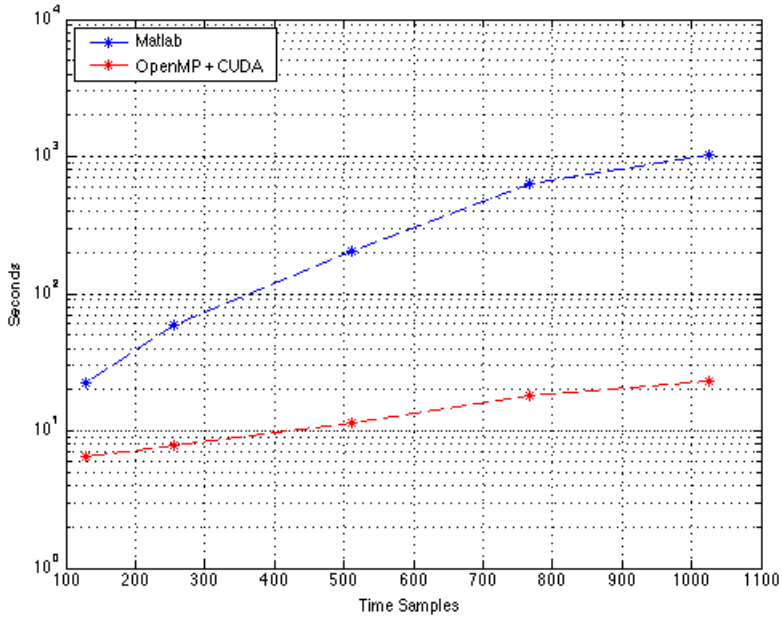

Figure 3.3: Time to solution [s] in function of time samples for about $7 \cdot 10^5$ sources and 128 measuring electrodes. Y axis is in logarithmic scale.

the brain. In this case, both implementations are able to provide a source localization in significantly less time than with a full resolution discretization of the gray matter region. It must be noted that the Matlab implementation still requires more than three seconds of computing time for a sampling rate of 128 Hz while the parallel implementation can reconstruct more than 1024 samples in the same amount of time.

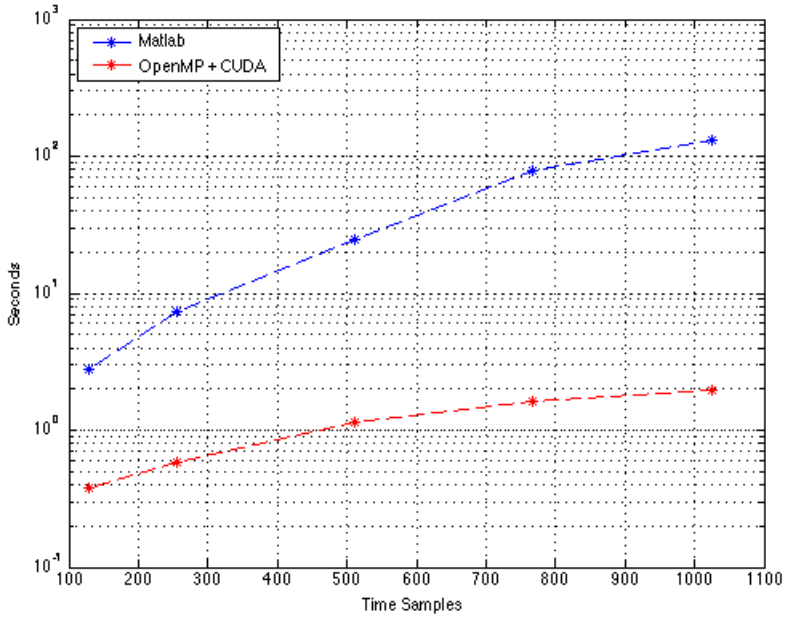

Figure 3.4: Time to solution [s] in function of time samples for about $9 \cdot 10^4$ sources and 32 measuring electrodes. Y axis is in logarithmic scale.

In Figure 3.5, 128 electrodes measure voltages and the subsampled gray matter region of the brain is considered. In this case, despite the Matlab integration, the parallel implementation is able to reconstruct in real time data acquired with a sampling rate of 128 Hz.

3.6 Experimental Validation

The developed implementation is tested with data coming from a particular Event Related Potentials (ERP) experiment in which visual stimuli are used. The aim is to image Visual Evoked Potentials (VEP).

In a VEP experiment, subjects concentrate on a visual stimulus which, in our case, consists in a flashing checkerboard. EEG is recorded during the administration of a set of visual stimuli in which the stimulus is repeated several times. Each EEG recording corresponding to

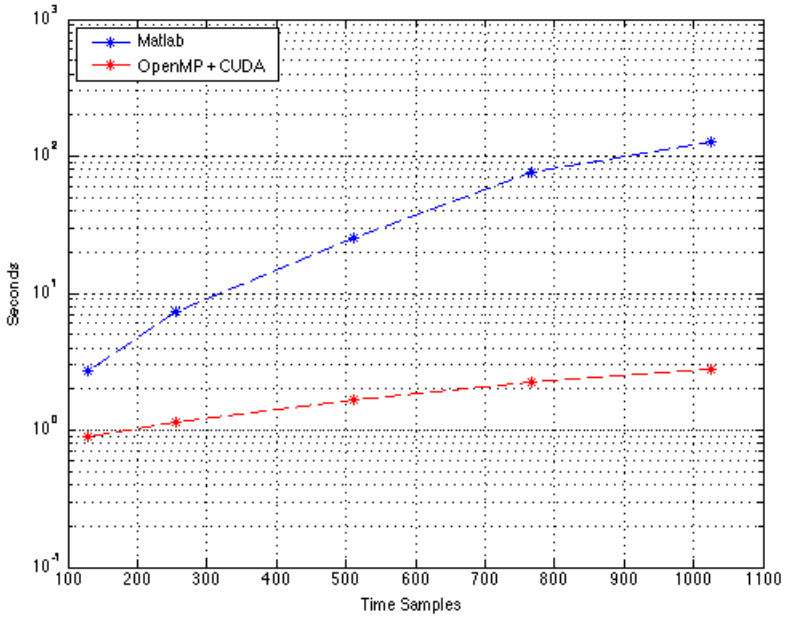

Figure 3.5: Time to solution [s] in function of time samples for about $9 \cdot 10^4$ sources and 128 measuring electrodes. Y axis is in logarithmic scale.

the administration of a visual stimulus is called epoch. The various measured epochs are then averaged to allow the VEP signal to emerge from noise and uncorrelated electrical activity of the brain. The process was repeated for 7 different subjects and then all the epochs were aligned and averaged to obtain a single grand average Figure 3.6.

The sLORETA algorithm was then used to reconstruct a map of electrical activity corresponding to the P100 peak reponse and the result is illustrated in Figure 3.7. It is possible to relate the precise location of maximal activation to a standard neuroanatomical region by overlaying to the reconstructed conductivity map a parcellated cortical surface generated with Brainsuite according to neuroanatomical atlases (Figure 3.8). The obtained reconstruction highlights a peak activation in the left occipital cortex which is consistent with the administered right field visual stimulus and replicates similar findings obtained by other groups with fMRI techniques [96].

In addition, the level of cerebral activation in each neuroanatomical region can also be exploited to perform functional connectivity studies which provide an estimation of information sharing between different cortical areas.

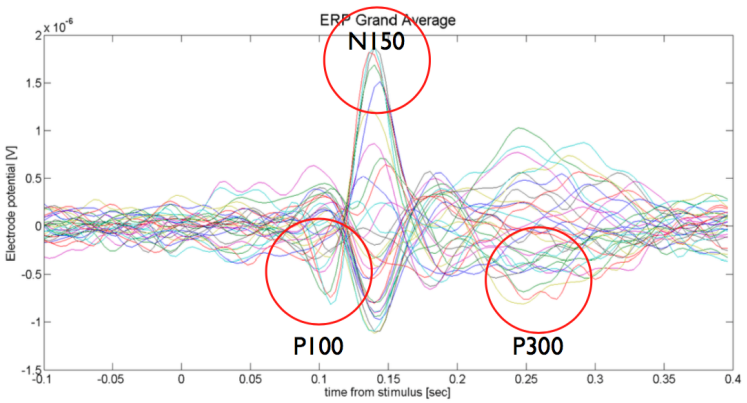

Figure 3.6: Grand average of the VEP recordings highlighting the characteristic peaks (P100, N150 and P300).

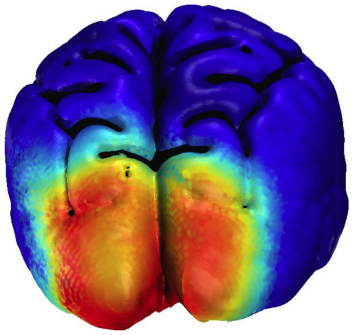

Figure 3.7: Cortex activation corresponding to the P100 visual evoked potential. Right visual field stimulus. The maximal activation is located in the controlateral occipital region.

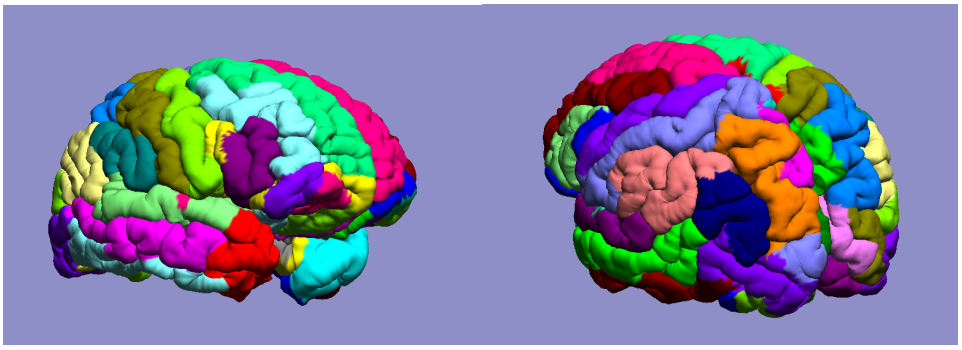

(a) (b)

Figure 3.8: Parcellated cerebral cortex

3.7 Summary

In this chapter a parallel implementation of sLORETA was presented. This algorithm is one of the most widely used to localize the sources of brain activity from EEG data and the parallelization of its most computationally expensive steps was demonstrated to significantly improve the overall performance. Indeed, it was demonstrated that in a subsampled domain, a sampling rate of 128 Hz was associated to a reconstruction time of less than 1 s and thus to the possibility of elaborating the data in real time. The implementation was validated with experimental VEP data. The P100 peak, one of the three main peaks emerging from the considered experiment, was localized with the implemented algorithm and the outcome proved to be consistent with literature results obtained with fMRI experiments.

Chapter 4

Discussion and Conclusions

In the this work three different applications of electrical brain imaging have been presented. These approaches retrieve both structural and functional information about the brain and can be used as diagnostic or research tools.

4.1 Electrical Impedance Tomography (EIT)

The first two applications are based on EIT measurements. EIT allows to reconstruct the conductivity map of the brain using small electrical currents injected, usually through the scalp, according to predefined patterns. Since different biological tissues have different conductivities, this information may be used to obtain a structural representation of the subject's brain and diagnose different pathologies, including stroke and epileptic foci, which have been considered in this work as case studies. A novel algorithm for the detection of compact conductivity contrasts on an approximately uniform background, PAR, is presented.

4.1.1 Stroke Detection and Classification

A stroke can be defined as the loss of cerebral function due to an interruption of the blood flow to the affected region.

Normally a CT or MRI scan is performed for diagnosis, however these techniques are only available in major medical centres. This significantly limits the use of tPA, a clot-busting therapeutic agent, which can be used to limit the brain damage in patients with an ischemic stroke but must be administered within 4.5 hours from the stroke onset. Another fundamental requirement of stroke diagnosis is the correct classification as hemorrhagic or ischemic, as the use of tPA in patients with hemorrhagic stroke can be dangerous.

EIT may be used to address these limitations, being able both to detect a stroke sooner than CT or MRI and to distinguish between the two major types of stroke as they cause an opposite change in the conductivity of the interested region. EIT also has the significant advantage of requiring only low cost, portable instrumentation.

One of the most widely used algorithms to reconstruct images from measured EIT data is the Tikhonov Regularized inversion (TR inversion), which reconstructs the conductivity associated to each voxel of the domain by solving the inverse problem. In this case, the solution is determined by minimizing a functional that represents the error between the voltage recorded on the scalp and the simulated voltages generated using the estimated conductivity distribution.

This procedure, however, is computationally expensive and requires the tuning of a regularization parameter. This parameter is part of an additional term of the error function that can be used to include prior information. In the case of stroke detection, the regularization term is selected to favour the reconstruction of compact conductivity contrasts, in an attempt to reduce the ill-posedness of the problem and allow for an unique solution of the inversion step. The determination of an optimized regularization parameter is critical as a non-accurately tuned parameter generally leads to incorrect reconstructions. The computational cost precludes the application of TR to stroke detection due to the tight time frame in which it is possible to administer tPA.

To address these limitations, a new algorithm for EIT reconstruction which can be used to efficiently detect a number compact conductivity contrasts and classify them either as an increase or decrease of conductivity with respect to the background, PAR, is described in Chapter 2. Unlike TR, PAR does not require the estimation of a regularization parameter and, by avoiding to reconstruct the conductivity of each voxel belonging to the discretized domain, results significantly faster.

To evaluate the preformance of the proposed algorithm, its results are compared to the ones of the TR algorithm which is combined with a post-processing procedure that allows the automatic detection and classification of compact conductivity contrasts. The algorithms are compared both with experimental measurements acquired on a cylindrical phantom containing different conductivity contrasts and with simulated measurements generated with a 3D head domain. The phantom is realized by placing 16 equispaced electrodes on the border of a tank filled with saline solution and using nonconductive targets as conductivity contrasts.

For the considered applications, PAR proves to be quicker and more

robust than TR, which is largely employed in the field of EIT, especially when the reconstruction makes use of complex 3D electrical models and the data are affected by significant discretization and measurement noises. Furthermore, PAR has been shown to be able to compensate for errors in the shape and electrical properties of the target, improving the algorithm usability in real situations, where the characteristics of the target are generally unknown.

Other regularization methods, like the sparsity regularization ones, may provide an higher spatial resolution and thus a higher localization accuracy than PAR, but these characteristics are beyond the presented algorithm's scope, since the goal is just quick detection and classification of compact conductivity variations with respect to the background and not precise estimation of the contrast location. Furthermore, like TR, sparsity techniques are computationally very expensive both in terms of memory and time, since they implement the most classic approach to EIT reconstruction: determination of the conductivity map of the entire domain on a voxel by voxel basis.

As the background and target regions are reconstructed on a voxel by voxel basis in TR and other classic inversion approaches, the quality of the resulting reconstruction relies on the precise knowledge of the domain in terms of electrical properties and boundaries of the different materials/tissues that compose it. In practical applications this information is generally only approximately known and PAR, separating the reconstruction of the conductivity contrast from that of the background, generally performs better than standard inversion methods, leading to a reliable recognition of the target over a wide range of conditions.

A notable exception might be inclusions over high contrast and distributed inhomogeneous backgrounds (e.g. stripy or grid like) in which PAR might perform poorly due to the numerous spurious local minima. If such a domain is present and enough prior information about the structure of the background region is available a priori, subdomain techniques coupled with more standard voxel by voxel inversion approaches might provide more accurate results at the expense of high computational cost.

The results presented in Chapter 2 demonstrate how PAR is a promising alternative for the quick detection and characterization of compact conductivity variations, due to the reduced computational burden and the absence of a regularization parameter. While the theoretical convergence of the presented method in all cases hasn't been demonstrated, the proposed algorithm proved to be robust with respect to several sources of uncertainty and to perform generally better than

TR, the standard approach to EIT reconstruction.

4.1.2 Epileptic Foci Localization

Then, a new application of EIT imaging is explored: localization of epileptic foci with measurements acquired using SEEG electrodes. SEEG is an invasive technique which records the activity of specific areas of the brain using needle-like electrodes to locate the seizure initiating region in patients affected by pharmacoresistant focal epilepsy. While non-invasive imaging techniques, like EEG, MRI, PET and SPECT can successfully identify the region to resect in a majority of cases, sometimes their results are not conclusive and SEEG is used to directly monitor the activity of the regions that are suspected to contain the epileptic focus.

In clinical practice, the recorded raw signal is visually analysed to identify the region in which the anomalous activity originated. In this work the aim is to bring imaging techniques to the process of localization of epileptic foci. As electrical stimulation is routinely performed during SEEG recordings to help locate the eloquent regions of the brain, and recent reseach higlights the presence of a conductivity contrast generated by epileptic cortex, EIT reconstructions can be attempted. The application of methods developed for EIT image reconstruction to SEEG data is indeed completely novel and has the potential to significantly improve the localization accuracy of the epileptic focus.

A simulation study is performed to characterize the reconstruction quality in function of the current injection pattern. The electrical model is constructed starting from a MRI scan of the head of the subject as described in the previous sections. In addition, electrodes are automatically detected with a custom segmentation procedure and contacts are placed on the leads according to the manufacturer's specifications. Then, time difference reconstructions are performed using the Tikhonov regularized inversion method (TR) on simulated SEEG data.

The comparison between different kinds of electrical stimulation patterns, the adjacent one in which stimulating contacts are next to each other and reside on the same electrode lead, and the non-adjacent one in which stimulating contacts reside on different electrode leads, highlights the importance of injection pattern optimization for EIT with SEEG electrodes.

Specifically, increasing the number of injections and performing them between contacts of different electrodes markedly improves the reconstruction quality, suggesting that a completely new source of information for epileptic foci localization could be exploited with just a

slight modification of the SEEG acquisition protocol currently used in clinical practice.

4.2 EEG Source Localization

Finally, EEG source localization has been considered. This technique measures the electrical potentials on the scalp, thus providing a direct quantification of the neural activity rather than an indirect estimation through changes in regional blood flow. While the measured signals are generally considered for diagnostic purposes, in this work they are exploited to localize the source of neuronal activity. This is one of main goals of functional neuroimaging studies, that evaluate which regions of the brain are involved in specific functional tasks and how they are distributed. These results can inform both on the normal and pathological brain activity and might help identify which treatment would be the most beneficial in a number of conditions (e.g. epilepsy, schizophrenia, depression, Alzheimer's disease).

The localization of the EEG sources requires the solution of the inverse problem, that is the determination of the causal factors that give rise to a specific set of observations. Since the number of measurements (voltage at the electrodes) is significantly lower than the number of unknowns (the current density in each voxel of the domain), this problem is underdermined and in most cases, ill-posed. These characteristics make source localization a very difficult problem, both mathematically and computationally.

One of the algorithms that are most employed in this field is sLORETA which provides zero localization error in noiseless conditions. It consists in minimizing a functional that represents the error between the measured potentials and the ones estimated starting from the reconstructed current density distribution within the brain. While granting an accurate reconstruction and being widely used in practice, some of the steps of this algorithm are computationally expensive. Specifically, the computation of the lead field matrix, the LORETA matrix product (Equation 3.7) and the normalization of the matrix containing the current densities in each voxel of the domain (Equation 3.11) have been identified as the operations requiring the most resources.

To improve the usability of sLORETA, a parallel implementation of this algorithm has been realized and described in Chapter 3. Briefly, the most computationally expensive tasks have been optimized to run on a heterogeneous multi-CPU and multi-GPU computing system, whose characteristics are listed in Table 1.2.

To evaluate the real world performance of the parallel implemen-

tation, it was compared to a serial version of the same algorithm implemented in Matlab, through the evaluation of the relation between reconstruction time and sampling rate of the measured signals. Despite constraints on code optimization due to the Matlab integration of the parallel implementation for quick inclusion in multiplatform libraries, with a gray matter domain discretized with $9 \cdot 10^4$ cubic voxels, real time reconstruction was achieved with a sampling rate of up to 256 Hz for the case of 32 measuring electrodes and with a sampling rate of up to 128 samples per second in the case of 128 measuring electrodes. Real time EEG source localization may be exploited to inform electrical, visual or acoustic feedback stimulation for real time modulation of cerebral activity.

The sLORETA implementations were then experimentally validated with EEG measurements acquired on healthy subjects undergoing a visual evoked potentials experiment. The reconstructrions replicate literature findings obtained with fMRI techniques.

4.3 Future Work

Further work is needed to test the proposed EIT reconstruction approach for quick detection and classification of compact conductivity contrasts in presence of markedly irregular targets and also a mixture of large and small targets to better understand the limits of application. A straightforward next step would be the validation of the obtained results with experimental data acquired in vivo on both healthy subjects and stroke patients. Since other health conditions such as solid tumors can be characterized by a compact conductivity contrast on a predominantly uniform background, the applicability of the proposed technique to different illnesses may also be explored.

For what concerns epileptic foci localization with electrical brain imaging approaches, experimental data acquired on human patients is needed to validate the effectiveness of EIT as an information source for the considered application and to quantitatively measure the additional precision in localization which may be achieved by exploiting this technique. Moreover, EEG source localization may be performed by combining the electrical model of the head and intracranial measurements with source reconstruction algorithms such as sLORETA. This approach may allow a better understanding of the spread of epileptic seizures from one focus to the others and eventually it may lead to better planning of the surgical procedure.

Finally, considering the developed framework for real time EEG source localization, a thorough analysis to evaluate quantitatively the

improvement of reconstruction quality due to the optimization of the electrical model to the specific individual on which EEG measurements are made would better clarify the need for EIT and EEG source localization integration. Given the real time perfomance with realistic 3D head domains, the reconstructed electrical activity map may in the future be used as an input for BCI systems. Nowadays, the majority of BCI applications are based on machine learning algorithms which are used to analyze the raw EEG signal but, given the additional information coming from an electrical model, potentially optimized on the specific subject, source localization algorithms may provide a more complex input to BCI by providing also the source location of the recorded signal. This would translate in an higher number of possible input states for BCI which may expand the applicability of interfaces which connect humans and machines.

All the presented techniques have great potential not only in the clinical and research settings but, thanks to their peculiar characteristics of low cost, portability and high temporal resolution, it is not difficult to imagine their future inclusion in commercial BCI systems and eventually their extension to the consumer market.

Publications

The following paper has been co-authored and is currently reviewed with pending minor revision:

- **A. Samorè, M. Guermandi, S. Placati and R. Guerrieri** - Automatic detection and classification of compact conductivity contrasts with Electrical Impedance Tomography - *IEEE Transactions on Instrumentation and Measurement (TIM)*

The following poster has been co-authored and presented at ABEC 2016:

- **A. Samorè, D. Zhu, A. Nikpour and A. McEwan** - Electrical Imaging of Deep Brain Epileptic Activity with Stereotaxic Intracranial Electrodes - *IProceedings of the Australian Biomedical Engineering Conference (ABEC) 2016*

The following paper has been co-authored and is published:

- **S. Placati, M. Guermandi, A. Samorè, E. Franchi Scarselli and R. Guerrieri** - Parallel Solver for Diffuse Optical Tomography on Realistic Head Models with Scattering and Clear Regions - *IEEE Transactions on Biomedical Engineering (TBME)*

The following european project deliverable has been co-authored:

- **S. Placati, A. Samorè, M. Guermandi, M. Chiesi, R. Guerrieri, E. Pereda and J. G. Prieto** - Software libraries for brain imaging algorithms tuned for multiple data sets and report on the validation on ERP - *CREAM European Project Deliverable 4.2, 2015*

The following poster has been co-authored:

- **S. Placati, A. Samorè, M. Guermandi, E. Franchi Scarselli and R. Guerrieri** - Merging structural information from MRI/DTI to EEG/EIT and NIRS - *HIGH Profile European Project Workshop Poster, 2014*

Bibliography

[1] B. Blaus, "Wikipedia - neuron," distributed under a CC-BY-SA 3.0 license http://creativecommons.org/licenses/by-sa/3.0/.

[2] Chris and Diberri, "Wikiepdia - action potential," distributed under a CC-BY-SA 3.0 license http://creativecommons.org/licenses/by-sa/3.0/.

[3] Q. Jarosz, "Adapted from wikipedia - node of ranvier," distributed under a CC-BY-SA 3.0 license http://creativecommons.org/licenses/by-sa/3.0/.

[4] J. A. Beal, "Adapted from wikipedia - white matter," distributed under a CC-BY 2.5 license http://creativecommons.org/licenses/by/2.5.

[5] Daveynin, "Wikipedia - ct scanner," distributed under a CC-BY 2.0 license http://creativecommons.org/licenses/by/2.0.

[6] H. Gamboa, "Wikipedia - eeg waves," distributed under a CC-BY-SA 3.0 license http://creativecommons.org/licenses/by-sa/3.0/.

[7] A1, "Wikipedia - openmp," distributed under a CC-BY-SA 3.0 license http://creativecommons.org/licenses/by-sa/3.0/.

[8] B. staff. "Blausen gallery 2014". Wikiversity Journal of Medicine. DOI:10.15347/wjm/2014.010. ISSN 20018762. Own work, https://en.wikipedia.org/wiki/Electrocorticography.

[9] L. MILANI, "Automatic localization of multilead intracerebral electrodes implanted for StereoElectroEncephaloGraphy," 2013.

[10] M. G. Wentrup, K. Gramann, E. Wascher, and M. Buss, "EEG Source Localization for Brain-Computer-Interfaces," in *Neural Engineering, 2005. Conference Proceedings. 2nd International IEEE EMBS Conference on.* IEEE, Jul. 2001, pp. 128–131.

[11] C. M. Michel and M. M. Murray, "Towards the utilization of EEG as a brain imaging tool," *NeuroImage*, vol. 61, no. 2, pp. 371–385, Jun. 2012.

[12] S. Beniczky, G. Lantz, I. Rosenzweig, P. Åkeson, B. Pedersen, L. H. Pinborg, M. Ziebell, B. Jespersen, and A. Fuglsang-Frederiksen, "Source localization of rhythmic ictal EEG activity: A study of diagnostic accuracy following STARD criteria," *Epilepsia*, vol. 54, no. 10, pp. 1743–1752, Aug. 2013.

[13] D. Keeser, F. Padberg, E. Reisinger, O. Pogarell, V. Kirsch, U. Palm, S. Karch, H. J. Möller, M. A. Nitsche, and C. Mulert, "Prefrontal direct current stimulation modulates resting EEG and event-related potentials in healthy subjects: A standardized low resolution tomography (sLORETA) study," *NeuroImage*, vol. 55, no. 2, pp. 644–657, Mar. 2011.

[14] S. Vanneste and D. De Ridder, "Bifrontal transcranial direct current stimulation modulates tinnitus intensity and tinnitus-distress-related brain activity," *European Journal of Neuroscience*, vol. 34, no. 4, pp. 605–614, Jul. 2011.

[15] M. Lukaschewitsch, P. Maass, and M. Pidcock, "Tikhonov regularization for electrical impedance tomography on unbounded domains," *Inverse problems*, vol. 19, no. 3, p. 585, 2003.

[16] T. York, "Status of electrical tomography in industrial applications," *Journal of Electronic Imaging*, vol. 10, no. 3, p. 608, Jul. 2001.

[17] D. Silvera-Tawil, D. Rye, M. Soleimani, and M. Velonaki, "Electrical impedance tomography for artificial sensitive robotic skin: A review," 2014.

[18] R. Bayford, "Bioimpedance tomography (electrical impedance tomography)," *Annu. Rev. Biomed. Eng.*, vol. 8, no. 1, pp. 63–91, Aug 2006.

[19] J. Mueller, D. Isaacson, and J. Newell, "Reconstruction of conductivity changes due to ventilation and perfusion from eit data collected on a rectangular electrode array," *Physiological Measurement*, vol. 22, no. 1, p. 97, 2001.

[20] N. Vaisman, N. Weintrob, and A. Blumental, "Gastric emptying in patients with type i diabetes mellitus," *Annals of the New ...*, 1999.

[21] R. Halter, A. Hartov, and K. Paulsen, "A broadband high-frequency electrical impedance tomography system for breast imaging," *Biomedical Engineering, IEEE Transactions on*, vol. 55, no. 2, pp. 650–659, 2008.

[22] H. Syed, A. Borsic, A. Hartov, and R. Halter, "Anatomically accurate hard priors for transrectal electrical impedance tomography (treit) of the prostate," *Physiological Measurement*, vol. 33, no. 5, p. 719, 2012.

[23] T. Tidswell, A. Gibson, R. H. Bayford, and D. S. Holder, "Three-dimensional electrical impedance tomography of human brain activity," *NeuroImage*, vol. 13, no. 2, pp. 283–294, Feb. 2001.

[24] H. J. Kim, W. C. Jeong, S. Z. K. Sajib, M.-O. Kim, O. I. Kwon, E. Je Woo, and D.-H. Kim, "Simultaneous imaging of dual-frequency electrical conductivity using a combination of MREIT and MREPT," *Magnetic Resonance in Medicine*, vol. 71, no. 1, pp. 200–208, Feb. 2013.

[25] M. Kranjc, F. Bajd, I. Serša, and D. Miklavcic, "Magnetic resonance electrical impedance tomography for determining electric field distribution during electroporation," *Journal of Physics: Conference Series*, vol. 434, p. 012086, Apr. 2013.

[26] D. H. Kim, M. O. Ghim, O. Kwon, H. Kim, and J. Seo, "MREIT and EPT: a comparison of two conductivity imaging modalities," in *Proceedings of the 19th ...*, 2011.

[27] S. K. Lee, S. Bulumulla, and P. Lamb, "Measurement of electrical properties of biological tissue at radio frequencies using magnetic resonance imaging," *... and Propagation (EuCAP ...*, 2015.

[28] X. Zhang, J. Liu, and B. He, "Magnetic-Resonance-Based Electrical Properties Tomography: A Review," *IEEE Reviews in Biomedical Engineering*, vol. 7, pp. 87–96.

[29] K. Karimi, N. G. Dickson, and F. Hamze, "A Performance Comparison of CUDA and OpenCL," *arXiv.org*, May 2010.

[30] D. Kirk and W. Wen-mei, *Programming massively parallel processors: a hands-on approach*, 2010.

[31] G. Silva, W. Koroshetz, R. González, and L. Schwamm, *Causes of Ischemic Stroke*, 2010.

[32] L. M. Brass, "Stroke," *Yale University School of Medicine Heart Book*, pp. 215–234, Feb 1992.

[33] M. Nichols, N. Townsend, P. Scarborough, M. Rayner, U. of Oxford Jose Leal, R. Luengo-Fernandez, and A. Gray, "European cardiovascular disease statistics 2012 edition," European Heart Network and European Society of Cardiology, Tech. Rep., Sep 2012.

[34] A. Go, D. Mozaffarian, V. Roger, E. Benjamin, J. Berry, W. Borden, D. Bravata, D. SHIFAN, E. Ford, and C. Fox, "Executive summary: Heart disease and stroke statistics: 2013 update: A report from the american heart association," *Circulation*, vol. 127, no. 1, 2013.

[35] T. Duong and M. Fisher, "Applications of diffusion/perfusion magnetic resonance imaging in experimental and clinical aspects of stroke," *Current atherosclerosis reports*, vol. 6, no. 4, pp. 267–273, 2004.

[36] S. M. Davis and G. A. Donnan, "4.5 hours: The new time window for tissue plasminogen activator in stroke," *Stroke*, vol. 40, no. 6, pp. 2266–2267, Jun 2009.

[37] I. Marinkovic, O. Mattila, D. Strbian, A. Meretoja, S. Shekhar, J. Saksi, U. Abo-Ramadan, V. Rantanen, P. Lindsberg, and T. Tatlisumak, "Evolution of intracerebral hemorrhage after intravenous tpa: reversal of harmful effects with mast cell stabilization," *Journal of Cerebral Blood Flow & Metabolism*, vol. 34, no. 1, pp. 176–181, 2014.

[38] D. Holder, "Appendix b introduction to biomedical electrical impedance tomography," *Electrical Impedance Tomography: Methods, History and Applications*, p. 423, 2010.

[39] M. T. Clay and T. C. Ferree, "Weighted regularization in electrical impedance tomography with applications to acute cerebral stroke," *IEEE Trans. Med. Imag.*, vol. 21, no. 6, pp. 629–637, Jan 2002.

[40] R. Oostenveld and P. Praamstra, "The five percent electrode system for high-resolution eeg and erp measurements," *Clinical neurophysiology*, vol. 112, no. 4, pp. 713–719, 2001.

[41] NICE, "Epilepsies: diagnosis and management," pp. 1–111, Dec. 2016.

[42] B. C. Jobst and G. D. Cascino, "Resective Epilepsy Surgery for Drug-Resistant Focal Epilepsy," *JAMA*, vol. 313, no. 3, p. 285, Jan. 2015.

[43] L. Landa, Z. Krpoun, and M. Kolarova, "Event-related potentials and their applications," *Activitas Nervosa ...*, 2014.

[44] S. Sur and V. K. Sinha, "Event-related potential: An overview," *Journal of Industrial Psychiatry*, 2009.

[45] D. H. Mathalon, J. M. Ford, and A. Pfefferbaum, "Trait and state aspects of P300 amplitude reduction in schizophrenia: A retrospective longitudinal study," *BPS*, vol. 47, no. 5, pp. 434–449, 2000.

[46] M. Hansenne, W. Pitchot, A. G. Moreno, I. U. Zaldua, and M. Ansseau, "Suicidal behavior in depressive disorder: An event-related potential study," *BPS*, vol. 40, no. 2, pp. 116–122, 1996.

[47] T. Turan, E. Esel, F. Karaaslan, M. Basturk, A. Oguz, and I. Yabanoglu, "Auditory event-related potentials in panic and generalised anxiety disorders," *Progress in Neuro-Psychopharmacology & Biological Psychiatry*, vol. 26, no. 1, pp. 123–126, Jan. 2002.

[48] N. Paul, S. H. Nizamie, and A. Basu, *P300 in obsessive compulsive disorder*. Eastern Journal of ..., 2016.

[49] B. Packham, H. Koo, and A. Romsauerova, "Comparison of frequency difference reconstruction algorithms for the detection of acute stroke using EIT in a realistic head-shaped tank," *Physiological Measurement*, 2012.

[50] X. Zhang, W. Wang, G. Sze, D. Barber, and C. Chatwin, "An image reconstruction algorithm for 3d electrical impedance mammography," *IEEE Trans. Med. Imag.*, vol. 33, no. 12, pp. 2223–2241, 2014.

[51] BrainSuite, http://neuroimage.usc.edu/neuro/BrainSuite.

[52] I. Foundation, https://www.itis.ethz.ch/virtual-population/tissue-properties/database/.

[53] S. Gabriel, R. Lau, and C. Gabriel, "The dielectric properties of biological tissues: lll. parametric models for the dielectric spectrum of tissues," *Physics in medicine and biology*, vol. 41, no. 11, p. 2271, 1996.

[54] ——, "The dielectric properties of biological tissues: Ii. measurements in the frequency range 10 hz to 20 ghz," *Physics in Medicine and Biology*, vol. 41, no. 11, p. 2251, 1996.

[55] M. Cheney, D. Isaacson, and J. Newell, "Electrical impedance tomography," *SIAM review*, vol. 41, no. 1, pp. 85–101, 1999.

[56] M. Cook and Z. Koles, "A high-resolution anisotropic finite-volume head model for eeg source analysis," *Proceedings of the 28th IEEE EMBS Annual International Conference*, pp. 4536–4539, 2006.

[57] W. R. B. Lionheart, "Eit reconstruction algorithms: pitfalls, challenges and recent developments," *Physiological Measurement*, vol. 25, no. 1, pp. 125–42, Feb 2004.

[58] T. J. YORKEY, J. G. WEBSTER, and W. J. TOMPKINS, "Comparing Reconstruction Algorithms for Electrical-Impedance Tomography," *IEEE Transactions on Biomedical Engineering*, vol. 34, no. 11, pp. 843–852, Nov. 1987.

[59] M. Vauhkonen, D. Vadasz, P. Karjalainen, E. Somersalo, and J. Kaipio, "Tikhonov regularization and prior information in electrical impedance tomography," *IEEE Trans. Med. Imag.*, vol. 17, no. 2, pp. 285–293, 1998.

[60] A. Borsic, B. M. Graham, A. Adler, and W. Lionheart, "Total variation regularization in electrical impedance tomography," 2007.

[61] M. Gehre, T. Kluth, A. Lipponen, B. Jin, A. Seppanen, J. P. Kaipio, and P. Maass, "Journal of Computational and Applied Mathematics," *Journal of Computational and Applied Mathematics*, vol. 236, no. 8, pp. 2126–2136, Feb. 2012.

[62] J. Zhao, Y. Xu, C. Tan, and F. Dong, "A fast sparse reconstruction algorithm for electrical tomography," *Measurement Science and Technology*, 2014.

[63] S. I. Kang, A. K. Khambampati, M. H. Jeon, B. S. Kim, and K. Y. Kim, "A sub-domain based regularization method with prior information for human thorax imaging using electrical impedance tomography," *Measurement Science and Technology*, pp. 1–9, Nov. 2016.

[64] L. Miao, Y. Ma, and J. Wang, "ROI-Based Image Reconstruction of Electrical Impedance Tomography Used to Detect Regional

Conductivity Variation," *IEEE Transactions on Instrumentation and Measurement*, vol. 63, no. 12, pp. 2903–2910, 2014.

[65] S. I. Kang, A. K. Khambampati, B. S. Kim, and K. Y. Kim, "EIT image reconstruction for two-phase flow monitoring using a sub-domain based regularization method," *Flow Measurement and Instrumentation*, 2016.

[66] F. Santosa and M. Vogelius, "A backprojection algorithm for electrical impedance imaging," *SIAM Journal on Applied Mathematics*, 1990.

[67] H. Wang, C. Wang, and W. Yin, "A Pre-Iteration Method for the Inverse Problem in Electrical Impedance Tomography," *IEEE Transactions on Instrumentation and Measurement*, vol. 53, no. 4, pp. 1093–1096, Aug. 2004.

[68] A. Nissinen, L. M. Heikkinen, and J. P. Kaipio, "The Bayesian approximation error approach for electrical impedance tomography—experimental results," *Measurement Science and Technology*, vol. 19, no. 1, p. 015501, Nov. 2007.

[69] A. Nissinen, V. P. Kolehmainen, and J. P. Kaipio, "Compensation of Modelling Errors Due to Unknown Domain Boundary in Electrical Impedance Tomography," *IEEE transactions on medical imaging*, vol. 30, no. 2, pp. 231–242.

[70] B. Gong, B. Schullcke, S. Krueger-Ziolek, U. Mueller-Lisse, and K. Moeller, "Sparse regularization for EIT reconstruction incorporating structural information derived from medical imaging," *Physiological Measurement*, pp. 843–862, Nov. 2016.

[71] P. C. Hansen and D. P. OLEARY, "The use of the l-curve in the regularization of discrete ill-posed problems," *SIAM Journal on Scientific Computing*, vol. 14, no. 6, pp. 1487–1503, Nov. 1993.

[72] G. Golub, P. Hansen, and D. O'Leary, "Tikhonov regularization and total least squares," *SIAM Journal on Matrix Analysis and Applications*, vol. 21, no. 1, pp. 185–194, 1999.

[73] B. Brandstatter, "Jacobian calculation for electrical impedance tomography based on the reciprocity principle," *Magnetics, IEEE Transactions on*, vol. 39, no. 3, pp. 1309–1312, 2003.

[74] M. Glidewell and K. Ng, "Anatomically constrained electrical impedance tomography for three-dimensional anisotropic bodies,"

Medical Imaging, IEEE Transactions on, vol. 16, no. 5, pp. 572–580, 1997.

[75] M. Clay and T. Ferree, "Weighted regularization in electrical impedance tomography with applications to acute cerebral stroke," *Medical Imaging*, 2002.

[76] A. Technologies, "Agilent 4294A Precision Impedance Analyzer Service Manual," pp. 1–249, Jan. 2007.

[77] L. F. e. Al, "A comparison of two EIT systems suitable for imaging impedance changes in epilepsy," pp. 1–19, Jun. 2009.

[78] P. R. Johnston and R. M. Gulrajani, "Selecting the corner in the l-curve approach to tikhonov regularization," *IEEE Transactions on Biomedical Engineering*, vol. 47, no. 9, pp. 1293–1296, 2000.

[79] P. Pantano, F. Caramia, L. Bozzao, and C. Dieler, "Delayed increase in infarct volume after cerebral ischemia correlations with thrombolytic treatment and clinical outcome," *Stroke*, 1999.

[80] A. Nissinen, J. P. Kaipio, M. Vauhkonen, and V. Kolehmainen, "Contrast enhancement in EIT imaging of the brain," *Physiological Measurement*, pp. 1–24, Dec. 2015.

[81] E. Lee, M.-E. Ts, J. K. Seo, and E. J. Woo, "Breast EIT using a new projected image reconstruction method with multi-frequency measurements," *Physiological Measurement*, vol. 33, no. 5, pp. 751–765, Apr. 2012.

[82] A. D. Friederici and K. Alter, "Lateralization of auditory language functions: A dynamic dual pathway model," *Brain and Language*, vol. 89, no. 2, pp. 267–276, May 2004.

[83] A. B. Vinton, R. Carne, R. J. Hicks, P. M. Desmond, C. Kilpatrick, A. H. Kaye, and T. J. O'Brien, "The extent of resection of FDG-PET hypometabolism relates to outcome of temporal lobectomy," *Brain*, vol. 130, no. 2, pp. 548–560, Feb. 2007.

[84] P. Megevand, L. Spinelli, M. Genetti, V. Brodbeck, S. Momjian, K. Schaller, C. M. Michel, S. Vulliemoz, and M. Seeck, "Electric source imaging of interictal activity accurately localises the seizure onset zone," *Journal of Neurology, Neurosurgery & Psychiatry*, vol. 85, no. 1, pp. 38–43, Dec. 2013.

[85] A. M. Lascano, T. Perneger, S. Vulliemoz, L. Spinelli, V. Garibotto, C. M. Korff, M. I. Vargas, C. M. Michel, and M. Seeck,

"Clinical Neurophysiology," *Clinical Neurophysiology*, vol. 127, no. 1, pp. 150–155, Jan. 2016.

[86] O. David, T. Blauwblomme, A. S. Job, S. Chabardes, D. Hoffmann, L. Minotti, and P. Kahane, "Imaging the seizure onset zone with stereo-electroencephalography," *Brain*, vol. 134, no. 10, pp. 2898–2911, Oct. 2011.

[87] M. Elbohouty, "Electrical conductivity of brain cortex slices in seizing and non-seizing states," 2013.

[88] M. M. Mesulam, "From sensation to cognition." *Brain*, 1998.

[89] J. Bullier, "Visual perception is too fast to be impenetrable to cognition," *Behavioural and Brain Sciences*, pp. 1–83, Jul. 1999.

[90] *Source localization of brain electrical activity.* Elsevier, Amsterdam, 1987.

[91] S. Axler, P. Bourdon, and R. Wade, "Harmonic function theory," 2000.

[92] R. D. Pascual-Marqui, "Review of methods for solving the EEG inverse problem," *International journal of ...*, 1999.

[93] ——, "ISBET NEWSLETTER," pp. 1–23, Dec. 2002.

[94] R. D. Pascal-Marquis, M. Esslen, K. Kochi, and D. Lehmann, *Functionnal imaging with low resolution brain electromagnetic tomography (LORETA): review, new comparaisons, and new validation.* Japanese Journal of Clinical ..., 2002.

[95] T. D. Marco, F. Ries, M. Guermandi, and R. Guerrieri, "Eit forward problem parallel simulation environment with anisotropic tissue and realistic electrode models," *IEEE Trans. Med. Imag.*, vol. 59, no. 5, pp. 1229–1239, 2012.

[96] F. Di Russo, A. Stella, G. Spitoni, F. Strappini, S. Sdoia, G. Galati, S. A. Hillyard, D. Spinelli, and S. Pitzalis, "Spatiotemporal brain mapping of spatial attention effects on pattern-reversal ERPs," *Human Brain Mapping*, vol. 33, no. 6, pp. 1334–1351, Apr. 2011.